UNIVERSIDADE DE LISBOA
FACULDADE DE CIÊNCIAS
DEPARTAMENTO DE FÍSICA

Testing cosmological structure formation in Unified Dark Matter-Energy models

Diogo Manuel Lopes Castelão

Mestrado em Física
especialização em Astrofísica e Cosmologia

Dissertação orientada por:
Ismael Tereno
Alberto Rozas-Fernández

2017

Agradecimentos

Neste breve pedaço de texto respiro a liberdade de não escrever exaustivamente sob as normas e formalidades exigidas adiante. E aproveito-o para agradecer ao doutor Ismael Tereno por ter sido o melhor orientador de sempre (e o pior, porque foi o único) e uma pessoa magnífica. Ao doutor Alberto Rozas-Fernández por toda a ajuda, disponibilidade e conversas estimulantes. Agradeço à Katrine, por toda a paciência e motivação, por ser bela e estar sempre ao meu lado. Agradeço ao João Pereira e ao Bartolomeu, por serem o meu refúgio emocional. Agradeço a toda a minha família, mas agradeço mais ao meus pais, à minha irmã e ao Ricardo, que me deu abrigo e amizade. Também agradeço ao Manuel, à Joana, ao Batalha, ao João Gandâra, à Joana Filipa, à Sara e a outros amigos por mencionar, porque fazem parte de mim e me inspiram, por vezes expiram, como bons amigos. Dou, por fim, um grande beijinho ao meu avó, que vive todos os dias no meu pensamento.

Abstract

There is a large number of cosmological models that are able to explain the recent acceleration of expansion of the universe. Besides describing the dynamics of the universe, cosmological models also need to correctly predict the observed structure in the universe. The ΛCDM model is in a very good agreement with most cosmological observations.
This thesis deals with an alternative approach, Unified Dark Matter-Energy models (UDM), a class of models that entertains the possibility of a universe where dark matter and dark energy exist as a single essence. We focus on a model with a fast transition between dark matter-like and dark energy-like behaviours. The rapidity of the transition is an important feature to enable the formation of structure. We also discuss another model, the Generalised Chaplygin Gas (GCG), with a small note on the important effect of non-linear clustering on small scales in this type of models. We implemented these two models in the Boltzmann Code CLASS which allowed us to obtain the relevant structure formation quantities. From these, we studied the viability of the UDM model using several cosmological observations in an MCMC analysis. The chosen observations were SNe Ia, BAO, CMB and weak lensing data. At the end of our analysis, we were able to conclude for the first time that this model is able to form structure and is in agreement with structure formation data.

Key words: *Unified dark matter-energy models, large scale structure, cosmological parameters, Bayesian inference*

Resumo em português

A dinâmica do universo em grandes escalas é dominada pela interação gravítica, que actualmente é explicada pela teoria da Relatividade Geral (GR). Para lá da interacção gravítica, os componentes que preenchem o universo e suas interações devem ser explicadas pelo modelo padrão da Física de partículas. Desta simbiose esperamos poder descrever a evolução do nosso Universo desde o seu princípio, começando na altura em que o universo era um plasma muito quente e denso, com uma taxa de interação entre partículas elevada. Com a expansão do Universo, a taxa de interação vai diminuindo e o plasma primordial vai arrefecendo, permitindo a formação dos primeiros elementos leves como o hidrogénio, hélio e lítio. Quando a densidade de energia diminuiu o suficiente para que os primeiros átomos se tornassem estáveis, os fotões começaram a propagar-se livremente: este evento é hoje detectado na forma de radiação de microondas (CMB). Esta radiação é quase uniforme, com uma temperatura média que ronda os 2.7 K em todas as direções. No entanto, ele contém pequenas flutuações de temperatura e essas pequenas variações representam pequenas não-homogeneidades na densidade primordial da matéria. Essas flutuações da matéria permitiram a criação de regiões com uma densidade superior à densidade média e que com o passar do tempo foram crescendo, criando por um lado regiões cada vez mais densas que eventualmente levaram à criação de galáxias, estrelas e planetas, e por outro lado regiões de menor densidade que se foram tornando cada vez menos densas, formando grandes zonas de "vazio". No entanto, à luz do modelo padrão de Física de partículas e da GR não somos capazes de recriar esta história do nosso Universo.

Para tornar isso possível, em primeiro lugar, logo após o Big-bang, precisamos introduzir aquilo a que chamamos de inflação cósmica, um período em que o universo teve uma grande expansão acelerada. Mais tarde, é necessário introduzir dois componentes desconhecidos no Universo. Componentes esses que acabam por ser os elementos mais abundantes do Universo. O primeiro componente desconhecido é denominado matéria escura, e é necessário para a formação de estrutura. O segundo componente, a energia escura, é necessário para explicar a actual expansão acelerada do Universo.

A natureza destes dois componentes é actualmente desconhecida e a sua detecção directa ou indirecta é um dos grandes objectivos actuais da cosmologia observacional.

Por parte da cosmologia teórica, a lista de modelos que tenta explicar a actual expansão acelerada do universo, bem como a formação de estrutura, é extensa. O modelo mais aceite chama-se ΛCDM, em que a energia escura é a constante cosmológica Λ e a matéria escura é uma componente fria (CDM).

Nesta dissertação, exploramos uma alternativa ao modelo ΛCDM, onde se considera que estes dois componentes são na verdade apenas um, havendo uma unificação da matéria escura e da energia escura. Esta abordagem é conhecida como modelos de Unified Dark Matter-Energy (UDM). Em particular, iremo-nos concentrar em descrever e testar com dados observacionais um modelo UDM específico que tem uma transição rápida entre um regime em que se comporta como matéria escura e um regime de energia escura.

Este modelo foi proposto na literatura pelo co-orientador desta dissertação e colaboradores e não tinha ainda sido testado com dados observacionais de formação de estrutura. Para fazer uma análise das propriedades do nosso modelo UDM começamos no primeiro capítulo com uma revisão da cosmologia padrão, onde fazemos referência ao modelo ΛCDM e dedicamos algum tempo à teoria das perturbações lineares. No segundo capítulo começamos por fazer um levantamento das várias ideias propostas quanto à origem da energia escura, alternativas ao modelo padrão, e apresentamos uma revisão histórica dos modelos UDM. De seguida, estudamos em detalhe a dinâmica do nosso modelo UDM, onde é feita uma análise relativa às perturbações e à formação de estrutura para este modelo. É também abordado

o tema das condições iniciais para este caso particular, necessárias para resolver numericamente as equações de evolução das perturbações. Neste capítulo é também apresentado um outro modelo UDM, o Generalised Chaplygin Gas (GCG), que foi usado como modelo de controlo na implementação do modelo UDM num código de evolução das perturbações lineares. No fim deste capítulo abordamos ainda o efeito de backreaction, isto é, o impacto que as regiões já colapsadas têm na evolução das perturbações. Este efeito foi apresentado recentemente na literatura aplicado ao modelo GCG mas é também aplicável ao nosso modelo UDM.

O programa usado para o cálculo da evolução das perturbações chama-se Cosmic Linear Anisotropy Solving System (CLASS) e é apresentado no terceiro capítulo. Neste capítulo, após uma pequena introdução sobre o funcionamento do código, é feita uma apresentação detalhada da implementação de ambos os modelos UDM neste programa. A nossa apresentação segue a estrutura do CLASS e é dividida em vários módulos (background, perturbations, etc) onde mostramos e analisamos vários resultados obtidos com a implementação, tais como: a evolução da densidade de energia, a evolução da equação de estado e da velocidade do som, a evolução da densidade de contraste e o power spectrum da matéria.

No capítulo seguinte, procedemos ao teste do nosso modelo UDM face aos dados observáveis. Começamos por apresentar os resultados já publicados do teste a este modelo face a vários observáveis de background, onde o modelo se mostrou tão viável quanto o modelo ΛCDM.

Tendo em conta que o principal objectivo desta dissertação é o teste deste modelo na sua capacidade de formar estrutura, fazemos uma pequena revisão teórica do efeito de lentes gravitacionais fracas (weak lensing), uma importante sonda de formação de estrutura cosmológica.

De seguida são apresentados os dados usados no teste do nosso modelo: JLA (usando Supernovas Ia) e BOSS (usando as oscilações acústicas bariónicas) como testes de background, Planck (usando o CMB) e KiDS (usando weak lensing) como testes à formação de estrutura.

Os testes ao modelo, foram feitos com inferência Bayesiana, usando um código Monte Carlo de cadeias de Markov, chamado MontePython. Na nossa análise, dividimos o espaço dos parâmetros em três regimes e para cada um deles corremos várias cadeias de Markov para diferentes combinações de dados e parâmetros livres. Em particular, fizemos análises com e sem os dados do KiDS, para permitir isolar a contribuição das lentes gravitacionais e compreender melhor o seu impacto na análise. Fizemos também análises com um maior e menor número de parâmetros livres, de modo a diminuir as degenerescências entre parâmetros.

Um aspecto importante a considerar é que com o CLASS calculámos o power spectrum linear da matéria, enquanto que a maior parte dos dados medidos pelo KiDS estão no regime não linear de formação de estrutura. Depois de apresentada a metodologia adoptada para a análise incluímos o procedimento usado para lidar com a não linearidade e apresentamos finalmente os resultados.

Concluímos que o modelo é viável num dos três regimes estudados e rejeitado noutro dos regimes. No regime intermédio os resultados são estatisticamente inconclusivos mas promissores, pois apresenta algumas das combinações de parâmetros com melhor likelihood no conjunto dos três regimes.

Em resumo, esta dissertação mostra pela primeira vez a viabilidade deste modelo na formação de estrutura, concluindo que é um possível candidato para descrever a matéria e energia escura, e restringindo os valores dos parâmetros viáveis em relação aos encontrados em análise anterior onde o modelo foi testado a nível de background.

Identificamos também melhoramentos possíveis de efectuar em análises futuras, ao nível do tratamento das integrações numéricas, do tratamento do regime não-linear e do método numérico de amostragem

da distribuição de probabilidades no espaço dos parâmetros. E ainda alternativas relacionadas ao modelo teórico proposto.

Palavras-chave: *Modelos de unificação de matéria e energia escuras, estrutura de grande escala do Universo, parâmetros cosmológicos, inferência Bayesiana*

Contents

List of Figures

List of Tables

Introduction

The dynamics of the universe on large scales is dominated by the gravitational interaction, which is, in the standard view, explained by the theory of General Relativity (GR). On the other hand, the contents of the universe and their interactions besides gravity are expected to be explained by the standard model of particle physics. From this symbiosis we expect to be able to describe our universe from the very beginning, when the universe was a very hot and dense plasma, matter was in the form of free electrons and atomic nuclei and the interactions between particles were very energetic and frequent, to the very end. In the thermal evolution of the universe, the primordial plasma cooled down and light elements like hydrogen, helium and lithium were formed. When the energy dropped enough for the first stable atoms to exist, the universe transparent and the photons have been propagating freely since, and we now observe them in the form of microwave radiation (CMB). This radiation is almost uniform, with the same temperature of about 2.7 K in all directions. However, this CMB contains small fluctuations in temperature and those tiny variations represent small inhomogeneities in the primordial density of matter. As time passed by, this matter fluctuation grew and overdense regions became increasingly denser leading to the creation of galaxies, stars and planets. This brief history is well known, and nowadays it seems to be so right that even when we were small children that history made perfect sense. What causes a child, that has no deep knowledge of physics, to feel this idea to be true goes beyond this dissertation, but the most important thing is that we are, unfortunately, not able to recreate the universe dynamics if we rely only on the standard model of particle physics and on standard GR.

First of all, we need to introduce inflation at the the very beginning. Later on, some exotic components must also be introduced that turn out to dominate the matter-energy content of the universe. These are dark matter (DM), needed to form structure, and dark energy (DE), required to explain the late-time accelerated expansion of the universe. The true nature of these two components is unknown and the search for it is an ongoing quest of cosmological studies. The first step in this quest is to assess if a certain model of DM and DE matches our current observations. There are many models proposed that pass this first test. However, these several ideas have different characteristics, even if they try to replicate the same universe. This pushes the searches for the nature of these components to increasing levels of precision, where we try to find small signatures that distinguish a model from another.

In this dissertation we explore the elegant idea of considering that the two components are in fact just one. This approach is known as the Unified Dark Matter-Energy models (UDM). More specifically, we focus on describing and testing a specific UDM model that has a fast transition from a DM like behavior to a DE like one. In order to fully describe the properties of our UDM model of interest we start, in chapter 1, with a review of standard cosmology, with an emphasis on linear perturbation theory, and proceed in chapter 2 with the detailed description of the model. We also introduce in chapter 2 another type of unified model, the well-known Generalised Chaplygin Gas (GCG) (including back-reaction effects), that we will use as a benchmark in implementation tests. In order to test the

model, we start by implementing it in the Cosmic Linear Anisotropy Solving System (CLASS). CLASS is a software program designed to compute the evolution of linear perturbations in the universe. The details of the modifications of CLASS for both models are presented in chapter 3, where we also further discuss the properties of the models now supported by outputs of CLASS, such as the matter power spectrum. We then move to the actual model testing in chapter 4. Here we perform several Bayesian inference analyses using the Markov Chain Monte Carlo (MCMC) code MontePython. The UDM model with fast transition is tested against various sets of cosmological structure formation and background expansion data (JLA Supernova data, BOSS BAO data, Planck CMB data and KiDS weak lensing data) using various sets of varying and fixed cosmological and nuisance parameters. We conclude in chapter 5, showing for the first time the viability of this model at structure formation level, implying that the UDM approach is still a possible candidate to describe DM and DE.

Chapter 1

Cosmology

1.1 The Homogeneous universe

Standard Big Bang cosmology rests on two fundamental assumptions:

-When we average over a sufficiently large scale, the observable properties of the universe are isotropic. In particular, the microwave background is almost perfectly isotropic and the distribution of distant galaxies approaches isotropy, while on the contrary nearby galaxies are very anisotropically distributed.

-Our position in the universe is by no means preferred to any other. This implies that the first assumption must hold for every observer in the universe. But if the universe is isotropic around all its points, it is also necessarily homogeneous.

These two assumptions requiring that the universe is homogeneous and isotropic when averaging over larges volumes are expressed, in general relativity, on the Friedmann-Lemaitre-Robertson-Walker (FLRW) metric:

$$ds^2 = g_{\mu\nu}dx^\mu dx^\nu = -dt^2 + a^2\left[\frac{dr^2}{1-kr^2} + r^2(d\theta^2 + sin(\theta)^2 d\varphi^2)\right], \tag{1.1}$$

usually written as

$$ds^2 = dt^2 - a^2(t)\gamma_{ij}dx^i dx^j, \tag{1.2}$$

where $a(t)$ is known as the scale factor, t is the cosmic time and k is the space curvature. For $k > 0$ the universe is closed. For $k = 0$ the universe is flat. For $k < 0$ the universe is open, having a hyperbolic spatial section.

In addition to the cosmic time t, it is also convenient to introduce the conformal time defined by

$$\tau \equiv \int a^{-1}dt. \tag{1.3}$$

The Einstein equations, describing the dynamics of the universe, can be computed as follows [1, 2]. From the metric $g_{\mu\nu}$, we first obtain the Christoffel symbols

$$\Gamma^{\mu}_{\nu\delta} = \frac{1}{2} g^{\mu\alpha}(g_{\alpha\nu,\delta} + g_{\alpha\delta,\nu} - g_{\nu\delta,\alpha}), \tag{1.4}$$

with $g_{\alpha\nu,\delta} = \dfrac{\partial g_{\alpha\nu}}{\partial x^{\delta}}$. The Ricci curvature tensor is then defined by

$$R_{\mu\nu} = \Gamma^{\alpha}_{\mu\nu,\alpha} - \Gamma^{\alpha}_{\mu\alpha,\nu} + \Gamma^{\alpha}_{\mu\nu}\Gamma^{\beta}_{\alpha\beta} - \Gamma^{\alpha}_{\mu\beta}\Gamma^{\beta}_{\alpha\nu}, \tag{1.5}$$

and can contracted in order to get the Ricci scalar

$$R = g^{\mu\nu} R_{\mu\nu}. \tag{1.6}$$

The desired Einstein field equations can be obtained from the following action

$$S = \int d^4x \sqrt{-g} \left[\frac{R}{16\pi G} + L_M \right], \tag{1.7}$$

where the first term in the action comes from the Einstein-Hilbert action and the L_M represents all the matter fields present.

From the principle of least action we have

$$\begin{aligned} 0 = \delta S &= \int d^4x \left[\frac{1}{16\pi G} \frac{\delta(\sqrt{-g}R)}{\delta g^{\mu\nu}} + \frac{\delta(\sqrt{-g}L_M)}{\delta g^{\mu\nu}} \right] \delta g^{\mu\nu} \\ &= \int d^4x \sqrt{-g} \left[\frac{1}{16\pi G} \left(\frac{\delta R}{g^{\mu\nu}} + \frac{R}{\sqrt{-g}} \frac{\delta\sqrt{-g}}{\delta g^{\mu\nu}} \right) + \frac{1}{\sqrt{-g}} \frac{\delta(\sqrt{-g}L_M)}{\delta g^{\mu\nu}} \right] \delta g^{\mu\nu}. \end{aligned} \tag{1.8}$$

Since this should hold for any variation with respect to $g^{\mu\nu}$, it follows that

$$\frac{\delta R}{g^{\mu\nu}} + \frac{R}{\sqrt{-g}} \frac{\delta\sqrt{-g}}{\delta g^{\mu\nu}} = 8\pi G \frac{(-2)}{\sqrt{-g}} \frac{\delta(\sqrt{-g}L_M)}{\delta g^{\mu\nu}}. \tag{1.9}$$

The right-hand side of the equation is the energy-momentum tensor

$$T_{\mu\nu} = -\frac{2}{\sqrt{-g}} \frac{\delta(\sqrt{-g}L_M)}{\delta g^{\mu\nu}}, \tag{1.10}$$

that contains the density and pressure of all the cosmological fluids (the source of gravity). By defining the properties of each fluid we determine the cosmic expansion.

It was proved in [4] that the variation of the Ricci scalar R and the variation of the determinant g is

$$\frac{\delta R}{\delta g^{\mu\nu}} = R_{\mu\nu} \tag{1.11}$$

$$\delta g = \delta det(g_{\mu\nu}) = g g^{\mu\nu} \delta g_{\mu\nu} \Rightarrow \frac{1}{\sqrt{-g}} \frac{\delta\sqrt{-g}}{\delta g^{\mu\nu}} = -\frac{1}{2} g_{\mu\nu}, \tag{1.12}$$

which allow us to rewrite the right-hand side of Eq.(1.9) and obtain the Einstein equations

$$R_{\mu\nu} - \frac{1}{2} g_{\mu\nu} R = G_{\mu\nu} = 8\pi G T_{\mu\nu}, \tag{1.13}$$

where $G_{\mu\nu}$ is the Einstein tensor.

The dynamical evolution of the universe is known once we solve the Einstein equations of General Relativity [1, 2, 5].

For the FLRW metric Eq.(1.2), the non-vanishing Christoffel symbols are

$$\Gamma^0_{ij} = a\dot{a}\gamma_{ij}, \tag{1.14}$$

$$\Gamma^i_{0j} = \frac{\dot{a}}{a}\delta^i_j, \tag{1.15}$$

$$\Gamma^i_{jk} = \frac{1}{2}\gamma^{ij}\left(\partial_j\gamma_{kl} + \partial_k\gamma_{jl} - \partial_l\gamma_{jk}\right). \tag{1.16}$$

From that we get the following non-vanishing components of the Ricci tensor and the Ricci scalar

$$R_{00} = -3\frac{\ddot{a}}{a}, \tag{1.17}$$

$$R_{ij} = -\left[\frac{\ddot{a}}{a} + 2\left(\frac{\dot{a}}{a}\right)^2 + 2\frac{k}{a^2}\right]g_{ij}, \tag{1.18}$$

$$R = -6\left[\frac{\ddot{a}}{a} + \left(\frac{\dot{a}}{a}\right)^2 + \frac{k}{a^2}\right], \tag{1.19}$$

and we obtain the non-vanishing components of the Einstein tensor

$$G^0_0 = 3\left[\left(\frac{\dot{a}}{a}\right)^2 + \frac{k}{a^2}\right], \tag{1.20}$$

$$G^i_j = \left[2\frac{\ddot{a}}{a} + \left(\frac{\dot{a}}{a}\right)^2 + \frac{k}{a^2}\right]\delta^i_j, \tag{1.21}$$

with $G^\mu_\nu = g^{\mu\delta}G_{\delta\nu}$. Here a dot represents the derivative with respect to the cosmic time t.

The Einstein equations can be reduced to two differential equations by combining Eqs. (1.20) and (1.21) with the energy-momentum tensor Eq.(1.10)

$$\left(\frac{\dot{a}}{a}\right)^2 = \frac{8\pi G}{3}\rho - \frac{K}{a^2} + \frac{\Lambda}{3}, \tag{1.22}$$

$$\frac{\ddot{a}}{a} = -\frac{4\pi G}{3}(\rho + 3p) + \frac{\Lambda}{3}. \tag{1.23}$$

Eqs.(1.22) and (1.23), the Friedmann equations, can be combined to give the continuity equation

$$\frac{d}{dt}(a^3\rho) + p\frac{d}{dt}(a^3) = 0, \tag{1.24}$$

which intuitively states energy conservation: the first term is the change in internal energy and the second term is the pressure work. This is the first law of thermodynamics in the absence of heat flow (which would violate isotropy).

The universe is filled with different matter components (barotropic fluids) that will provide the last equation needed to solve the set of equations, the equation of state

$$w = \frac{p}{\rho}\,, \tag{1.25}$$

which relates the energy density and pressure of the various possible cosmological fluids. For cold dark matter (CDM) ($w = 0$), radiation ($w = 1/3$), vacuum energy ($w = -1$) or for any other barotropic fluid with a dynamical equation of state $w(a)$, the solution to Eq.(1.24) is

$$\rho(a) = \rho(a_0) e^{-\int_{a_0}^{a} 3(1+w(a))a^{-1}da}\,. \tag{1.26}$$

ΛCDM model

The simplest model capable of explaining several evidences observed in our real universe is ΛCDM. It is a universe filled with two main components of unknown nature: the cosmological constant Λ, responsible for the late accelerated expansion of the universe, and CDM, as the main component driving structure formation and of structure itself. In the ΛCDM model Eq.(1.22) becomes

$$\left(\frac{\dot{a}}{a}\right)^2 = H^2 = \frac{8\pi G}{3}\left[\rho_r \left(\frac{a_0}{a}\right)^4 + \rho_m \left(\frac{a_0}{a}\right)^3 + \rho_\Lambda\right]\,, \tag{1.27}$$

where ρ_i denotes the energy density of the different components of the energy budget today, at $t = t_0$. We will also use the conventional normalisation for the scale factor, $a_0 \equiv 1$.

For a flat universe, the critical density today is [2, 5]

$$\rho_{crit} = \frac{3H_0^2}{8\pi G} = 1.1 \times 10^{-5} h^2 \,\frac{\text{protons}}{\text{cm}^3}\,, \tag{1.28}$$

and we use the critical density to define the dimensionless density parameter

$$\Omega_i = \frac{\rho_i}{\rho_{crit}}\,. \tag{1.29}$$

Then the Friedmann equation (1.27) becomes

$$H^2(a) = E^2 H_0^2 = H_0^2\left[\Omega_r \left(\frac{a_0}{a}\right)^4 + \Omega_m \left(\frac{a_0}{a}\right)^3 + \Omega_\Lambda\right]\,. \tag{1.30}$$

A combination of several cosmological observations have allowed the Planck team to estimate the density parameters of the ΛCDM model with high precision [6]. Their central values are $\Omega_r = 9.4\times10^{-5}$, $\Omega_m = 0.31$ and $\Omega_\Lambda = 0.68$. The matter density parameter, Ω_m, has contributions around 0.04 of ordinary (baryonic) matter and 0.27 of DM. [2, 5].

1.2 Cosmological perturbation theory

So far, we considered the universe as perfectly homogeneous. To understand the formation and evolution of large-scale structures, we have to introduce inhomogeneities. As long as these perturbations remain relatively small, we can define a metric that deviates from the FLRW spacetime as the sum of the unperturbed FLRW part plus something else, that is usually called the perturbed metric.

$$g_{\mu\nu} = g^{(0)}_{\mu\nu} + \delta g_{\mu\nu}. \tag{1.31}$$

Then, by using the flat FLRW background spacetime with no curvature,

$$ds^2 = a^2(\tau)\left[-d\tau^2 + \delta_{ij}dx^i dx^j\right], \tag{1.32}$$

the perturbed metric is

$$ds^2 = a^2(\tau)\left[-(1-2A)d\tau^2 + 2B_i dx^i d\tau - (\delta_{ij} + h_{ij})dx^i dx^j\right]. \tag{1.33}$$

where A, B_i and h_{ij} are functions of space and time.

Now that we have defined the perturbed metric it is important to perform a scalar-vector-tensor (SVT) decomposition of the perturbations, that will allow us to get the Einstein equations for scalars, vectors and tensors unmixed at linear order and will allow us to treat them separately [2].

For the 3-vector B_i we can split it into the gradient of a scalar plus a divergenceless vector

$$B_i = \partial_i B + \hat{B}_i, \tag{1.34}$$

with $\partial^i \hat{B}_i = 0$.

The rank-2 simmetric tensor can be written as

$$h_{ij} = 2C\delta_{ij} + 2\left(\partial_i\partial_j - \frac{1}{3}\delta_{ij}\nabla^2\right)E + \left(\partial_i\hat{E}_j + \partial_j\hat{E}_i\right) + 2\hat{E}_{ij}, \tag{1.35}$$

where the tensor perturbation is traceless, $\hat{E}^i_i = 0$, $\partial^i\hat{E}_i$ and $\partial^i\hat{E}_{ij} = 0$.

This allow us to re-writte the 10 degrees of freedom of the metric as 4 scalar, 4 vectors and 2 tensors components.

Here we have to take into account a small consideration. The metric perturbations that we defined Eq.(1.33) were made by choosing a specific time slicing of the spacetime and a defined specific spatial coordinates on this time slice. Then, by making a different choice of coordinates we can change the values of these perturbations variables and we can introduce fake perturbations or even remove true ones. For example, if we take the homogeneous FLRW metric Eq.(1.32) and make the following change of the spatial coordinates $x^i \to \tilde{x}^i = x^i + \epsilon^i(\tau, \vec{x})$, where we assume ϵ^i to be small and therefore amenable to being treated as a perturbation. With $dx^i = d\tilde{x}^i - \partial_\tau\epsilon^i d\tau - \partial_k\epsilon^i d\tilde{x}^k$, the FLRW metric Eq.(1.32) becomes

$$ds^2 = a^2(\tau)\left[-d\tau^2 + 2\partial_\tau\epsilon^i d\tilde{x}^i d\tau - \left(\delta_{ij} + \partial_i\epsilon_j + \partial_j\epsilon_i\right)d\tilde{x}^i d\tilde{x}^j\right], \tag{1.36}$$

dropping the quadratic terms in ϵ^i. We have apparently introduced the metric perturbations $B_i = \partial_\tau\epsilon_i$ and $\hat{E}_i = \epsilon_i$, but these are just fictitious gauge modes that can be removed by going back to the old coordinates. In the same way, we can change our time slicing, $\tau \to \tau + \epsilon^0(\tau, \vec{x})$, and the homogeneous

energy density of the universe gets perturbed, $\rho(\tau) \to \rho(\tau + \epsilon^0(\tau, \vec{x})) = \bar{\rho}(\tau) + \bar{\rho}^{'}\epsilon^0$. This means that a change of the time coordinate can lead to fake density perturbations, $\delta\rho = \bar{\rho}^{'}\epsilon^0$. On the other hand, a real perturbation in the perturbed metric can be removed in the same way by a change of coordinates.

These examples show us that we need a more physical way to identify true perturbations. One way to avoid the gauge problems is to define a special combination of metric perturbations that do not transform under a change of coordinates. These are called Bardeen variables. Another alternative is to fix the gauge and keep track of all perturbations.

1.2.1 Synchronous gauge and Newtonian gauge

Throughout this dissertation we will consider two gauges, the synchronous gauge and the Newtonian gauge, because they are the ones that will be used later in CLASS. Also, thanks to the SVT decomposition, we are able to only consider the scalar perturbations, since vector and tensor perturbations are not of much interest in current DE research. In this case, Eq.(1.33) becomes,

$$ds^2 = a^2(\tau)\left[-(1+2A)\,d\tau^2 + 2\partial_i B d\tau dx^i + [(1+2C)\delta_{ij} + 2\partial_i\partial_j E]\,dx^i dx^j\right]. \tag{1.37}$$

The synchronous gauge is the most commonly used gauge, adopted by Lifshitz [3]. For this gauge the components g_{00} and g_{0i} of the metric tensor are by definition unperturbed, i.e., $A = B = 0$, and the line element is usually written as

$$ds^2 = a^2(\tau)\left[-d\tau^2 + [(1+2C)\delta_{ij} + 2\partial_i\partial_j E]\,dx^i dx^j\right]. \tag{1.38}$$

These two scalar fields (C and E) characterise the scalar mode of h_{ij}. The scalar mode of h_{ij} is usually written as a Fourier integral, as a function of two fields $h(\vec{k}, \tau)$ and $\eta(\vec{k}, \tau)$:

$$h_{ij}(\vec{x}, \tau) = \int d^3k e^{i\vec{k}\vec{x}}\left[\hat{k}_i\hat{k}_j h(\vec{k}, \tau) + (\hat{k}_i\hat{k}_j - \frac{1}{3}\delta_{ij})6\eta(\vec{k}, \tau)\right] \tag{1.39}$$

In addition, to fix the gauge we need to impose the extra condition that the synchronous gauge is comoving with pressureless species i.

For the Newtonian gauge we fix two of the scalar perturbations to zero $E = B = 0$, which gives the metric:

$$ds^2 = a^2(\tau)\left[-(1+2\Psi)\,d\tau^2 + (1-2\Phi)\delta_{ij}dx^i dx^j\right], \tag{1.40}$$

where we renamed $A \equiv \Psi$ and $C \equiv -\Phi$, as it is usually defined in the literature.

With all this set we will now derive the first order Einstein equations using the Newtonian gauge.

To do that we decompose the Einstein tensor G^μ_ν and the energy-momentum tensor T^μ_ν into a background part and a perturbed part

$$G^\mu_\nu = G^{\mu(0)}_\nu + \delta G^\mu_\nu \tag{1.41}$$

$$T^\mu_\nu = T^{\mu(0)}_\nu + \delta T^\mu_\nu. \tag{1.42}$$

The background part was already solved in the previous section. The perturbed part of the Einstein equation is then given by

$$\delta G^{\mu}_{\nu} = 8\pi G \delta T^{\mu}_{\nu}. \tag{1.43}$$

First we need to calculate the perturbed Christoffel symbols

$$\delta\Gamma^{\mu}_{\nu\lambda} = \frac{1}{2}\delta g^{\mu\alpha}\left(g_{\alpha\nu,\lambda} + g_{\alpha\delta,\nu} - g_{\nu\lambda,\alpha}\right) + \frac{1}{2}g^{\mu\alpha}\left(\delta g_{\alpha\nu,\lambda} + \delta g_{\alpha\delta,\nu} - \delta g_{\nu\lambda,\alpha}\right). \tag{1.44}$$

For the the metric Eq.(1.40), the non-zero components are

$$\delta\Gamma^{0}_{ij} = \delta_{ij}\left[2\mathcal{H}\left(\Phi - \Psi\right) + \Phi'\right], \tag{1.45}$$

$$\delta\Gamma^{0}_{00} = \Psi', \tag{1.46}$$

$$\delta\Gamma^{0}_{0i} = \delta\Gamma^{i}_{00} = \Psi_{,i}, \tag{1.47}$$

$$\delta\Gamma^{i}_{j0} = \delta^{i}_{j}\Phi'. \tag{1.48}$$

Here a prime represents the derivative with respect to the conformal time τ. Next, we derive the perturbation in the Ricci tensor and scalar

$$\delta R_{\mu\nu} = \delta\Gamma^{\alpha}_{\mu\nu,\alpha} - \delta\Gamma^{\alpha}_{\mu\alpha,\nu} + \delta\Gamma^{\alpha}_{\mu\nu}\Gamma^{\beta}_{\alpha\beta} + \Gamma^{\alpha}_{\mu\nu}\delta\Gamma^{\beta}_{\alpha\beta} - \delta\Gamma^{\alpha}_{\mu\beta}\Gamma^{\beta}_{\alpha\nu} - \Gamma^{\alpha}_{\mu\beta}\delta\Gamma^{\beta}_{\alpha\nu} \tag{1.49}$$

$$\delta R = \delta g^{\mu\alpha}R_{\alpha\mu} + g^{\mu\alpha}\delta R_{\alpha\mu}, \tag{1.50}$$

with this we obtain the perturbed Einstein tensor

$$\delta G_{\mu\nu} = \delta R_{\mu\nu} - \frac{1}{2}\delta g_{\mu\nu}R - \frac{1}{2}g_{\mu\nu}\delta R \tag{1.51}$$

$$\delta G^{\mu}_{\nu} = \delta g^{\mu\alpha}G_{\alpha\nu} + g^{\mu\alpha}\delta G_{\alpha\nu}. \tag{1.52}$$

Inserting all these quantities, we can write the perturbed Einstein tensor as function of the metric components [1]

$$\delta G^{0}_{0} = 2a^{-2}\left[3\mathcal{H}\left(\mathcal{H}\Psi - \Phi'\right) + \nabla^{2}\Phi\right], \tag{1.53}$$

$$\delta G^{0}_{i} = 2a^{-2}\nabla_{i}\left(\Phi' - \mathcal{H}\Psi\right), \tag{1.54}$$

$$\delta G^{i}_{j} = 2a^{-2}\left[\left(\mathcal{H}^{2} + 2\mathcal{H}'\right)\Psi + \mathcal{H}\Psi' - \Phi'' - 2\mathcal{H}\Phi'\right]\delta^{i}_{j} + a^{-2}\left[\nabla^{2}\left(\Psi + \Phi\right)\delta^{i}_{j} - \nabla^{i}_{j}\left(\Psi + \Phi\right)\right]. \tag{1.55}$$

Notice that we defined the conformal Hubble function $\mathcal{H} \equiv Ha$.

Now we will take a look at the perturbed energy momentum tensor $T_{\mu\nu}$, where we will consider it to be the energy momentum tensor of a single perfect fluid. As we will see later, this is what we need to implement a UDM model in CLASS.

For a perfect fluid, the energy momentum tensor is

$$T^{\mu}_{\nu} = T^{\mu(0)}_{\nu} + \delta T^{\mu}_{\nu}, \tag{1.56}$$

where the unperturbed part is given by

$$T^{\mu(0)}_{\nu} = (\rho + P)\,\bar{u}^{\mu}\bar{u}_{\nu} + P\delta^{\mu}_{\nu}. \tag{1.57}$$

The perturbed part is then

$$\delta T^{\mu}_{\nu} = (\delta\rho + \delta P)\bar{u}^{\mu}\bar{u}_{\nu} + (\rho + P)(\bar{u}^{\mu}\delta u_{\nu} + \bar{u}_{\nu}\delta u^{\mu}) + \delta P\delta^{\mu}_{\nu}, \tag{1.58}$$

that we can rewrite as

$$\delta T^{\mu}_{\nu} = \rho\left[\delta(1 + c_s^2)\bar{u}_{\nu}\bar{u}^{\mu} + (1 + w)(\delta u_{\nu}\bar{u}^{\mu} + \bar{u}_{\nu}\delta u^{\mu}) + c_s^2\delta\delta^{\mu}_{\nu}\right]. \tag{1.59}$$

Here we introduced important quantities, the density contrast and the sound speed

$$\delta \equiv \frac{\delta\rho}{\rho}, \tag{1.60}$$

$$c_s^2 \equiv \frac{\delta P}{\delta\rho}. \tag{1.61}$$

If the fluid is barotropic, $P = P(\rho)$, then $c_s^2 = P'/\rho'$.

We also have to define the 4-velocity vector $\bar{u}^{\mu} = a^{-1}\delta^0_{\mu}$. Since $g_{\mu\nu}u^{\mu}u^{\nu} = 1$ and $\bar{g}_{\mu\nu}\bar{u}^{\mu}\bar{u}^{\nu} = 1$, we have at linear order

$$\delta g_{\mu\nu}\bar{u}^{\mu}\bar{u}^{\nu} + 2\bar{u}_{\mu}\delta u^{\mu} = 0. \tag{1.62}$$

For the Newtonian gauge $\delta g_{00} = 2a^2\Psi$, we get $\delta u^0 = -\Psi a^{-1}$, and we write the spatial part of the perturbed 4-velocity vector as $\delta u^i \equiv v^i/a$, with $v^i \equiv dx^i/d\tau$. So we have

$$u^{\mu} = a^{-1}\left[(1 - \Psi)\,, v^i\right], \tag{1.63}$$

$$u_{\mu} = g_{\mu\nu}u^{\nu} = \left[-a\,(1 + \Psi)\,, av_i\right]. \tag{1.64}$$

The perturbed components of the energy-momentum tensor are then

$$\delta T^0_0 = -\delta\rho \tag{1.65}$$

$$\delta T^0_i = -\delta T^i_0 = (1 + w)\rho v^i \tag{1.66}$$

$$\delta T^1_1 = \delta T^2_2 = \delta T^3_3 = c_s^2\delta\rho. \tag{1.67}$$

We finally obtain the perturbed Einstein equations

$$3\mathcal{H}\left(\mathcal{H}\Psi - \Phi'\right) + \nabla^2\Phi = 4\pi G a^2\delta T^0_0 = -4\pi G a^2\rho\delta, \tag{1.68}$$

$$\nabla^2 \left(\Phi' - \mathcal{H}\Psi\right) = 4\pi G a^2(\rho + P)\theta = 4\pi G a^2(1+w)\rho\theta, \tag{1.69}$$

$$\Psi = -\Phi, \tag{1.70}$$

$$\Phi'' + 2\mathcal{H}\Phi' - \mathcal{H}\Psi' - \left(\mathcal{H}^2 + 2\mathcal{H}'\right)\Psi = -4\pi G a^2 c_s^2 \rho\delta, \tag{1.71}$$

where we introduced the velocity divergence $\theta \equiv \nabla_i v^i$, where in the synchronous gauge $\theta_i = 0$ for any pressureless species.

The energy-momentum tensor satisfies the identity $\nabla_\mu T^\mu_\nu = 0$. And for the perturbed part it writes

$$\nabla_\mu \delta T^\mu_\nu = \delta T^\mu_{\nu,\mu} - \delta\Gamma^\alpha_{\nu\beta} T^\beta_\alpha - \Gamma^\alpha_{\nu\beta}\delta T^\beta_\alpha + \delta\Gamma^\alpha_{\beta\alpha} T^\beta_\nu + \Gamma^\alpha_{\beta\alpha}\delta T^\beta_\nu = 0. \tag{1.72}$$

For the component $\nu = 0$, we obtain a continuity equation

$$\partial_\tau \left(\delta\rho\right) + 3\mathcal{H}\left(\delta\rho + \delta P\right) = -\left(\rho + P\right)\left(\theta + 3\Phi'\right), \tag{1.73}$$

and using the unperturbed continuity equation (1.24) we get

$$\delta' + 3\mathcal{H}\left(c_s^2 - w\right)\delta = -\left(1+w\right)\left(\theta + 3\Phi'\right). \tag{1.74}$$

The equation $\nabla_\mu \delta T^\mu_\nu = 0$ for $\nu = i$ leads to

$$\theta' + \left[\mathcal{H}(1-3w) + \frac{w'}{1+w}\right]\theta = -\nabla^2\left(\frac{c_s^2}{1+w}\delta + \Psi\right). \tag{1.75}$$

We can rewrite the perturbed Einstein equations (1.68)-(1.71) and the conservation equations (1.74), (1.75) in Fourier space, yielding

$$3\mathcal{H}\left(\mathcal{H}\Psi - \Phi'\right) + k^2\Phi = 4\pi G a^2 \delta T^0_0 = -4\pi G a^2 \rho\delta, \tag{1.76}$$

$$k^2\left(\Phi' - \mathcal{H}\Psi\right) = 4\pi G a^2(\rho + P)\theta = 4\pi G a^2(1+w)\rho\theta, \tag{1.77}$$

$$\Psi = -\Phi, \tag{1.78}$$

$$\Phi'' + 2\mathcal{H}\Phi' - \mathcal{H}\Psi' - \left(\mathcal{H}^2 + 2\mathcal{H}'\right)\Psi = -4\pi G a^2 c_s^2 \rho\delta, \tag{1.79}$$

$$\delta' + 3\mathcal{H}\left(c_s^2 - w\right)\delta = -\left(1+w\right)\left(\theta + 3\Phi'\right), \tag{1.80}$$

$$\theta' + \left[\mathcal{H}(1-3w) + \frac{w'}{1+w}\right]\theta = -k^2\left(\frac{c_s^2}{1+w}\delta + \Psi\right). \tag{1.81}$$

Following the same procedure for the synchronous gauge we arrive at an equivalent set of equations [7]

$$k^2\eta - \frac{1}{2}\mathcal{H}h' = 4\pi G a^2 \delta T_0^0 = -4\pi G a^2 \rho \delta, \tag{1.82}$$

$$k^2\eta' = 4\pi G a^2 (\rho + P)\theta = 4\pi G a^2 (1+w)\rho\theta, \tag{1.83}$$

$$h'' + 2\mathcal{H}h' - 2k^2\eta = -8\pi G a^2 \delta T_i^i = -24\pi G a^2 c_s^2 \rho\delta, \tag{1.84}$$

$$h'' + 6\eta'' + 2\mathcal{H}(h' + 6\eta') - 2k^2\eta = -24\pi G(\rho + P)\sigma, \tag{1.85}$$

$$\delta' + 3\mathcal{H}\left(c_s^2 - w\right)\delta = -\left(1+w\right)\left(\theta + \frac{h'}{2}\right), \tag{1.86}$$

$$\theta' + \left[\mathcal{H}(1-3w) + \frac{w'}{1+w}\right]\theta = k^2 \frac{c_s^2}{1+w}\delta. \tag{1.87}$$

The conservation equations both in the synchronous and in the Newtonian gauge are valid for a single uncoupled fluid, or for the total δ and θ that include all fluids.

1.2.2 Random Fields

It is important to note that all perturbed quantities are random fields and not deterministic quantities. Indeed, the structures that we see today arrive from the quantum fluctuations of the energy density from the very beginning of the universe. At that time, the energy density at each point results from a stochastic process. As such, initial conditions for δ as a function of spatial location cannot be known, but only its statistical distribution. The primordial distributions are assumed to be Gaussian and are described by the mean, which is $\langle\delta\rangle = 0$ by definition, and the variance. The variance defines a matrix in real space (the covariance matrix, a 2-point quantity in the space of spatial coordinates) and it is the central quantity to describe structure formation in cosmology. This implies that, due to the randomness of initial conditions, the goal of structure formation studies is not to determine the values of δ at given locations, but to determine the covariance matrix of the δ field.

As an example let us start by considering N galaxies in a volume V (assuming that galaxies trace the δ field). We can calculate the average numerical density as $\rho_0 = N/V$, but this will not tell us if the N points are evenly distributed across the volume or if they are distributed inhomogeneously. Indeed, that information is contained in the covariance matrix. What we can do is then analyse a smaller volume dV inside the volume V, where $\rho_0 dV$ is still the average number of points in this infinitesimal volume. Let us define $dN_{ab} = \langle n_a n_b\rangle$ as the product of the number of points in one volume times the number of points in the other volume, separated by r_{ab}

$$dN_{ab} = \langle n_a n_b\rangle = \rho_0^2 dV_a dV_b \left[1 + \xi(r_{ab})\right]. \tag{1.88}$$

The excess number of pairs in the volumes dV_a and dV_b, compared with the number of pairs for independent distributions of points randomly distributed is determined by the factor $\xi(r_{ab})$ implicitly defined in Eq. (1.88). This is called the 2-point correlation function $\xi(r_{ab})$ and corresponds to the coefficients of the covariance matrix.

This average could be evaluated in two ways. We can average over many realisations of the distribution (like in N-body simulations), selecting in each realisation the volumes dV_a and dV_b at the same

location and then average the pair number $n_a n_b$. This is called the ensemble average. We can also take the pairs at different locations in a single realisation, separated by the same distance r_{ab}. This is called the sample average. If the regions are so distant that they are uncorrelated, then we can consider that this is the same thing as considering different realisations and both methods will give the same result. However, we only know the existence of one universe and we are not completely sure if the regions are really uncorrelated and we cannot confirm this with an ensemble average. This problem is more important when we are studying large scales, but still, the correlation function is a very useful estimator and we will consider that the properties of the sample distribution are a good approximation to the ensemble ones.

Assuming the number density of galaxies trace the density contrast δ, Eq.(1.88) may be written as

$$\xi(r_{ab}) = \frac{dN_{ab}}{\rho_0^2 dV_a dV_b} - 1 = \langle \delta(r_a)\delta(r_b)\rangle, \tag{1.89}$$

and, if we want to do a sample average, we have to average over all possible positions

$$\xi(r) = \frac{1}{V}\int \delta(y)\delta(y+r)dV_y. \tag{1.90}$$

In our case, we are interested in having a function that allows us to study the amplitude of the density contrast. Also, instead of using sizes defined by the separation between points we would like to use a set of independent characteristic sizes, that we will usually call scales. One excellent choice are a set of Fourier modes.

For the density contrast of a density field $\delta(x)$, the Fourier transform is

$$\delta_k = \frac{1}{V}\int \delta(x)e^{-ikx}dV. \tag{1.91}$$

This will allow us to introduce a well known quantity called the power spectrum

$$P(k) = V|\delta_k|^2 = V\delta_k\delta_k^* = \frac{1}{V}\int \delta(x)\delta(y)e^{-ik(x-y)}dV_x dV_y, \tag{1.92}$$

and by defining $r = x - y$ and from Eq.(1.90) we get

$$P(k) = \int \xi(r)e^{-ikr}dV, \tag{1.93}$$

meaning that the power spectrum is the Fourier transform of the correlation function.

If we assume spacial isotropy, the correlation function will only depend on the modulus $r = |r|$ and the power spectrum will depend only on $k = |k|$

$$P(k) = \int \xi(r)r^2dr\int_0^\pi e^{-ikrcos\theta}sin\theta d\theta\int_0^{2\pi} d\phi = 4\pi\int \xi(r)\frac{sinkr}{kr}r^2dr. \tag{1.94}$$

The power spectrum is a very important quantity in cosmology due to its ability to describe the level of clustering. It can be measured in the observational data of a given cosmological field $g(\vec{x})$, such as the CMB temperature field in CMB data, or the galaxy ellipticity field in the gravitational lensing data, or in the galaxy density field of galaxy clustering data, among many others.

In order to test the viability of our UDM model and constrain its parameters, we will compare its structure formation predictions with observed data. To do this, we need first to compute the power spectrum in the UDM model.

Chapter 2

Unified Dark Matter-Energy models

There are several theoretical ideas, alternatives to ΛCDM, proposing various forms of DE to explain the origin of the late-time acceleration of the universe. ΛCDM may be considered as the simplest solution, borrowing Einstein's idea of vacuum energy, namely cosmological the constant Λ. However, there are two problems that arise with the cosmological constant and motivates us to study other alternatives. The first one is called the fine-tuning problem and the second one the coincidence problem (see for e.g. [1, 9]).

In Quantum Field Theory (QFT) and therefore in modern Particle Physics, the notion of empty space has been replaced by a vacuum state, defined to be the ground state of a collection of quantum fields (meaning the lowest energy density). These quantum fields exhibit zero-point fluctuations everywhere in space. These zero-point fluctuations of the quantum fields, as well as other 'vacuum phenomena' of QFT, give rise to an enormous vacuum energy density ρ_{vac}. This vacuum energy density is believed to act as a contribution to the cosmological constant Λ. Several observations [6, 10, 11] show us that this Λ is in fact very small, $\mid \Lambda \mid < 10^{-56} cm^2$. This constraint can be interpreted as a constraint on the vacuum energy density in QFT, $\mid \rho_{vac} \mid < 10^{-29} g/cm^3 \sim 10^{-47} \mathrm{GeV}^4$. However, we can theoretically estimate the various contributions to the vacuum energy density in QFT, and predictions exceed the observational bound by at least 40 orders of magnitude. This large discrepancy is the main problem associated to the cosmological constant.

The second problem addresses the single question of why ρ_Λ is not only small but of the same order of magnitude of the matter energy density present in the universe, ρ_m.

One of the first alternative models that tried to solve these problems was quintessence (see e.g. [12–16]). The name quintessence means the fifth element, besides baryons, DM, radiation and spatial curvature. This fifth element is the missing cosmic energy density component with negative pressure that we are searching for today. The basic idea of quintessence is that DE is in the form of a time varying scalar field which is slowly rolling down toward its potential minimum. The quintessence model assumes a canonical kinetic energy and the potential energy term in the action. By modifying this canonical kinetic energy term, we can get a non-canonical (non-linear) kinetic energy of the scalar field that can drive the negative pressure without the help of potential terms. The non-linear kinetic energy terms are thought to be small and are usually ignored because the Hubble expansion damps the kinetic energy density over time. However, it is possible to have a dynamical attractor solution which forces the non-linear terms to remain non-negligible. These other kind of models are called k-essence (see e.g. [17, 18]).

There are other types of models like the Coupled Dark Energy models that consider an interaction between DM and DE [19, 20], or f(R) gravity [21–23] that consists of the modification of gravity on large scales, or even other ideas like the DGP model [24, 25] and the inhomogeneous LTB model [26, 27].

The alternative here considered are the Unified Dark Matter-Energy models (UDM), also known as quartessence. These models propose the interesting idea of considering a single fluid that behaves as DM and DE, studying the possibility that the two unknown components of the universe are in fact one. That idea, besides being elegant, also releases us from the coincidence problem. Most of these models are characterised by a sound speed, whose value and evolution imprints oscillations on the matter power spectrum.

The first UDM model proposed was the Generalised Chaplygin Gas (GCG) [28, 29], which can produce cosmic acceleration, successefully explaining the late-time acceleration of the universe. However, this model has a speed of sound which may become significantly large during the evolution of the universe preventing the formation of structure [30]. As we will later see, having a speed of sound different from zero gives rise to two regimes: scales where the density contrast grows and scales where there is an oscillatory solution, preventing the growth. The threshold between the two regimes is known as the Jean scale. In the original GCG model the Jean scale was too large, preventing the formation of structure. To evade this problem, four main solutions have been considered to make the GCG viable: the vanishing sound speed models, also known as silent Chaplygin Gas [31]; the decomposition models, where the UDM models are seen as an interaction between DM and the vacuum energy; the clustering GCG model [32]; and the backreaction [33]. The decomposition models can be divided into two main models: the Barotropic model [34], that unfortunately does not solve the clustering problem, and the geodesic flow model [34–36].

Besides the alternatives considered for the CGC many other UDM models were proposed (see e.g. [37, 38]). Some of them have a non-canonical kinetic term in the Lagrangian (a kinetic term $f(\dot{\psi}^2)$ instead of $\dot{\psi}^2/2$), that allows to build a model with a small effective sound speed and eventually allow structure formation. Another alternative considered are the UDM models with fast transition. These models have a fast transition between a CDM-like epoch, with an Einstein-de Sitter evolution, and an accelerated DE-like epoch. This fast transition results in having a speed of sound different from zero but only for a short period of time and therefore a Jeans scale large enough to allow structure to form. By prescibing an evolution for the equation of state w, for the pressure p or for the energy density ρ we can define the dynamics of the UDM model. The first UDM model with fast transition was proposed in [39], where it was prescribed the evolution of p. In this model the UDM fluid was considered to be barotropic $p = p(\rho)$ and the perturbations were adiabatic. A second UDM model with fast transition was presented in [40]. This model was built from a k-essence scalar field. In this model it was also prescribed an evolution for p but non-adiabatic perturbations were considered. In this dissertation we considered a third UDM model proposed in [41]. The dynamics of this UDM fluid is prescribed through the energy density ρ, and it has adiabatic perturbations. This model was presented as a phenomenological model, with no discussion about the physical process behind the fast transition.

2.1 UDM with fast transition

At background level this UDM model can be created by considering it has a CDM behaviour at early times,

$$\rho = Aa^{-3}\,, \tag{2.1}$$

and it starts to show a different behaviour,

$$\rho = B + Ca^{-3}\,, \tag{2.2}$$

after a transition occurring at $a = a_t$.
Using the continuity equation Eq.(1.24), we can write the equation of state and the adiabatic sound speed $c_s^2 = \partial p/\partial\rho$ (which is an important quantity for structure formation) as a function of ρ and its derivatives only:

$$w = -\frac{a}{3}\frac{\rho^{'}}{\rho} - 1 \tag{2.3}$$

$$c_s^2 = \frac{dp}{d\rho} = \frac{a}{3}\frac{\rho^{''}}{\rho^{'}} - \frac{4}{3}\,, \tag{2.4}$$

and the model is completely specified by ρ.

To define ρ, we consider the desired limits defined in Eqs.(2.1) and (2.2), parametrised by its values at transition (ρ_t) and infinity ($\rho_{\Lambda udm}$),

$$\rho = \begin{cases} \rho_t \left(\dfrac{a_t}{a}\right)^3 & \text{if } a < a_t \\ \rho_{\Lambda udm} + (\rho_t - \rho_{\Lambda udm}) \left(\dfrac{a_t}{a}\right)^{3(1+\alpha)} & \text{if } a > a_t \end{cases}. \tag{2.5}$$

We can write them in a single equation by considering the Heaviside function,

$$\rho = \rho_t \left(\frac{a_t}{a}\right)^3 + \left[\rho_{\Lambda udm} + (\rho_t - \rho_{\Lambda udm}) \left(\frac{a_t}{a}\right)^{3(1+\alpha)} - \rho_t \left(\frac{a_t}{a}\right)^3\right] H(a - a_t)\,. \tag{2.6}$$

The parameter α parametrises the decreasing rate of $\rho(a)$ after the transition. We will focus on $\alpha = 0$,

$$\rho = \rho_t \left(\frac{a_t}{a}\right)^3 + \rho_\Lambda \left[1 - \left(\frac{a_t}{a}\right)^3\right] H(a - a_t)\,. \tag{2.7}$$

in case the UDM has a ΛCDM limit.

We will also consider a smooth continuous approximation to the Heaviside function given by

$$H(a - a_t) = \frac{1}{2} + \frac{1}{\pi}\arctan(\beta(a - a_t))\,. \tag{2.8}$$

This approximation produces a speed of sound $c_s^2 > 0$ and so it is physically realistic. Other approximations are discussed in Appendix B.

This UDM model has the desired general behaviour described in Eq. (2.5), and contains four parameters:

a_t: the scale factor at the transition.
ρ_t: the value of $\rho(a)$ at $a = a_t$.
$\rho_{\Lambda udm}$: the limiting value of $\rho(a)$ at $a \to \infty$.
β: parametrising the rapidity of the transition.

Only three of the parameters are independent due to the constraint imposed by the Friedmann equation:

$$\rho_t = \frac{1 - \sum_i \rho_{0,i} - \left[\rho_{\Lambda udm} - \rho_{\Lambda udm} a_t^{3(1+\alpha)}\right] H(1 - a_t)}{a_t^3 + \left[a_t^{3(1+\alpha)} - a_t^3\right] H(1 - a_t)}, \tag{2.9}$$

where the sum is the contribution from the various components of the universe (baryons, photons, neutrinos or any other component). This model has thus two extra parameters (a_t, β) as compared to ΛCDM.

It is important to note that a_t does not correspond to a time of transition from a DM-like regime to a DE-like regime. It just defines the time at which the second term of Eq.(2.7) is "activated".

We are interested in studying structure formation in the UDM scenario. For the evolution of the perturbations the UDM fluid will follow Eqs.(1.79) and (1.80) or Eqs.(1.85) and (1.86), depending on the gauge, where the equation of state and the sound speed are those of the UDM fluid.

Starting with the equations (1.75)-(1.80) in the Newtonian gauge, if we combine Eqs.(1.75), (1.77) and (1.78) we obtain an equation for ϕ

$$\phi'' + 3\mathcal{H}\left(1 + c_s^2\right)\phi'' + \left(c_s^2 k^2 + 3\mathcal{H}^2 c_s^2 + 2\mathcal{H}' + \mathcal{H}^2\right)\phi = 0. \tag{2.10}$$

On the other hand, if we combine Eqs.(1.75) and (1.76), we obtain the relativistic Poisson equation

$$k^2\phi = 4\pi G a^2 \rho \left[\delta + 3\mathcal{H}\left(1 + w\right)\theta/k^2\right]. \tag{2.11}$$

We can then transform δ of the Newtonian gauge into a gauge independent variable

$$\delta^* \equiv \delta + 3\mathcal{H}\left(1 + w\right)\theta/k^2, \tag{2.12}$$

and the Eq.(2.11) becomes

$$k^2\phi = 4\pi G a^2 \rho \delta^*. \tag{2.13}$$

Using Eq.(2.13) and its derivatives, we obtain an equation for δ^*

$$\delta''^* + \mathcal{H}\left(1 + 3c_s^2 - 6w\right)\delta'^* - \left[\frac{3}{2}\mathcal{H}^2\left(1 - c_s^2 - 3w^2 + 8w\right) - c_s^2 k^2\right]\delta^* = 0. \tag{2.14}$$

To see if δ^* grows, forming structure, or decays, we can start again from Eq. (2.10). Even if this equation cannot be solved for an arbitrary equation of state it is possible to derive asymptotic solutions. To do that it is useful to introduce a new variable in order to eliminate the friction term (the term proportional to ϕ')

$$u \equiv \frac{2\phi}{\sqrt{\rho + p}}. \tag{2.15}$$

By expressing $\mathcal{H}$ in terms of ρ and p via the conservation law $\rho' = -3\mathcal{H}(\rho + p)$ we obtain [43]

$$u'' + k^2 c_s^2 u - \frac{\theta''}{\theta} u = 0, \tag{2.16}$$

where

$$\theta \equiv \sqrt{\frac{\rho}{3(\rho + p)}} \frac{1}{a}. \tag{2.17}$$

The solution of Eq.(3.16) may be a growing solution or an oscillatory solution, depending on the scale. The Jeans scale, defined as [40]

$$k_{\rm J}^2 \equiv \left| \frac{\theta''}{c_s^2 \theta} \right|, \tag{2.18}$$

is the threshold between the two behaviours. Density contrast will grow on scales larger than $k_{\rm J}$ and will not grow efficiently (will oscillate) on smaller scales. Models with large $k_{\rm J}$ (small scales) are then the most favourable to produce structure. Models with a low sound speed (CDM-like) are obviously favourable for structure formation, and as we may have guessed, they have a large value of $k_{\rm J}$.

The Jean scale, Eq.(2.18) may be computed as function of the derivatives of ρ, which in turn introduces dependencies on w and c_s^2. After some lenghty calculations we obtain an explicit form for $k_{\rm J}^2$, (see also, [39])

$$k_{\rm J}^2 = \frac{3}{2}\rho a^2 \frac{(1+w)}{c_{\rm s}^2} \left| \frac{1}{2}(c_{\rm s}^2 - w) - \rho \frac{dc_{\rm s}^2}{d\rho} + \frac{3(c_{\rm s}^2 - w)^2 - 2(c_{\rm s}^2 - w)}{6(1+w)} + \frac{1}{3} \right| . \tag{2.19}$$

From this equation we conclude that we can obtain a large $k_{\rm J}^2$, that in principle allows structure formation, not only when we have a speed of sound equal to zero but also when the speed of sound changes rapidly. This is the motivation to build UDM models with fast transition.

An important subject to consider when solving numerically the differential equations of the perturbations related to each fluid are the initial conditions. Here we will closely follow [7], where we can find an excellent study on cosmological perturbation theory. Numerically, the integration starts at early times, when a given k-mode is still outside the horizon ($k\tau \ll 1$, where $k\tau$ is dimensionless), deep in the radiation epoch. At that time, the expansion rate is $\dot{a}/a = \tau^{-1}$ and massive neutrinos are relativistic and the UDM fluid and the baryons all make a very small contribution to the total energy density ($\bar{\rho_t} = \bar{\rho_\gamma} + \bar{\rho_\nu}$). From the differential equations (1.81), (1.83) and the perturbed Boltzmann equation for photons and neutrinos (which are not described here) we can analytically extract the time-dependence of the metric and density perturbations on super-horizon scales and end up with the following set of equations in the synchronous gauge

$$\tau^2 h'' + \tau h' + 6\left[(1 - R_\nu)\,\delta_\gamma + R_\nu \delta_\nu\right] = 0, \tag{2.20}$$

$$\delta_\gamma' + \frac{4}{3}\theta_\gamma + \frac{2}{3}h' = 0, \tag{2.21}$$

$$\theta'_\gamma - \frac{1}{4}k^2\delta_\gamma = 0, \tag{2.22}$$

$$\delta'_\nu + \frac{4}{3}\theta_\nu + \frac{2}{3}h' = 0, \tag{2.23}$$

$$\theta'_\nu - \frac{1}{4}k^2\left(\delta_\nu - 4\sigma_\nu\right) = 0, \tag{2.24}$$

$$\sigma'_\nu - \frac{2}{15}\left(2\theta_\nu + h' + 6\eta'\right) = 0, \tag{2.25}$$

where $R_\nu \equiv \bar{\rho_\nu}/\left(\bar{\rho_\gamma} + \bar{\rho_\nu}\right)$.

For N_ν flavour of neutrinos, after the electron-positron pair annihilation and before the massive neutrinos become nonrelativistic, $\bar{\rho_\nu}/\bar{\rho_\gamma} = (7N_\nu/8)\,(4/11)^{4/3}$ is constant.

At first order, and neglecting the terms $\propto k^2$ in the equations above, we get $\theta'_\nu = \theta'_\gamma = 0$, and these equations can be combined into a single fourth-order equation for h

$$\tau\frac{d^4h}{d\tau^4} + 5\frac{d^3h}{d\tau^3} = 0, \tag{2.26}$$

with four power laws solutions allowing us to obtain the following equations

$$h = A + B\,(k\tau)^{-2} + C\,(k\tau)^2 + D\,(k\tau)\,, \tag{2.27}$$

$$\delta \equiv (1 - R_\nu)\,\delta_\gamma + R_\nu\delta_\nu = -\frac{2}{3}B\,(k\tau)^{-2} - \frac{2}{3}C\,(k\tau)^2 - \frac{1}{6}D\,(k\tau)\,, \tag{2.28}$$

$$\theta \equiv (1 - R_\nu)\,\theta_\gamma + R_\nu\theta_\nu = -\frac{3}{8}Dk. \tag{2.29}$$

The other metric perturbation η can also be obtained

$$\eta = 2C + \frac{3}{4}D\,(k\tau)^{-1}\,. \tag{2.30}$$

A general expression for the time depending of the four eigenmodes is derived in [8] and they showed that the first two modes (A and B) are gauge modes and can be eliminated by a coordinate transformation and the other two modes (C and D) are physical modes of density perturbations in the radiation epoch. In the synchronous gauge both appear as growing modes in the radiation epoch but in the matter epoch D decays [13], meaning that the $C(k\tau)^2$ mode dominates at later times.

In that sense, we define our initial conditions so that only the fastest growing mode is present and we obtain the initial conditions at super-horizon-sized perturbations

$$\delta_\gamma = -\frac{2}{3}C(k\tau)^2, \quad \delta_{cdm} = \delta_b = \frac{3}{4}\delta_\nu = \frac{3}{4}\delta_\gamma, \tag{2.31}$$

$$\theta_{cdm} = 0, \quad \theta_\gamma = \theta_b = -\frac{1}{18}Ck^4\tau^3, \quad \theta_\nu = \frac{23 + 4R_\nu}{15 + 4R_\nu}\theta_\gamma, \tag{2.32}$$

$$\sigma_\nu = \frac{4C}{3\left(15+4R_\nu\right)}\left(k\tau\right)^2, \tag{2.33}$$

$$h = C(k\tau)^2, \quad \eta = 2C - \frac{5+4R_\nu}{6\left(15+4R_\nu\right)}C\left(k\tau\right)^2. \tag{2.34}$$

And for the Newtonian gauge we obtain

$$\delta_\gamma = -\frac{40C}{15+4R_\nu} = -2\psi, \quad \delta_{cdm} = \delta_b = \frac{3}{4}\delta_\nu = \frac{3}{4}\delta_\gamma, \tag{2.35}$$

$$\theta_{cdm} = \theta_\gamma = \theta_\nu = \theta_b = -\frac{10C}{15+4R_\nu}k^2\tau = \frac{1}{2}k^2\tau\psi, \tag{2.36}$$

$$\sigma_\nu = \frac{4C}{3\left(15+4R_\nu\right)}\left(k\tau\right)^2 = \frac{1}{15}\left(k\tau\right)^2\psi, \tag{2.37}$$

$$\psi = \frac{20C}{15+4R_\nu}, \quad \phi = \left(1+\frac{2}{5}R_\nu\right)\psi. \tag{2.38}$$

The initial conditions for the UDM fluid are then very straightforward. Since we have all the potentials as a dependency on the growing mode C, we can replace these potentials in the differential equations for the UDM fluid in the synchronous or Newtonian gauge. Obtaining, for the Newtonian gauge,

$$\delta' + 3\frac{1}{\tau}\left(c_s^2 - w\right)\delta = -\left(1+w\right)\theta, \tag{2.39}$$

$$\theta' + \left[\frac{1}{\tau}(1-3w) + \frac{w'}{1+w}\right]\theta = -k^2\left(\frac{c_s^2}{1+w}\delta + \frac{20C}{15+4R_\nu}\right); \tag{2.40}$$

and for the synchronous gauge

$$\delta' + 3\frac{1}{\tau}\left(c_s^2 - w\right)\delta = -\left(1+w\right)\left(\theta + \frac{2Ck^2\tau}{2}\right), \tag{2.41}$$

$$\theta' + \left[\frac{1}{\tau}(1-3w) + \frac{w'}{1+w}\right]\theta = k^2\frac{c_s^2}{1+w}\delta. \tag{2.42}$$

These equations can be simplified by considering that during the radiation epoch, the UDM fluid behaves exactly as CDM, and we can approximate $w = w' = c_s^2 = 0$, obtaining the CDM initial conditions.

2.2 The Generalised Chaplygin Gas

In chapter 3 we shall describe in detail the numerical implementation of the UDM model with a fast transition. This is the first time that linear structure formation is computed in detail for this particular model. As such, there are no previous results with which to compare our results. In order to test if our numerical implementation is well done, we decided to also implement the more widely studied Generalised Chaplygin Gas (GCG). Even though the behaviours of the two models are quite different, we can compare the power spectra of the GCG computed with our implementation with published GCG results, and use it as an indirect test of possible numerical problems in our implementations.

We will now briefly introduce the GCG model. The GCG is defined as a perfect fluid with the following equation of state [33, 44]

$$p_{cg} = -\frac{A}{\rho_{cg}^{\alpha}}, \tag{2.43}$$

where α (ranging from 0 to 1) allows to generalise the standard Chaplygin Gas model, which corresponds to the case $\alpha = 0$. From the continuity equation (1.24) we get an equation for the evolution of the energy density of the GCG

$$\rho_{cg}(a) = \left[A + a^{-3(1+\alpha)}\left(\rho_{cg(0)}^{1+\alpha} - A\right)\right]^{\frac{1}{1+\alpha}} \tag{2.44}$$

This equation can be rewritten as

$$\rho_{cg}(a) = \rho_{cg(0)}\left[\bar{A} + (1-\bar{A})a^{-3(1+\alpha)}\right]^{\frac{1}{1+\alpha}}. \tag{2.45}$$

We can see that just like the UDM with fast transition, the GCG has a period ($a \ll 1$) where it behaves like DM with $\rho_{cg} \propto \left(1-\bar{A}\right)^{\frac{1}{1+\alpha}} a^{-3}$ and a period ($a \gg 1$) where it behaves like DE with $\rho_{cg} \propto \bar{A}^{\frac{1}{1+\alpha}}$ (in particular, it can behave like a cosmological constant).

This behaviour is of course expressed also in the evolution of the equation of state, that for the GCG is

$$w_{cg} = \frac{p}{\rho} = -\frac{A}{\rho_{cg}^{1+\alpha}}. \tag{2.46}$$

and in the evolution of the speed of sound

$$c_{s,cg}^2 = \frac{dp}{d\rho} = -\alpha w_{cg}. \tag{2.47}$$

The same differential equations (1.79), (1.80), (1.85), (1.86) describe the evolutions of the perturbations for this fluid.

2.3 Non-linearity (Backreaction)

In this thesis we focus on linear perturbations and we will test the model using data on linear scales (see discussion in chapter 4). However, we are aware that in single fluid models the existence of non-linearities also has an impact on the large scale evolution of the universe. This effect, known as the back reaction of small scale clustering onto large scales was studied in [33] for the case of the GCG model. This effect arises because as regions of the single fluid collapse and decouple from the evolution, the energy density available to continuing the evolution decreases. This has an impact on both the background dynamics of the universe and on the linear clustering. It was shown in [33] that, by altering the background evolution, this backreaction may reconcile the original Chaplygin gas model ($\alpha = 1$) with Supernova data, and, that by altering the oscillations in the linear power spectrum, may reconcile the GCG model with large-scale structure data.

We implemented backreaction in CLASS for both the GCG model and our fast transition UDM model. However, a detailed study of this effect is beyond the goals of this thesis and we do not consider it when testing the UDM model with data in our central analysis. We leave the backreaction results and discussion for the appendix.

We followed the idea presented in [33, 44], and considered that the UDM fluid is essentially divided into collapsed regions (+) where the energy density is much larger than the average energy density of the fluid, and underdense regions (−), that occupy most of the volume of the universe, where the energy density is smaller than the average.

The average fraction of the total UDM energy E that belongs to collapsed objects (with total energy E_+) in a comoving region of the universe of comoving volume V is

$$\epsilon = \frac{E_+}{E}. \tag{2.48}$$

The contribution of the collapsed regions to the average energy density of the universe is

$$\rho_+ = \frac{E_+}{V} = \epsilon\rho, \tag{2.49}$$

and the contribution from the underdense regions is

$$\rho_- = \frac{E_-}{V} = \frac{E - E_+}{V} = (1-\epsilon)\rho. \tag{2.50}$$

The contributions to the pressure come only from the underdense regions, which implies that the effective equation of state of the fluid is

$$w = \frac{p_-}{\rho} = \frac{\rho_-}{\rho}\frac{p_-}{\rho_-} = (1-\epsilon)w_-. \tag{2.51}$$

The fact that the underdense regions determine the background evolution, but do not contain all the energy of the fluid, imposes this new effective w and constitutes a backreaction of the collapsed regions on the background evolution.

To completely describe the effect, we need to define the evolution of the fraction ϵ. We follow [33] and consider the simple model where E_+ remains fixed. On the other hand, the total energy evolves as $E \propto \rho a^{-3}$, and so the evolution of ϵ is given by

$$\epsilon = \frac{\epsilon_0 \rho_0}{\rho a^3}, \tag{2.52}$$

where we introduced the parameter $\epsilon_0 = \epsilon(a = 1)$.

With ϵ_0 we can now calculate ρ_+, ρ_- as well as the effective equation of state and the speed of sound associated with the fluid ρ_-. With this, we have all the ingredients needed to compute the perturbations for this model including the backreaction. We use the differential Eqs. (1.79), (1.80), (1.85), (1.86), separately for both regions + and −. In particular, for the collapsed regions we use $w_+ = 0$ and $c^2_{s,+} = 0$. And for the underdense regions, we use w and c_s calculated for the GCG, Eqs.(2.46),(2.47), but now with the energy density ρ_-.

Chapter 3

Cosmic Linear Anisotropy Solving System (CLASS)

Now that we introduced the UDM and the GCG models, we need a code to allow us to solve the full set of differential equations for the evolution of perturbations in these models. This will allow us to calculate the quantities needed to test the models against observables.

In chapter 1, we described the system of perturbed Einstein equations in the Newtonian and synchronous gauges for the perturbed energy-momentum tensor of a cosmological fluid. That system of equations governs the evolution of metric perturbations and contains the fluid equations valid for the matter species. In particular, this system of equations describes linear structure formation in the UDM and GCG models. For radiative cosmological species, such as the CMB photons, the fluid description is not valid and Boltzmann equations must be used [45]. There are a few public cosmological perturbations codes available that implement the full set of Einstein-Boltzmann equations. These are usually known in cosmology as Boltzmann codes. Our approach is to implement our models in CLASS [46] by modifying the Einstein and fluid equations. The UDM and GCG models do not introduce additional couplings or modifications in the radiation sector and do not require modifications of the Boltzmann description in the code.

The main reason to choose CLASS over other Boltzmann codes such as CAMB [47], CMBFAST [48] or CMBEASY [49] is because CLASS is a new accurate code designed to offer a more user-friendly and flexible coding environment to cosmologists. CLASS is very well structured, can be modified in a consistent way, offers a rigorous way to control the accuracy of output quantities, is faster than others codes, and is written in C.

A great part of our work relied on the implementation of the UDM model in CLASS to test the model with observational data of the inhomogeneous universe. But, as said before, since this implementation is not trivial, we decided to implement in a separate code a GCG model that had been already studied at perturbation level [44] and compare the results.

Compiling CLASS requires no specific version of the compiler, no special package or library [46]. The code is executed with a maximum of two input files, e.g.
./class explanatory.ini chi2pl1.pre
The file with a .ini extension is the cosmological parameters input file, and the one with a .pre extension is the precision file. Both files are optional: all parameters are set to default values corresponding to the "most usual choices", and are eventually replaced by the parameters passed in the two input files. For

instance, if one is happy with default accuracy settings, it is enough to run with ./class explanatory.ini. Input files do not necessarily contain a line for each parameter, since many of them can be left to default values. Fig. 3.1 shows part of a modified input file.

```
# List of input/precision parameters actually read
# (all other parameters set to default values)
# Obtained with CLASS v2.4.1 (for developpers: svn version 6142M)
#
# This file can be used as the input file of another run
#
h = 0.69508
T_cmb = 2.7255
omega_b = 0.022032
N_ur = 3.046
Omega_cdm = 0.00000001
Omega_dcdmdr = 0.0
Gamma_dcdm = 0.0
N_ncdm = 0
Omega_k = 0.
Omega_Lambda = 0
Omega_fld = 0
Omega_scf = 0

alpha_udm = 0
a_transition_udm=0.15
beta_udm=0
Omega_lambda_udm=0.72
use_backreaction_udm = no
epsilon_init_udm= 0.4
```

Figure 3.1: Part of the input file used to run the UDM model (teste.ini) already with the implementation of the new quantities related to the UDM model.

The code is divided in several modules: one module for the background evolution, one for the thermodynamics, another one for the perturbations, etc. There are no duplicate equations and a given physical assumption should be formulated only in a single place. For an illustrative representation of the flexibility of CLASS and how it works let us take an example where we integrate over time a set of background and perturbation equations. For the background equations, CLASS uses an adaptive Runge-Kutta integrator. Such integrators need to be called several times over small time steps. The edge of these time steps defines the discrete values of time at which background quantities will be tabulated and stored, in view of being interpolated in other modules. CLASS infers the step sizes automatically from the rate at which background equations change. So, in a non-standard cosmological model where something special would happen at a given time, the step size would automatically decrease around that time. The same occurs with the perturbation equations when we use the same Runge-Kutta integrator, which is only an option (the default integrator for perturbations, called ndf15, is described in [50]).

To show how the implementation was made we will follow the flexibility and structure of CLASS and present the implementation for each module separately. Since the code is quite big, we will only include the most important modules and we will not explain in detail those modules, but rather show the implementation added in each module and briefly explain its job. Also, it is important to note that the implementation of these new fluids was made in a way that allows us to "activate" or not this new components. If we do not define any parameters of the new fluid, CLASS will set those fluids to zero and will reproduce the ΛCDM model.

3.1 Input module

The input.c is basically where the code reads the .ini file and goes through a check list of conditions needed in order to run the code properly.

We start the implementation by defining a flag for the input parameter *Omega_lambda_udm* that will activate in case CLASS finds the parameter defined as shown in Fig. 3.2. That flag will tell the code that we have this fluid in the universe.

```
/** UDM begins **/
class_call(parser_read_double(pfc,"Omega_Lambda",&param1,&flag1,errmsg),
           errmsg,
           errmsg);
class_call(parser_read_double(pfc,"Omega_fld",&param2,&flag2,errmsg),
           errmsg,
           errmsg);
class_call(parser_read_double(pfc,"Omega_scf",&param3,&flag3,errmsg),
           errmsg,
           errmsg);
class_call(parser_read_double(pfc,"Omega_lambda_udm",&param4,&flag4,errmsg),
           errmsg,
           errmsg);
```

Figure 3.2: Part of the code were we define the new flag for the new fluid.

We included the new fluid in some of the conditions of the check list and added new conditions to the list. As an example, Fig. 3.3 shows the inclusion of the UDM fluid in an already existing condition to enable to run a model with a DE scalar field.

```
/** - Test that the user have not specified Omega_scf = -1 but left either
    Omega_lambda or Omega_fld unspecified:*/
class_test(((flag1 == _FALSE_) || (flag2 == _FALSE_) || (flag4 == _FALSE_)) && ((flag3 == _TRUE_) && (param3 < 0.)),
           errmsg,
           "It looks like you want to fulfil the closure relation sum Omega = 1 using the scalar field, so you have to specify both Omega_lambda, Omega_fld and Omega_lambda_udm in the .ini file"); /** UDM
           begins */ /* This test includes udm now */ /** UDM ends **/
```

Figure 3.3: An example of a check where the UDM is now included.

After that we calculate the value of Ω_{udm} today. As we saw in section 2.1, the UDM model is not parametrised by Ω_{udm} today. We compute this value by subtracting the sum of all other density components of the cosmological fluid to 1, as shown in Fig. 3.4. In case this does not fill the universe completely, CLASS completes the sum by adding small amounts of fluids that were not used such as Ω_Λ, Ω_{fld}, Ω_{scf} and Ω_{udm} (where fld stands for fluid and scf stands for scalar field). This is the general procedure used by CLASS to always set the total density to one. We include Ω_{udm} as an available choice for CLASS users by including the lines of code shown in Fig. 3.5.

```
/** UDM begins */
  if (flag4 == _TRUE_){
    pba->Omega0_udm = 1. - pba->Omega0_k - Omega_tot; /*Omega0_udm is Omega_lambda + Omega_cdm, so it has to be defined in this way */
    Omega_tot += pba->Omega0_udm;
/** UDM ends */
  }
```

Figure 3.4: Calculating $\Omega_{0,udm}$.

```
}/** UDM begins **/
else if (flag4 == _FALSE_) {
  pba->Omega0_udm = 1. - pba->Omega0_k - Omega_tot;
  if (input_verbose > 0) printf(" -> matched budget equations by adjusting Omega_udm = %e\n",pba->Omega0_udm);
} /** UDM ends **/
```

Figure 3.5: Filling the universe in case the sum of all densities does not equal unity.

Another important modification is the inclusion of the lines of code shown in Fig. 3.6, that allows CLASS to read the values of the UDM parameters and backreaction parameters defined in the input file.

```
/** UDM begins **/
if (pba->Omega0_udm != 0.) {
  class_read_double("beta_udm",pba->beta_udm);
  class_read_double("alpha_udm",pba->alpha_udm);
  class_read_double("Omega_lambda_udm",pba->Omega_lambda_udm);
  class_read_double("a_transition_udm",pba->a_transition_udm);

  class_call(parser_read_string(pfc,
                                "use_backreaction_udm",
                                &string1,
                                &flag1,
                                errmsg),
             errmsg,
             errmsg);

  if (flag1 == _TRUE_){
    if((strstr(string1,"y") != NULL) || (strstr(string1,"Y") != NULL)){
      pba->use_backreaction_udm = _TRUE_;
      class_read_double("epsilon_init_udm",pba->epsilon_init_udm);
    }
    else {
      pba->use_backreaction_udm = _FALSE_;
    }
  }
}
/** UDM ends **/
```

Figure 3.6: Reading the values of the UDM and backreaction parameters from the input file.

```
/** UDM begins **/
  pba->Omega0_udm = 0.;
  pba->alpha_udm=0.;
  pba->beta_udm=552.;
  pba->Omega_lambda_udm=0.;
  pba->a_transition_udm=0.17;
  pba->use_backreaction_udm = _FALSE_;
  pba->epsilon_init_udm=0.;
/** UDM ends **/
```

Figure 3.7: The default value of each new parameter is defined in case they are not expressed in the input file.

Similar to what is done for all other components, we also define default values for the new parameters

in case the user does not define them in the input file. In the example shown in Fig. 3.7 we set the default value of Ω_{udm} to zero, meaning that the code will run ΛCDM if we do not assign any value for this parameter in the input file.

3.2 Background module

At background level, we introduced the new fluid in CLASS as a new component that can enter the Hubble function. This modification involves the introduction of new quantities in the background structure (background.h), and in the background module (background.c).

The background structure, as all structures of other modules, is where we define the quantities that we need to store and pass from one module to another, including flags, variables and vectors.

We start by calculating the value of Ω_{udm} at the time of the transition. We define it as $\rho_t / \rho_{crit,0}$, using the critical density of today as normalisation. Then we define how the energy density of the UDM fluid evolves Eq.(2.6) as well as the other important quantities related to the fluid, like the equation of state Eq.(2.3) and the speed of sound Eq.(2.4). Also, we define a matter-like part of the UDM fluid, $\rho_{m,udm}$, as

$$\rho_{m,udm} = \rho_t \left(\frac{a_t}{a}\right)^3 . \tag{3.1}$$

This means that the UDM fluid was purely matter-like behaviour before the transition, and after the transition this evolving density will be considered as a matter component of the UDM. The remaining density, $\rho_{udm} - \rho_{m,udm}$, will be considered as the dark energy component of the UDM, $\rho_{DE,udm}$. The computation of all these quantities is shown in Fig. 3.8.

```
/** UDM begins **/
if (pba->has_udm == _TRUE_) {

  pba->a_transition_udm = pba->a_transition_udm / pba->a_today;

  pvecback[pba->index_bg_heavi_udm] = (0.5 + 1./_PI_ * atan(pba->beta_udm*(a_rel - pba->a_transition_udm)));

  pvecback[pba->index_bg_dheavi_udm] = (pba->beta_udm / (_PI_ + pow(a_rel - pba->a_transition_udm,2) * _PI_ * pow(pba->beta_udm,2)));

  pvecback[pba->index_bg_d2heavi_udm] = ( - (2. * (a - pba->a_transition_udm) * _PI_ * pow(pba->beta_udm,3) ) / ( pow(_PI_ + pow(a_rel - pba->a_transition_udm,2) * _PI_ * pow(pba->beta_udm,2),2)) );

  pba->Omega_t_udm =( (1. - pba->Omega0_ncdm_tot - pba->Omega0_dcdmdr - pba->Omega0_g - pba->Omega0_b - pba->Omega0_k - pba->Omega0_ur - pba->Omega0_cdm - (pba->Omega_lambda_udm -
  pba->Omega_lambda_udm*pow(pba->a_transition_udm, 3.*(1. + pba->alpha_udm)))*(0.5 + 1./_PI_ * atan(pba->beta_udm*(1./pba->a_today - pba->a_transition_udm))) )/ ( pow(pba->a_transition_udm,3) +
  (pow(pba->a_transition_udm, 3.*(1. + pba->alpha_udm)) - pow(pba->a_transition_udm,3))*(0.5 + 1./_PI_ * atan(pba->beta_udm*(1./pba->a_today - pba->a_transition_udm))) ) );

  pvecback[pba->index_bg_rho_udm] =( pba->Omega_t_udm * pow(pba->H0,2) * pow(pba->a_transition_udm/a_rel,3) + ( pba->Omega_lambda_udm * pow(pba->H0,2) + ( pba->Omega_t_udm * pow(pba->H0,2) -
  pba->Omega_lambda_udm * pow(pba->H0,2)) * pow(pba->a_transition_udm/a_rel,3*(1+pba->alpha_udm)) - pba->Omega_t_udm * pow(pba->H0,2) * pow(pba->a_transition_udm/a_rel,3)) * pvecback[pba->index_bg_heavi_udm] );

  pvecback[pba->index_bg_rhom_udm] = ( pba->Omega_t_udm * pow(pba->H0,2) * pow(pba->a_transition_udm/a_rel,3));

  pvecback[pba->index_bg_rho_prime_udm] =( (-3.*pow(pba->a_transition_udm,3)*pba->Omega_t_udm*pow(pba->H0,2))/(pow(a_rel,4)) +
  (3.*pow(pba->a_transition_udm,3)*(pow((pba->a_transition_udm/a_rel),3.*pba->alpha_udm)*(1.+pba->alpha_udm)*(pba->Omega_lambda_udm*pow(pba->H0,2) - pba->Omega_t_udm*pow(pba->H0,2)) +
  pba->Omega_t_udm*pow(pba->H0,2) ) * pvecback[pba->index_bg_heavi_udm] )/(pow(a_rel,4)) + (pba->Omega_lambda_udm*pow(pba->H0,2) - (pow(pba->a_transition_udm,3)*pba->Omega_t_udm*pow(pba->H0,2))/pow(a_rel,3) +
  pow((pba->a_transition_udm/a_rel),3.*(1.+pba->alpha_udm)) * (pba->Omega_t_udm*pow(pba->H0,2) - pba->Omega_lambda_udm*pow(pba->H0,2)) ) * pvecback[pba->index_bg_dheavi_udm] );

  pvecback[pba->index_bg_rho_2prime_udm] =( (1./pow(a_rel,5))*(12.*pow(pba->a_transition_udm,3)*pba->Omega_t_udm*pow(pba->H0,2) + 3.*pow(pba->a_transition_udm,3) *
  (-1.*pow((pba->a_transition_udm/a_rel),3.*pba->alpha_udm) * (1.+pba->alpha_udm)*(4.+3.*pba->alpha_udm)*(pba->Omega_lambda_udm*pow(pba->H0,2) -
  pba->Omega_t_udm*pow(pba->H0,2))-4.*pba->Omega_t_udm*pow(pba->H0,2) )*pvecback[pba->index_bg_heavi_udm] + 6.*a_rel*pow(pba->a_transition_udm,3)*(
  pow((pba->a_transition_udm/a_rel),3.*pba->alpha_udm)*(1.+pba->alpha_udm)*(pba->Omega_lambda_udm*pow(pba->H0,2) - pba->Omega_t_udm*pow(pba->H0,2)) + pba->Omega_t_udm*pow(pba->H0,2)) *
  pvecback[pba->index_bg_dheavi_udm] + pow(a_rel,2)*(pow(a_rel,3)*pba->Omega_lambda_udm*pow(pba->H0,2) +
  pow(pba->a_transition_udm,3)*(-1.*pba->Omega_t_udm*pow(pba->H0,2)+pow((pba->a_transition_udm/a_rel),3.*pba->alpha_udm)*(pba->Omega_t_udm*pow(pba->H0,2) - pba->Omega_lambda_udm*pow(pba->H0,2))))*
  pvecback[pba->index_bg_d2heavi_udm] ) );

  pvecback[pba->index_bg_w_udm] =(-a_rel/3. * (pvecback[pba->index_bg_rho_prime_udm]/pvecback[pba->index_bg_rho_udm]) -1.);

  pvecback[pba->index_bg_cs2_udm] =(-a_rel/3. * (pvecback[pba->index_bg_rho_2prime_udm]/pvecback[pba->index_bg_rho_prime_udm]) - 4./3.);
```

Figure 3.8: Part of the code in background.c module where ρ, w and c_s^2 for the UDM model were implemented.

After we defined these background equations we verify whether we want to consider backreaction

or not. In case we do not want to, we add the energy density of the UDM to the total energy density, as well as the pressure. When backreaction is considered, we separate the energy density in a part that belongs to collapse regions and a part that belongs to underdense regions and re-calculate the speed of sound and the equation of state as discussed in section 3.3. After these considerations, we can then proceed to modify the Hubble function, as shown in Figs. 3.9 and 3.10.

```
if (pba->use_backreaction_udm == _FALSE_){
 rho_tot += pvecback[pba->index_bg_rho_udm];
 p_tot += pvecback[pba->index_bg_w_udm] * pvecback[pba->index_bg_rho_udm];
 rho_m += pvecback[pba->index_bg_rhom_udm];
 pba->Omega0_m_udm=( pba->Omega_t_udm * pow(pba->a_transition_udm,3));
}
```

Figure 3.9: Including UDM energy density and pressure in the Hubble function without backreaction.

```
if (pba->use_backreaction_udm == _TRUE_){
 pba->epsilon0_udm = ((pba->epsilon_init_udm * pba->Omega_t_udm * pow(pba->H0,2) * pow(pba->a_transition_udm,3))/(pba->Omega0_udm * pow(pba->H0,2)));
 pvecback[pba->index_bg_epsilon_udm] = ((pba->epsilon0_udm * pba->Omega0_udm * pow(pba->H0,2))/(pvecback[pba->index_bg_rho_udm]*pow(a_rel,3)) );
 pvecback[pba->index_bg_epsilon_prime_udm] = (-(pba->epsilon0_udm * pba->Omega0_udm * pow(pba->H0,2)*(3.*pvecback[pba->index_bg_rho_udm] + a_rel * pvecback[pba->index_bg_rho_prime_udm]
 )/(pow(a_rel,4)*pow(pvecback[pba->index_bg_rho_udm],2))));
 pvecback[pba->index_bg_epsilon_2prime_udm] = (pba->epsilon0_udm * pba->Omega0_udm * pow(pba->H0,2) *
 (12.*pow(pvecback[pba->index_bg_rho_udm],2)+2.*pow(a_rel,2)*pow(pvecback[pba->index_bg_rho_prime_udm],2)+a_rel*pvecback[pba->index_bg_rho_udm]*(6.*pvecback[pba->index_bg_rho_prime_udm]-a_rel*pvecback[pba->in
 dex_bg_rho_2prime_udm]))/(pow(a_rel,5)*pow(pvecback[pba->index_bg_rho_udm],3)));
 pvecback[pba->index_bg_rho_plus_udm] = (pvecback[pba->index_bg_epsilon_udm] * pvecback[pba->index_bg_rho_udm]);
 pvecback[pba->index_bg_rho_minus_udm] = ((1. - pvecback[pba->index_bg_epsilon_udm])*pvecback[pba->index_bg_rho_udm]);

 pvecback[pba->index_bg_rho_minus_prime_udm] = (- pvecback[pba->index_bg_rho_udm]*pvecback[pba->index_bg_epsilon_prime_udm] + (1.-pvecback[pba->index_bg_epsilon_udm])*pvecback[pba->index_bg_rho_prime_udm]);

 pvecback[pba->index_bg_rho_minus_2prime_udm] = (-2.*pvecback[pba->index_bg_epsilon_prime_udm]*pvecback[pba->index_bg_rho_prime_udm]-pvecback[pba->index_bg_rho_udm]*pvecback[pba->index_bg_epsilon_2prime_udm]
 + (1.-pvecback[pba->index_bg_epsilon_udm])*pvecback[pba->index_bg_rho_2prime_udm]);

 pvecback[pba->index_bg_w_minus_udm] = (-a_rel/3. * (pvecback[pba->index_bg_rho_minus_prime_udm]/pvecback[pba->index_bg_rho_minus_udm]) -1.);
 pvecback[pba->index_bg_w_udm] =(pvecback[pba->index_bg_w_minus_udm]*(1. - pvecback[pba->index_bg_epsilon_udm]));
 pvecback[pba->index_bg_cs2_minus_udm] = (-a_rel/3. * (pvecback[pba->index_bg_rho_minus_2prime_udm]/pvecback[pba->index_bg_rho_minus_prime_udm]) - 4./3.);

 rho_tot += pvecback[pba->index_bg_rho_udm];
 //rho_tot += pvecback[pba->index_bg_rho_minus_udm];
 p_tot += pvecback[pba->index_bg_w_udm] * pvecback[pba->index_bg_rho_udm];
 rho_m += pvecback[pba->index_bg_rhom_udm];
 }
}
/** UDM ends **/
```

Figure 3.10: Including UDM energy density and pressure in the Hubble function considering the backreaction effect.

Upon running, the code outputs some information on-screen, that now has UDM-related informations, and an output data file showing the evolution of various background quantities, such as the Hubble function and various cosmological distances and densities, against redshift. Besides UDM-related quantities, we have also included the scale factor in the output file, which is a convenient time variable, related to the redshift as $a = \dfrac{1}{z+1}$. The various steps needed to modify the outputs are shown in Figs. 3.11, 3.12 and 3.13.

```
/** UDM begins **/
if (pba->has_udm == _TRUE_){
  printf("    Unified Dark Matter details:\n");
  printf("     -> a today = %f\n", pba->a_today);
  printf("     -> a of transition = %f\n", pba->a_transition_udm);
  printf("     -> Omega0_m_UDM = %g , %f\n", pvecback[pba->index_bg_Omega_m], pvecback[pba->index_bg_rho_crit]/pow(pba->H0,2) );
  printf("     -> Omega at transition = %f\n",pba->Omega_t_udm);
  printf("     -> Omega Lambda for UDM = %f\n",pba->Omega_lambda_udm);
  printf("     -> Omega_UDM = %g, wished %g\n",
         pvecback[pba->index_bg_rho_udm]/pvecback[pba->index_bg_rho_crit], pba->Omega0_udm);
  printf("     -> epsilon0 = %g, rho_init_udm %g\n",
         pba->epsilon0_udm, pba->Omega0_udm * pow(pba->H0,2));
}
/** UDM ends **/
```

Figure 3.11: Including on-screen information related to the UDM.

```
class_store_columntitle(titles,"(.)rho_udm",pba->has_udm); /** UDM begins **/
class_store_columntitle(titles,"(.)rhom_udm",pba->has_udm);
class_store_columntitle(titles,"w_udm",pba->has_udm);
class_store_columntitle(titles,"cs2_udm",pba->has_udm);
class_store_columntitle(titles,"epsilon",pba->has_udm && (pba->use_backreaction_udm == _TRUE_));
class_store_columntitle(titles,"w_minus",pba->has_udm && (pba->use_backreaction_udm == _TRUE_));
class_store_columntitle(titles,"cs2_minus",pba->has_udm && (pba->use_backreaction_udm == _TRUE_));  /** UDM ends **/
```

Figure 3.12: Adding new columns and their titles in the background data file.

```
class_store_double(dataptr,pvecback[pba->index_bg_rho_udm],pba->has_udm,storeidx); /** UDM begins **/
class_store_double(dataptr,pvecback[pba->index_bg_rhom_udm],pba->has_udm,storeidx);
class_store_double(dataptr,pvecback[pba->index_bg_w_udm],pba->has_udm,storeidx);
class_store_double(dataptr,pvecback[pba->index_bg_cs2_udm],pba->has_udm,storeidx);
class_store_double(dataptr,pvecback[pba->index_bg_epsilon_udm],pba->has_udm && (pba->use_backreaction_udm == _TRUE_),storeidx);
class_store_double(dataptr,pvecback[pba->index_bg_w_minus_udm],pba->has_udm && (pba->use_backreaction_udm == _TRUE_),storeidx);
class_store_double(dataptr,pvecback[pba->index_bg_cs2_minus_udm],pba->has_udm && (pba->use_backreaction_udm == _TRUE_),storeidx); /** UDM ends **/
```

Figure 3.13: Filling the UDM-related columns.

3.2.1 Results

The implementation of the UDM model at background level already allows us to study some of its properties.

Fig. 3.14 shows the evolution of the densities of the various fluids present in this cosmology. We can notice that the density of radiation decreases faster than the density of matter or the UDM, just like in ΛCDM, and that the UDM decreases first with the same rate as the baryons but later gradually deviates (when the transition takes place) and approaches the critical density. It is also important to note, as mentioned in section 2.1, that in this example $a_t = 0.01$, but the scale factor at which the UDM fluid is dominated by the DE-like density ($\rho_{DE,udm} = \rho_{udm} - \rho_{m,udm}$) is $a_* \sim 0.714$.

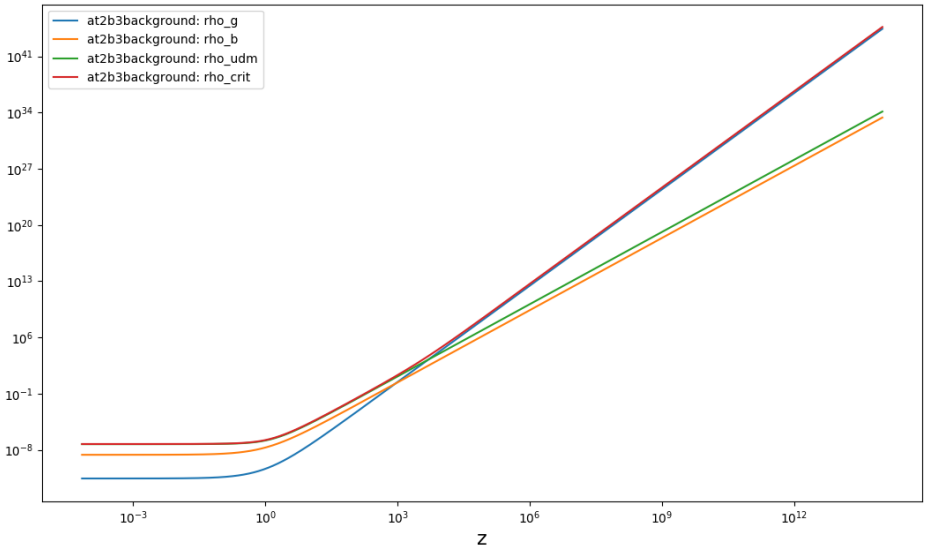

Figure 3.14: Plot of the evolution throughout time *(redshift)* of the energy densities of the various components present in this cosmological model. The UDM fluid is characterised by $a_t = 0.01$, $\beta = 5{\times}10^4$ and $\Omega_{\Lambda udm} = 0.7$. The components are radiation (*rho_g*, blue line), baryons (*rho_b*, orange) and UDM (*rho_udm*, green). The evolution of the critical density is also shown (*rho_crit*,red).

By adding the c_s^2 and w evolution to the output data file, we can make comparisons with the results of [41], as shown in Figs. 3.15 and 3.16. In both cases, there is a perfect match.

In Fig. 3.16 notice that the evolution of $\rho(a)/\rho_\Lambda$ is a monotonic decreasing function and can be used as a time variable. In this model, the transition is at $a_t \sim 0.2$ and the value $\rho/\rho_\Lambda = 50$ corresponds to $\rho = \rho_t$, showing that the peak in the sound speed occurs at the transition $a = a_t$. In our results, shown as function of redshift, the peak occurs at $z_t \sim 4$, or $a_t \sim 0.2$ and the two results match perfectly.

By adding the c_s^2 and w evolution to the output data file, we can make comparisons with the results of [41], as shown in Figs. 3.15 and 3.16. In both cases, there is a perfect match.

In Fig. 3.16 notice that the evolution of $\rho(a)/\rho_\Lambda$ is a monotonic decreasing function and can be used as a time variable. In this model, the transition is at $a_t \sim 0.2$ and the value $\rho/\rho_\Lambda = 50$ corresponds to $\rho = \rho_t$, showing that the peak in the sound speed occurs at the transition $a = a_t$. In our results, shown as function of redshift, the peak occurs at $z_t \sim 4$, or $a_t \sim 0.2$ and the two results match perfectly.

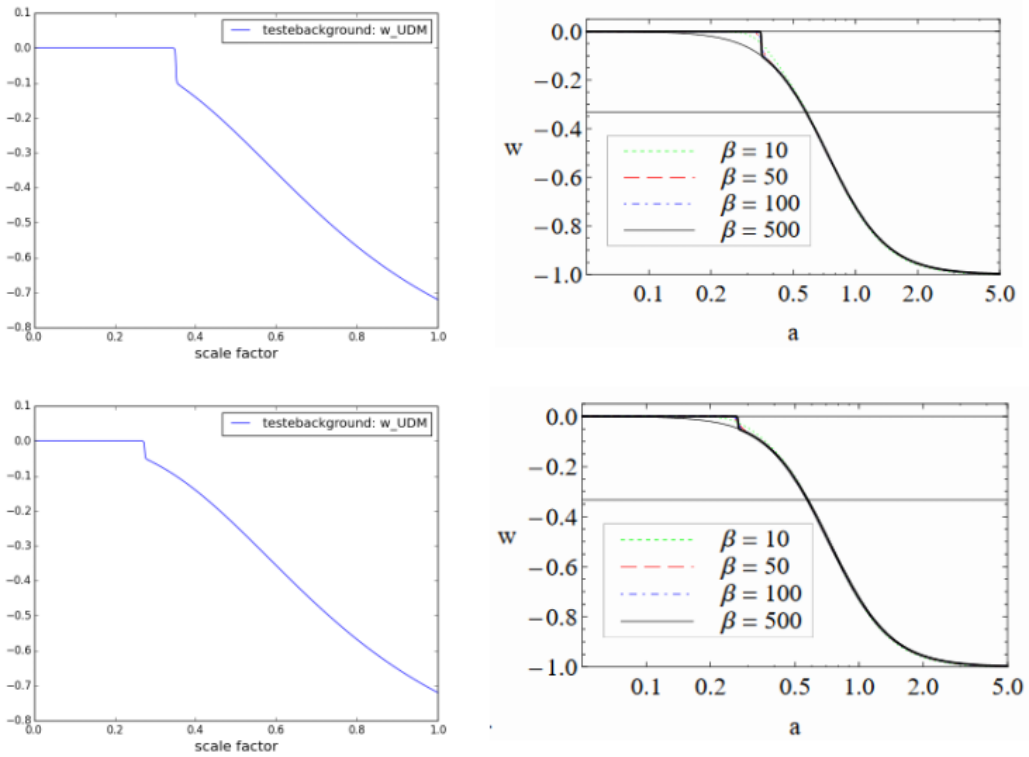

Figure 3.15: Comparison of the evolution of the equation of state w obtained with our CLASS implementation (*left panel*) with the results of [41] (*right panel*).

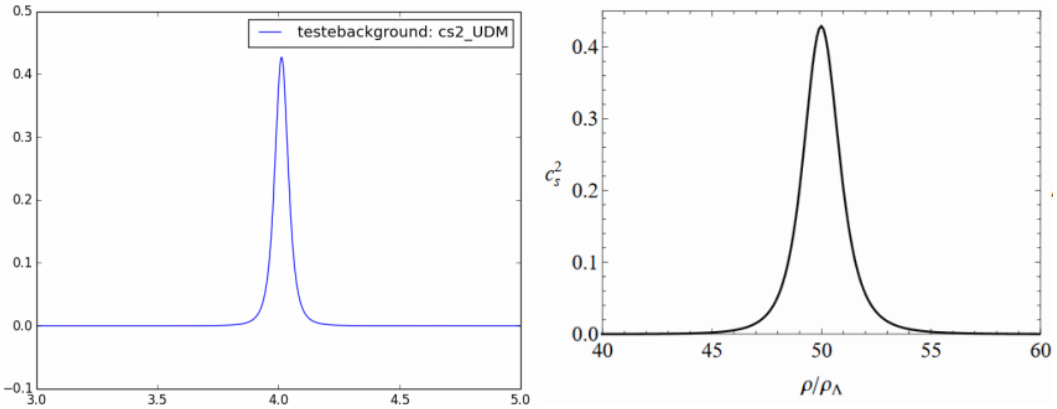

Figure 3.16: Comparison of the plot obtained with the output data file of the background module *(left)* with the one presented in Ref. [41] *(right)* of the evolution of the c_s^2. Right panel uses the density as a time variable, since its evolution is monotonic. $\rho/\rho_\Lambda = 50$ corresponds to $\rho = \rho_t$ showing that the peak occurs at the transition $a = a_t$. The transition occurs at $a_t \simeq 0.2 \Leftrightarrow z_t \simeq 4$, and the 2 panels match perfectly.

```
class_test(pba->cs2_udm_peak > 1.,
           pba->error_message,
           "cs2_udm is %e at some point and bigger than 1", pba->cs2_udm_peak);
```

Figure 3.17: Implementation of a test to forbid sound speeds greater than one.

It is also important to note that after the transition the sound speed does not actually go to zero but to values very close to it. This remaining sound speed, even if very small, could have a large influence on the evolution of perturbations. We will address this issue in Appendix B.

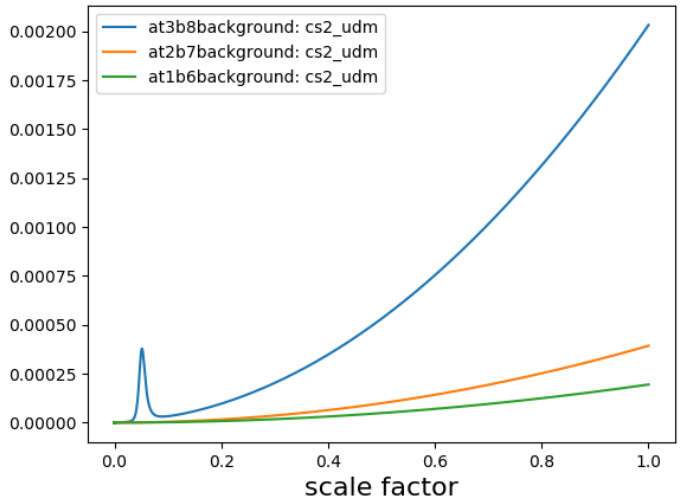

Figure 3.18: Evolution of the speed of sound for the models: ($a_t = 0.05$, $\beta = 100$ and $\Omega_{\Lambda udm} = 0.7$; *blue*), ($a_t = 0.01$, $\beta = 500$ and $\Omega_{\Lambda udm} = 0.7$; *orange*), ($a_t = 0.001$, $\beta = 1000$ and $\Omega_{\Lambda udm} = 0.7$; *green*). In these cases, the sound speed does not go to zero as the universe evolves.

Fig. 3.18 shows the evolution of the speed of sound for three models that produce sound speed peaks of low amplitude at the transition. In those cases the speed of sound does not drop to zero after the transition but increases again. This is a feature of the Heaviside approximation and it is most proemient in models with low amplitude peaks. Other choices of Heaviside approximations are discussed in Appendix B.

3.3 Perturbation module

In the perturbation module, as in every module, we add the UDM-related variables in the perturbation header (perturbation.h). These are δ_{udm} and θ_{udm} or $\delta_{+,udm}$,$\delta_{-,udm}$, $\theta_{+,udm}$, $\theta_{-,udm}$ in the case of backreation. In the file perturbation.c we check the flags that tell us if we want to consider perturbations in the UDM fluid and backreaction. According to that, we add the evolution of the relevant perturbations for the UDM fluid in the output file of perturbations as shown in Fig. 3.19. Those quantities are also passed on to the next modules.

Then, we define the initial conditions. In CLASS, the initial conditions for photons are computed from the matter components according to the standard prescription derived in section 3.1. This is the

major reason why we needed to define a matter-like component of the UDM fluid. We add then this component, $\rho_{m,udm}$ to the total ρ_m, which is used to define others quantities that will be used to define the initial condition of the photons. From the initial conditions for the photons we add the initial conditions for the UDM fluid with and without backreactions using the equations defined in section 3.1. Fig. 3.20 shows the inclusion of these conditions for the case of the synchronous gauge.

```
/** UDM begins **/
class_store_columntitle(ppt->scalar_titles,"delta_udm",pba->has_udm && (pba->use_backreaction_udm == _FALSE_));
class_store_columntitle(ppt->scalar_titles,"theta_udm",pba->has_udm && (pba->use_backreaction_udm == _FALSE_));
class_store_columntitle(ppt->scalar_titles,"delta_plus_udm",pba->has_udm && (pba->use_backreaction_udm == _TRUE_));
class_store_columntitle(ppt->scalar_titles,"delta_minus_udm",pba->has_udm && (pba->use_backreaction_udm == _TRUE_));
class_store_columntitle(ppt->scalar_titles,"theta_plus_udm",pba->has_udm && (pba->use_backreaction_udm == _TRUE_));
class_store_columntitle(ppt->scalar_titles,"theta_minus_udm",pba->has_udm && (pba->use_backreaction_udm == _TRUE_));
/** UDM ends **/
```

Figure 3.19: Part of the code where new column titles for UDM perturbations are added.

```
/** UDM begins **/
if (pba->has_udm == _TRUE_ && pba->use_backreaction_udm == _FALSE_) {
  ppw->pv->y[ppw->pv->index_pt_delta_udm] = 3./4.*ppw->pv->y[ppw->pv->index_pt_delta_g]; /* UDM density */
  ppw->pv->y[ppw->pv->index_pt_theta_udm] = 0.;
}
if (pba->has_udm == _TRUE_ && pba->use_backreaction_udm == _TRUE_) {
  ppw->pv->y[ppw->pv->index_pt_delta_plus_udm] = 3./4.*ppw->pv->y[ppw->pv->index_pt_delta_g]; /* UDM density */
  ppw->pv->y[ppw->pv->index_pt_delta_minus_udm] = 3./4.*ppw->pv->y[ppw->pv->index_pt_delta_g]; /* UDM density */
  ppw->pv->y[ppw->pv->index_pt_theta_plus_udm] = 0.;
  ppw->pv->y[ppw->pv->index_pt_theta_minus_udm] = 0.;
}
/** UDM ends **/
```

Figure 3.20: Part of the code where we define the initial conditions for the UDM fluid in the synchronous gauge.

```
  /** UDM begins **/
if (pba->has_udm == _TRUE_ && pba->use_backreaction_udm == _FALSE_){
  delta_udm = ppw->pv->y[ppw->pv->index_pt_delta_udm];
  theta_udm = ppw->pv->y[ppw->pv->index_pt_theta_udm];
}
else if (pba->has_udm == _TRUE_ && pba->use_backreaction_udm == _TRUE_){
  delta_udm = ppw->pv->y[ppw->pv->index_pt_delta_plus_udm];
  delta_udm += ppw->pv->y[ppw->pv->index_pt_delta_minus_udm];
  theta_udm = ppw->pv->y[ppw->pv->index_pt_theta_plus_udm];
  theta_udm += ppw->pv->y[ppw->pv->index_pt_theta_minus_udm];
}
else
  delta_udm=0.;
  /** UDM ends **/

// note: if there are no neutrinos, fracnu, delta_ur and theta_ur below will consistently be zero.

delta_tot =
(fracg*ppw->pv->y[ppw->pv->index_pt_delta_g]+fracnu*delta_ur+rho_m_over_rho_r*(fracb*ppw->pv->y[ppw->pv->index_pt_delta_b]+fraccdm*delta_cdm+frac_m_udm*delta_
udm))/(1.+rho_m_over_rho_r);

velocity_tot = ((4./3.)*(fracg*ppw->pv->y[ppw->pv->index_pt_theta_g]+fracnu*theta_ur) +
rho_m_over_rho_r*(fracb*ppw->pv->y[ppw->pv->index_pt_theta_b]+frac_m_udm*theta_udm))/(1.+rho_m_over_rho_r);

alpha = (eta + 3./2.*a_prime_over_a*a_prime_over_a/k/k/s2_squared*(delta_tot + 3.*a_prime_over_a/k/k*velocity_tot))/a_prime_over_a;
```

Figure 3.21: Part of the code where we include the UDM fluid in the gauge transformation variables.

To have the possibility to compute UDM perturbations in the Newtonian gauge, we also implemented the gauge transformation equations for the UDM fluid (see Fig. 3.21) and the corresponding initial conditions (see Fig. 3.22).

```
/** UDM begins **/
if (pba->has_udm == _TRUE_ && pba->use_backreaction_udm == _FALSE_) {
  ppw->pv->y[ppw->pv->index_pt_delta_udm] = 3./4. * ppw->pv->y[ppw->pv->index_pt_delta_g];
  ppw->pv->y[ppw->pv->index_pt_theta_udm] = ppw->pv->y[ppw->pv->index_pt_theta_g];
}
if (pba->has_udm == _TRUE_ && pba->use_backreaction_udm == _TRUE_) {
  ppw->pv->y[ppw->pv->index_pt_delta_plus_udm] = 3./4. * ppw->pv->y[ppw->pv->index_pt_delta_g];
  ppw->pv->y[ppw->pv->index_pt_delta_minus_udm] = 3./4. * ppw->pv->y[ppw->pv->index_pt_delta_g];
  ppw->pv->y[ppw->pv->index_pt_theta_plus_udm] = ppw->pv->y[ppw->pv->index_pt_theta_g];
  ppw->pv->y[ppw->pv->index_pt_theta_minus_udm] = ppw->pv->y[ppw->pv->index_pt_theta_g];
}
/** UDM ends **/
```

Figure 3.22: Part of the code where we define the initial conditions for the UDM fluid in the Newtonian gauge.

We arrive now to the point of adding the UDM perturbations to the total perturbed energy momentum tensor. This is shown in Fig. 3.23.

```
/** UDM begins **/
if (pba->has_udm == _TRUE_ && pba->use_backreaction_udm == _FALSE_) {

  a_rel = a / pba->a_today;
  w_udm = ppw->pvecback[pba->index_bg_w_udm];
  cs2_udm = ppw->pvecback[pba->index_bg_cs2_udm];

  ppw->delta_rho += ppw->pvecback[pba->index_bg_rho_udm]*y[ppw->pv->index_pt_delta_udm];
  ppw->rho_plus_p_theta += (1.+w_udm)*ppw->pvecback[pba->index_bg_rho_udm]*y[ppw->pv->index_pt_theta_udm];
  ppw->delta_p += cs2_udm * ppw->pvecback[pba->index_bg_rho_udm]*y[ppw->pv->index_pt_delta_udm];
}
if (pba->has_udm == _TRUE_ && pba->use_backreaction_udm == _TRUE_) {

  a_rel = a / pba->a_today;
  w_minus_udm = ppw->pvecback[pba->index_bg_w_minus_udm];
  cs2_minus_udm = ppw->pvecback[pba->index_bg_cs2_minus_udm];

  ppw->delta_rho += ppw->pvecback[pba->index_bg_rho_plus_udm]*y[ppw->pv->index_pt_delta_plus_udm];
  ppw->delta_rho += ppw->pvecback[pba->index_bg_rho_minus_udm]*y[ppw->pv->index_pt_delta_minus_udm];
  ppw->rho_plus_p_theta += (1.+w_minus_udm)*ppw->pvecback[pba->index_bg_rho_minus_udm]*y[ppw->pv->index_pt_theta_minus_udm];
  ppw->rho_plus_p_theta += ppw->pvecback[pba->index_bg_rho_plus_udm]*y[ppw->pv->index_pt_theta_plus_udm];
  ppw->delta_p += cs2_minus_udm * ppw->pvecback[pba->index_bg_rho_minus_udm]*y[ppw->pv->index_pt_delta_minus_udm];
}
/** UDM ends **/
```

Figure 3.23: Part of the code where we add the contribution of the UDM perturbations to the total perturbed energy-momentum tensor.

We can now include in CLASS the differential equations of the perturbations for the UDM fluid for the two implementations, with or without backreaction. These are Eqs. (1.79), (1.80), (1.85) and (1.86). The new lines of code are shown in Figs. 3.24 and 3.25.

```
/** UDM begins **/
if (pba->has_udm == _TRUE_ && pba->use_backreaction_udm == _FALSE_) {

  a_rel = a / pba->a_today;
  w_udm = ppw->pvecback[pba->index_bg_w_udm];
  cs2_udm = ppw->pvecback[pba->index_bg_cs2_udm];

  /** - ----> UDM density */

  dy[pv->index_pt_delta_udm] =
    -(1.+w_udm)*(y[pv->index_pt_theta_udm]+metric_continuity)
    -3.*(cs2_udm-w_udm)*a_prime_over_a*y[pv->index_pt_delta_udm];

  /** - ----> UDM velocity */

  dy[pv->index_pt_theta_udm] =
    -(1.-3.*cs2_udm)*a_prime_over_a*y[pv->index_pt_theta_udm]
    +cs2_udm*k2/(1.+w_udm)*y[pv->index_pt_delta_udm]
    +metric_euler;

}
```

Figure 3.24: Part of the code where we add the differential perturbative equations for the UDM fluid without backreaction.

```
if (pba->has_udm == _TRUE_ && pba->use_backreaction_udm == _TRUE_) {

  a_rel = a / pba->a_today;
  w_minus_udm = ppw->pvecback[pba->index_bg_w_minus_udm];
  cs2_minus_udm = ppw->pvecback[pba->index_bg_cs2_minus_udm];

  /** - ----> UDM density */

  dy[pv->index_pt_delta_plus_udm] =
    -(1.)*(y[pv->index_pt_theta_plus_udm]+metric_continuity);


  dy[pv->index_pt_delta_minus_udm] =
    -(1.+w_minus_udm)*(y[pv->index_pt_theta_minus_udm]+metric_continuity)
    -3.*(cs2_minus_udm - w_minus_udm)*a_prime_over_a*y[pv->index_pt_delta_minus_udm];

  /** - ----> UDM velocity */

  dy[pv->index_pt_theta_plus_udm] =
    -(1.)*a_prime_over_a*y[pv->index_pt_theta_plus_udm]+metric_euler;

  dy[pv->index_pt_theta_minus_udm] =
    -(1.-3.*cs2_minus_udm)*a_prime_over_a*y[pv->index_pt_theta_minus_udm]
    +cs2_minus_udm*k2/(1.+w_minus_udm)*y[pv->index_pt_delta_minus_udm]
    +metric_euler;

}
//** UDM ENDS **//
```

Figure 3.25: Part of the code where we add the differential perturbative equations for the UDM fluid with backreaction.

The central quantity to study the large scale structure in the universe, and the one we will use to test the models against data, is the matter power spectrum. To test the UDM model, besides computing the evolution of all of its perturbed quantities, we also need to define what its contribution is to the total

matter perturbations δ_m, the basis of the matter power spectrum. We did a similar choice at background level, when we defined a $\rho_{m,udm}$. Here, at perturbative level, we follow the approach suggested in [42] and consider that the matter-like contribution of the UDM density contrast δ_{udm} is the fraction

$$\delta_{m,udm} = \frac{\rho_{udm}\delta_{udm}}{\rho_m}. \tag{3.2}$$

In Fig. 3.26 we can see the lines of code where we add the matter-like contribution of the UDM density contrast to the total δ_m.

```
if (ppt->has_source_delta_m == _TRUE_) {

  /* include baryons and cold dark matter */

  delta_rho_m = ppw->pvecback[pba->index_bg_rho_b]*y[ppw->pv->index_pt_delta_b];
  rho_m = ppw->pvecback[pba->index_bg_rho_b];

  /** UDM begins **/
  if (pba->has_udm == _TRUE_ && pba->use_backreaction_udm == _FALSE_) {
    delta_rho_m += ppw->pvecback[pba->index_bg_rho_udm]*y[ppw->pv->index_pt_delta_udm];
    rho_m += ppw->pvecback[pba->index_bg_rhom_udm];
  }
  if (pba->has_udm == _TRUE_ && pba->use_backreaction_udm == _TRUE_) {
    delta_rho_m += ppw->pvecback[pba->index_bg_rho_plus_udm]*y[ppw->pv->index_pt_delta_plus_udm];
    rho_m += ppw->pvecback[pba->index_bg_rhom_udm];
  }
  /** UDM ends **/

  if (pba->has_cdm == _TRUE_) {
    delta_rho_m += ppw->pvecback[pba->index_bg_rho_cdm]*y[ppw->pv->index_pt_delta_cdm];
    rho_m += ppw->pvecback[pba->index_bg_rho_cdm];
  }
```

Figure 3.26: Part of the code where we add the contribution of the UDM perturbations to the δ_m, used later to calculate the matter power spectrum.

3.3.1 Results: evolution of the density contrast

With the implementation of this module finished we can now compute the evolution of the density contrast and the divergence velocity for the UDM fluid and observe some general behaviours that are characteristic of the model.

As an example, we look at the evolution of δ_{udm} for different values of the parameters of the model and compare it with the evolution of δ_{cdm} in ΛCDM. Figs. 3.27, 3.28 and 3.29 show the evolutions for three different scales.

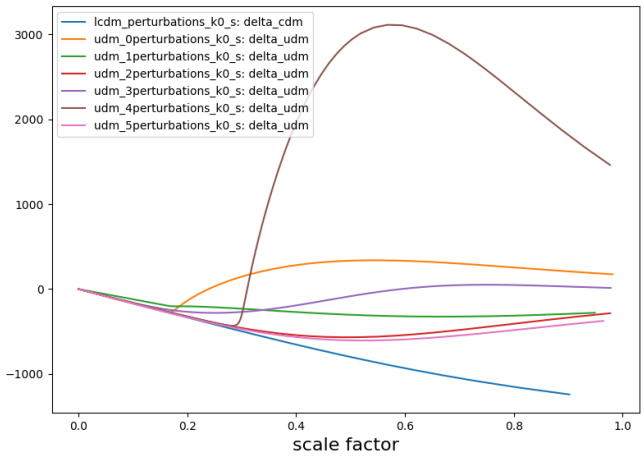

Figure 3.27: Evolution of δ_{udm} for a large scale $k = 0.01$ for different values of the model parameters: orange: $\Omega_{\Lambda udm} = 0.70$, $\beta_{udm} = 200$, $a_{transition} = 0.17$; green: $\Omega_{\Lambda udm} = 0.5$, $\beta_{udm} = 200$, $a_{transition} = 0.17$; red: $\Omega_{\Lambda udm} = 0.70$, $\beta_{udm} = 200$, $a_{transition} = 0.05$; violet: $\Omega_{\Lambda udm} = 0.70$, $\beta_{udm} = 10$, $a_{transition} = 0.11$; brown: $\Omega_{\Lambda udm} = 0.70$, $\beta_{udm} = 100$, $a_{transition} = 0.3$; pink: $\Omega_{\Lambda udm} = 0.70$, $\beta_{udm} = 5 \times 10^5$, $a_{transition} = 0.01$; blue: δ_{cdm} in a flat ΛCDM model with $\Omega_\Lambda = 0.70$.

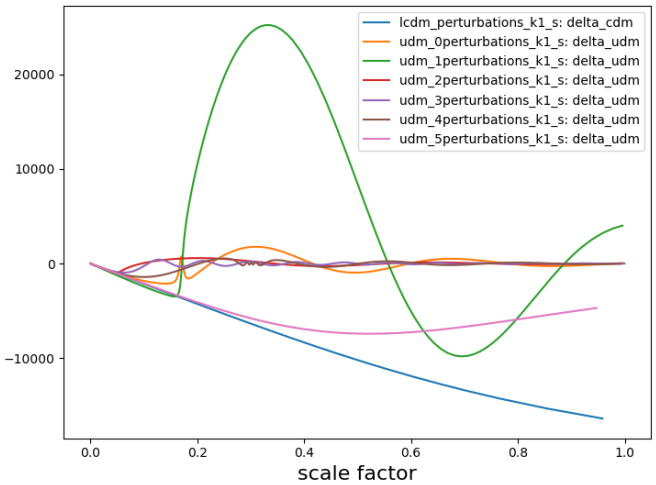

Figure 3.28: Evolution of δ_{udm} for a intermediate scale $k = 0.1$ for different values of the model parameters: orange: $\Omega_{\Lambda udm} = 0.70$, $\beta_{udm} = 200$, $a_{transition} = 0.17$; green: $\Omega_{\Lambda udm} = 0.5$, $\beta_{udm} = 200$, $a_{transition} = 0.17$; red: $\Omega_{\Lambda udm} = 0.70$, $\beta_{udm} = 200$, $a_{transition} = 0.05$; violet: $\Omega_{\Lambda udm} = 0.70$, $\beta_{udm} = 10$, $a_{transition} = 0.11$; brown: $\Omega_{\Lambda udm} = 0.70$, $\beta_{udm} = 100$, $a_{transition} = 0.3$; pink: $\Omega_{\Lambda udm} = 0.70$, $\beta_{udm} = 5 \times 10^5$, $a_{transition} = 0.01$; blue: δ_{cdm} in a flat ΛCDM model with $\Omega_\Lambda = 0.70$.

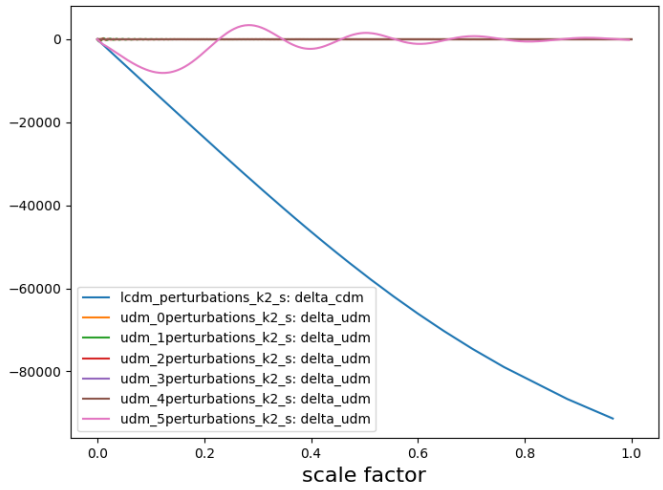

Figure 3.29: Evolution of δ_{udm} for a small scale $k = 10$ for different values of the model parameters: orange: $\Omega_{\Lambda udm} = 0.70$, $\beta_{udm} = 200$, $a_{transition} = 0.17$; green: $\Omega_{\Lambda udm} = 0.5$, $\beta_{udm} = 200$, $a_{transition} = 0.17$; red: $\Omega_{\Lambda udm} = 0.70$, $\beta_{udm} = 200$, $a_{transition} = 0.05$; violet: $\Omega_{\Lambda udm} = 0.70$, $\beta_{udm} = 10$, $a_{transition} = 0.11$; brown: $\Omega_{\Lambda udm} = 0.70$, $\beta_{udm} = 100$, $a_{transition} = 0.3$; pink: $\Omega_{\Lambda udm} = 0.70$, $\beta_{udm} = 5 \times 10^5$, $a_{transition} = 0.01$; blue: δ_{cdm} in a flat ΛCDM model with $\Omega_\Lambda = 0.70$.

We notice that the free parameters of the UDM model have a strong influence on the evolution of the density contrast and also that the same parameter's values give different features for the density contrast on different scales.

In these figures we try to provide a wide range of possibilities for the evolution of the density contrast of UDM in those three scales by choosing several combinations of the parameter values. We try to show the impact of each parameter by fixing two parameters and changing only one. For example, from the orange curve to the green one we only change the parameter $\Omega_{\Lambda udm}$ and we see that at $k = 0.01$ the density contrast for the green curve is always very close to zero while for the orange curve there is a strong deviation from zero. However at $k = 0.1$ the green curve shows a strong oscillatory solution in comparison to the orange one that now tends much faster to zero.

We also try to show the differences between a very early and very fast transition (pink curve) and a slower and late transition (violet and brown curves). In those cases we observe that the pink curve follows closer the δ_{cdm} at $k = 0.01$ in comparison to the other cases, especially comparing with the brown curve where we observe a huge oscillation. At $k = 0.1$ we still see a good behaviour for the pink curve while the other two are already oscillating very close to zero, suggesting that with this choice of parameters the evolution of δ_{udm} strongly decays with the scale. At the small scale $k = 10$ we now see a strong oscillation for the pink curve and the other two cases have $\delta_{udm} = 0$.

We can also compare a case with an early and fast transition (pink curve) with an early and slower transition (red curve). We see that both cases show the same behaviour at $k = 0.01$, but at the others scales, $k = 0.1$ and $k = 10$, the red curve δ_{udm} tends to zero. These comparisons give us an indication that a UDM model with a very fast and early transition could result in a promising matter power spectrum.

We also find a general behaviour in all the cases. At all scales, the UDM fluid follows the ΛCDM model until the transition takes place and after that, we observe an oscillatory solution in all cases. These oscillations are very different from model to model and they are of course related to the sound speed being different from zero. In some cases, the oscillations are very large. This does not happen in our control model, the GCG, where in Fig. 3.30 and in the results of Appendix A we can see that the density contrast also follows ΛCDM until the transition and then starts to oscillate but with small oscillations.

The results for the GCG model, shown in Appendix A, are in perfect agreement with the results published in [44], and successfully validate our implementation procedure in CLASS. However there might be some numerical problems with the UDM implementation, not shown by this test. Numerically, the main difference between the two models is the fact that the speed of sound may be very peaked in the UDM model with fast transition. We need to be sure that the large oscillations found are truly a feature of the model and are not due to some numerical problem related to the numerical integration of a strongly peaked function.

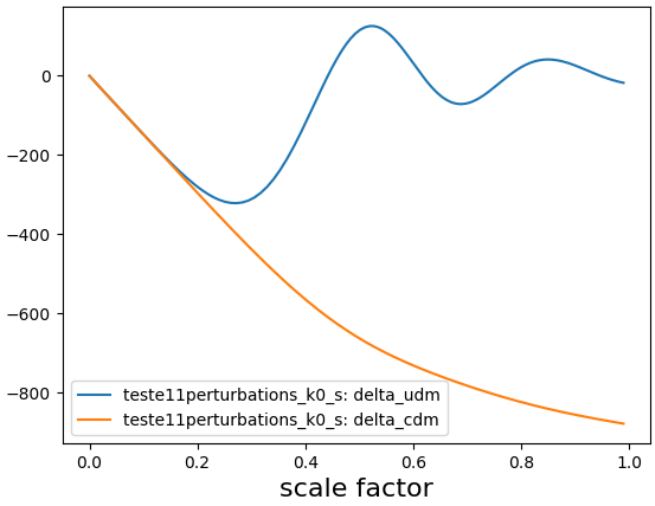

Figure 3.30: Evolution of δ_{GCG} and δ_{cdm} over time for the large scale $k = 0.01$, for *A_chap=0.72* and $\alpha = 0.2$.

We made two different consistency tests to verify our solutions of δ. The first test was to use a Runge-Kutta integrator as an alternative to the ndf15 numerical integrator used by default in CLASS. The second test was to use a different continuous approximation to the Heaviside function, to see the impact on the oscillatory pattern. In both tests we found no significant difference from the previous result, and we consider our UDM results to be reliable for model testing and will use them in the next chapter. As a side product of the second test, we found that some of the Heaviside approximations used (the sigmoid functions) allow for some interesting physical properties. We discuss this point in Appendix B.

3.4 Other modules

After finishing this module we have the implementation almost complete. Now, we only need to modify two more modules: spectra.c and thermodynamics.c. The first one will allow us to calculate the desired matter power spectrum and the angular power spectrum for the CMB. On the second one, we added the UDM fluid to be part of the matter sector of the universe that is passed to the two recombinations codes that are integrated with CLASS (RECFAST and HyRec). It is important to note that further modifications would be needed if we wanted for example to consider models with dark matter annihilation.

3.4.1 Results: power spectra

With these last implementations we obtain all the desired quantities to test our model. In Fig. 3.31 we show the CMB temperature angular power spectrum.
This power spectrum is very sensitive to Ω_Λ, or more precisely to Ω_m due to the flatness condition. Shallower potential wells allow for large oscillations in the baryon-photon plasma and so models with less matter (large Ω_Λ) such as the green model in Fig. 3.31 has larger amplitude than smaller Ω_Λ models (orange).

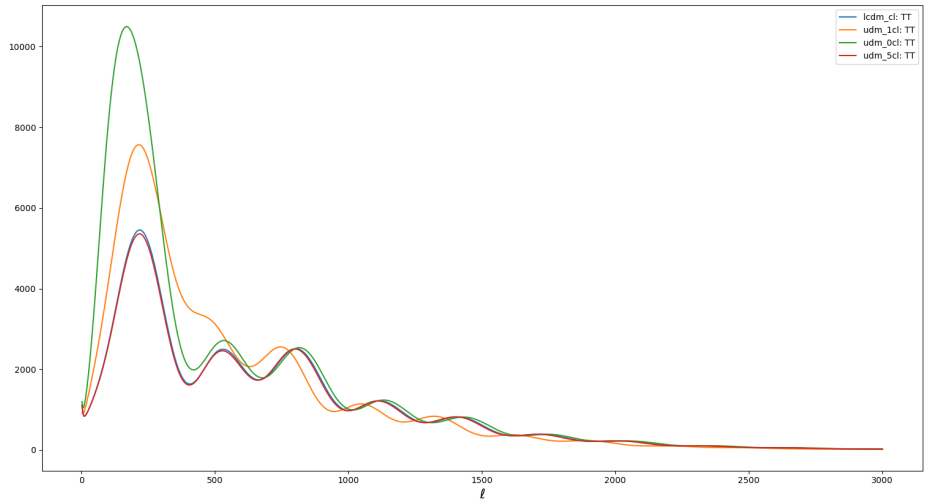

Figure 3.31: Temperature angular power spectrum of the CMB for different values of the model parameters: green: $\Omega_{\Lambda udm} = 0.70$, $\beta_{udm} = 200$, $a_{transition} = 0.17$; orange: $\Omega_{\Lambda udm} = 0.5$, $\beta_{udm} = 200$, $a_{transition} = 0.17$; red: $\Omega_{\Lambda udm} = 0.70$, $\beta_{udm} = 5 \times 10^5$, $a_{transition} = 0.01$; blue: flat ΛCDM model with $\Omega_\Lambda = 0.70$.

The CMB power spectrum is also sensitive to the UDM a_t and β parameters. The model in red, in Fig. 3.31, shows a UDM model with early and fast transition that produces a CMB power spectrum very similar to ΛCDM.

We turn now to the matter power spectrum, the fundamental quantity of structure formation.

In Fig. 3.32 and 3.33 we show the matter power spectra for a wide range of the model parameters, that later will be used to test our model against the Kilo-Degree Survey (KiDS) weak lensing data. In particular, Fig. 3.32 shows models with faster transitions, and Fig. 3.33 shows models with slower transitions. The scales $k = 0.2$ and $k = 0.8$ are also marked in the curves. These scales are close to the two main data points used in the weak lensing analysis in chapter 4, and are then the scales where we probe the UDM power spectra.
The large boxes marked $c_s^2 > 1$ in Figs. 3.32 and 3.33 correspond to combinations of $(a_t\ ,\ \beta)$ parameters where the peak of the sound speed goes over 1. These models are not considered in the analysis in chapter 4.

Just like in the results obtained in the perturbation module for the density contrast, we observe an oscillatory behaviour in the matter power spectrum. The UDM model is capable of producing large oscillations but these only arise for certain combinations of the parameters values and there is a wide range of parameter space that needs to be analysed. Also, even the most critical area with large oscillations may provide viable results when tested with data in the $0.2 < k < 0.9\,h^{-1}$Mpc range, as we will see in Sect. 4.3.2.

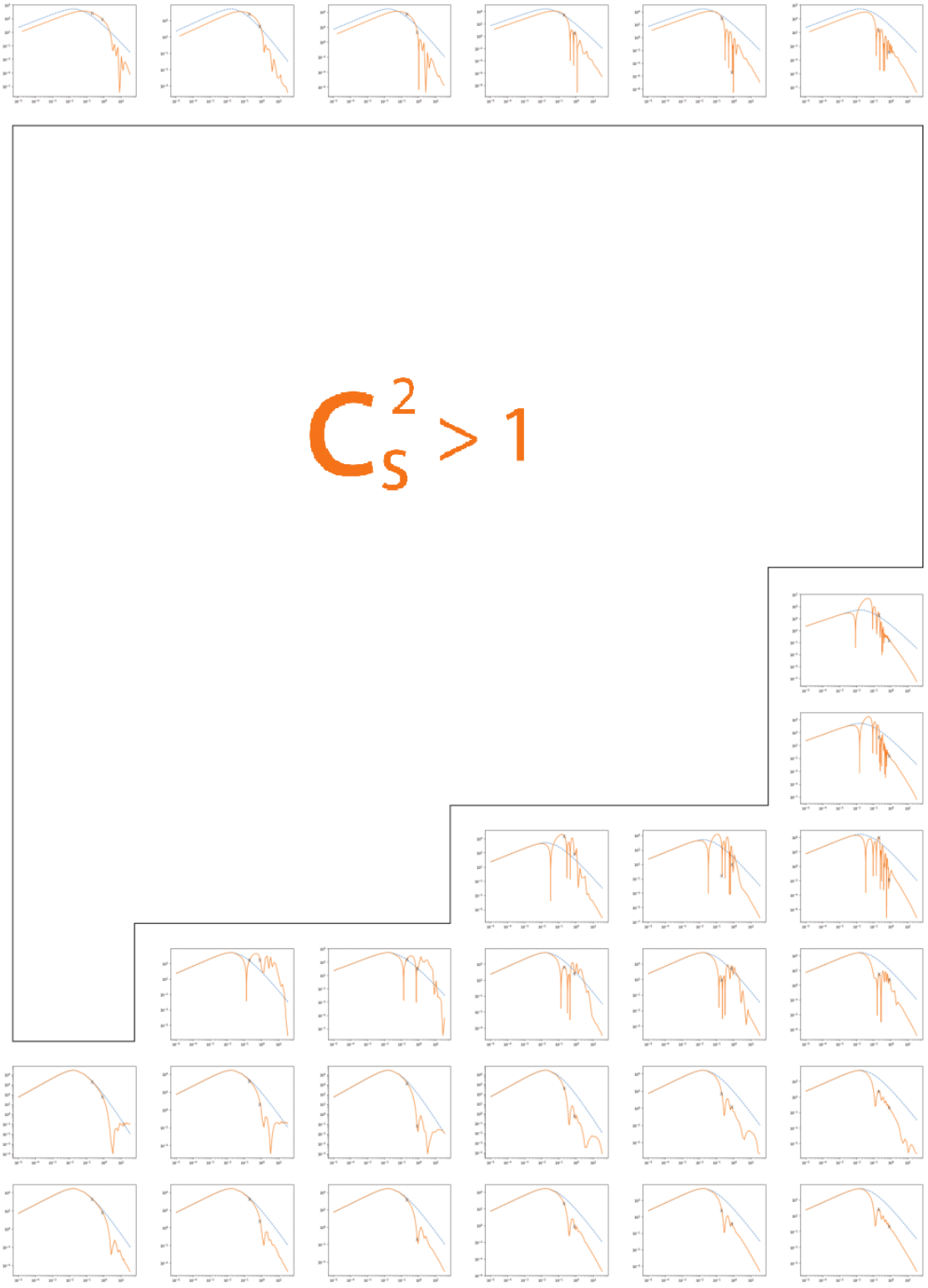

Figure 3.32: Matter power spectrum for a fixed value of $\Omega_{\Lambda udm} = 0.7$ and for $a_t = \{0.001, 0.01, 0.05, 0.1, 0.15, 0.2, 0.3, 0.5, 0.7, 0.9, 1.5\}$, increasing from the bottom to the top and for values of $\beta_{udm} = \{10^3, 5 \times 10^3, 10^4, 5 \times 10^4, 10^5, 5 \times 10^5\}$, increasing the speed of the transition from the right to the left.

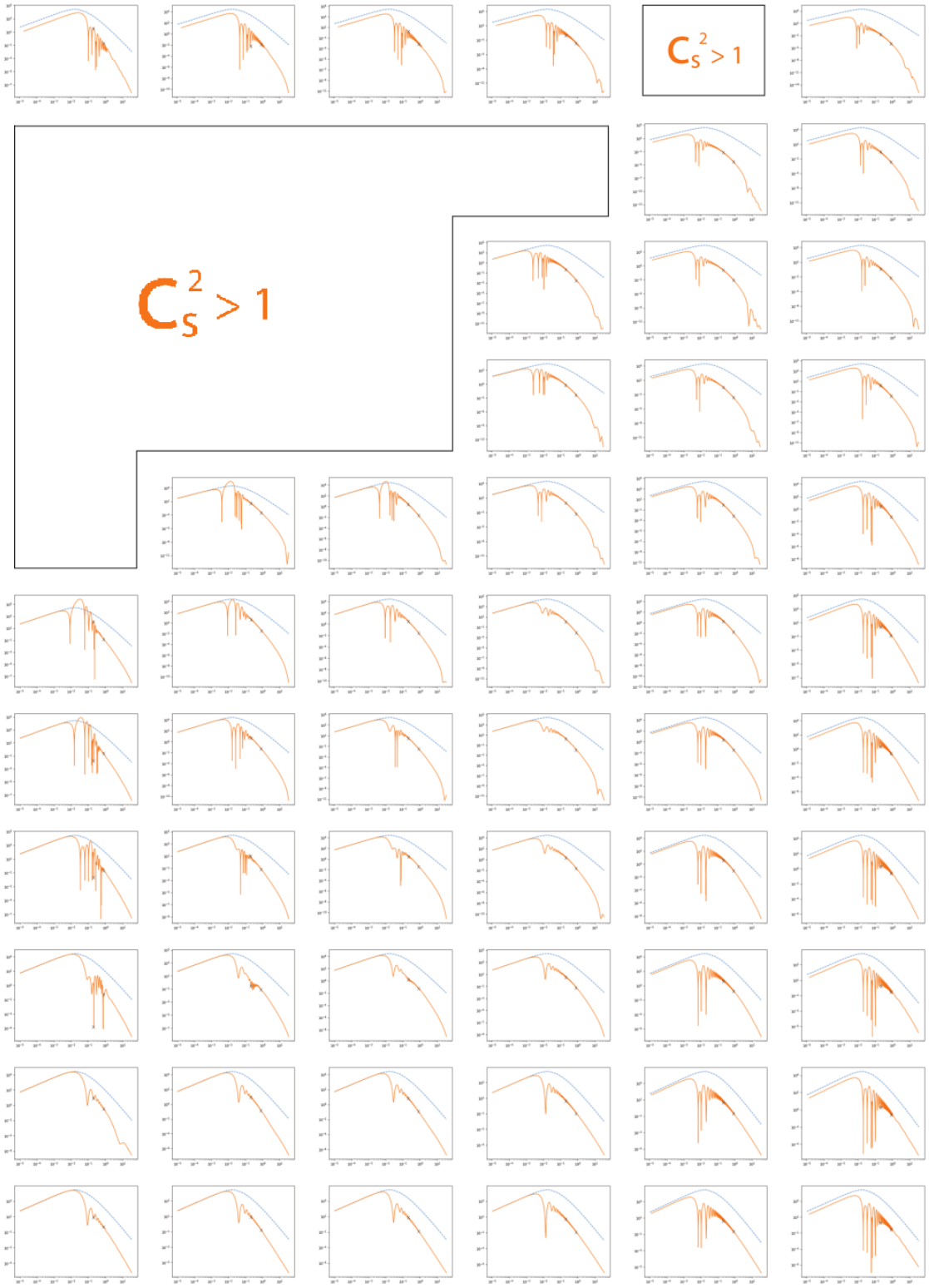

Figure 3.33: Matter power spectrum for a fixed value of $\Omega_{\Lambda udm} = 0.70$ and for $a_t = \{0.001, 0.01, 0.05, 0.1, 0.15, 0.2, 0.3, 0.5, 0.7, 0.9, 1.5\}$, increasing from the bottom to the top and for values of $\beta_{udm} = \{0.1, 1, 10, 50, 100, 500\}$, increasing the speed of the transition from the right to the left.

Chapter 4

Testing cosmological models

After the implementation of the model it is time to test it with several quantities that can be observed and used to constrain the parameters space of the model.

In this chapter we start by presenting the current constraints on the UDM model based on background tests. Then we will present the analysis made in this dissertation, where we test the model first with a combination of SNe Ia, BAO and CMB data, and later by introducing structure formation using weak lensing data.

4.1 Background tests

The UDM model that we study in this dissertation was already tested at background level in [51]. There, the authors used a combination of data related with quantities obtained in the homogeneous study of the model. They used two background features of CMB data, which are the scaled distance to the photon-decoupling surface

$$R \equiv \sqrt{\Omega_m H_0^2}\frac{r(z_*)}{c}\,, \tag{4.1}$$

and the angular scale of the sound horizon at the photon-decoupling epoch

$$l_a \equiv \pi\frac{r(z_*)}{r_s(z_*)}\,, \tag{4.2}$$

where $r(z_*)$ is the comoving distance to the photon-decoupling surface lying at redshift z_* and $r_s(z_*)$ is the comoving sound horizon at z_*. These quantities are measured in the CMB observations, for example l_a is the scale of the first peak in the CMB power spectrum, and can be calculated for the UDM model as a function of its parameters, allowing to estimate the parameter values and test the model.

In [51], they also used BAO data, which depend on $H(z)r_s(z_d)/c$ and D_A (angular diameter distance). Finally, they also used SNe Ia data which provide the distance modulus, which is a quantity that can be computed theoretically for the UDM model.

$$\mu(z) = 5\log_{10} d_L(z) + \mu_0\,, \tag{4.3}$$

Model	h	Ω_c	Ω_b	a_t	β	Ω_Λ	χ^2_{red}	$\ln B_{i\Lambda}$
UDM	$0.69508^{+0.00068}_{-0.00064}$	$0.2445^{+0.00011}_{-0.00012}$	$0.04626^{+0.00024}_{-0.00026}$	$0.17^{+0.010}_{-0.011}$	552^{+75}_{-69}	$0.7091^{+0.0015}_{-0.0013}$	0.9501	+0.791
ΛCDM	$0.6906^{+0.0090}_{-0.0093}$	$0.245^{+0.011}_{-0.010}$	$0.0462^{+0.00097}_{-0.00096}$	–	–	$0.708^{+0.011}_{-0.012}$	0.9488	0

Table 4.1: Summary of the constraints (median values and 1-σ intervals) for the model parameters using CMB, BAO and SN data. The minimum reduced χ^2 and the Bayes factor with respect to ΛCDM are also shown.

where d_L is the luminosity distance that can be computed from

$$d_L(z) = (1+z)\int_0^z \frac{dz'}{E(z')}\,. \tag{4.4}$$

In their analysis, the model was found to fit the data as well as the concordance model does.
The Bayes factor is the ratio between the evidences of two models and is a criteria to make model selection. We see in Tab. 4.1 that the UDM model is slightly preferred over the ΛCDM model, with a small positive value of the logarithm of the Bayes factor, despite having two extra parameters. We can also see that the estimated values for the UDM parameters are a scale factor at a value for the transition of $a_t = 0.17$, corresponding to a redshift $z_t = 4.9$, and $\beta = 552$. These parameters were estimated with a good precision of 6 % and 13 % respectively.

Thus, at background level this model is a viable alternative to explain the late accelerated expansion of the universe.

4.2 Tests in the inhomogeneous universe

Now, we will describe the analysis performed in this dissertation, concerning the tests at perturbation level. For that, we will start by introducing the structure formation observable that we used (weak gravitational lensing). Then we will show the analysis procedure and in particular the Markov Chain Monte Carlo (MCMC) code that we used (MontePython), for parameter estimation. There are two main parts in the code, the algorithm for sampling the parameters space and the likelihood codes of the various datasets.
Finally, we present the results.

4.2.1 Weak gravitational lensing

Cosmological weak gravitational lensing, also known as cosmic shear, is the deflection of photons paths caused by inhomogeneities in the universe where the photons propagate. The photons are emitted by astrophysical sources such as galaxies, and this lensing effect is caused by the variation of density, and therefore by the gravitational potentials, that exist along the propagation path. In that way, cosmic shear is a way to learn more about the distribution of matter in the universe. Since cosmological models make predictions of how matter is distributed in the universe, cosmic shear is then an excellent tool to discover the best model for the universe.

In practice, if light being emitted at an angular position β is observed at a different angular position θ, it is because it was deflected by a deflection vector α caused by the gravitational potentials (see Fig. 4.1), meaning that α is the field that contains the information that we want.

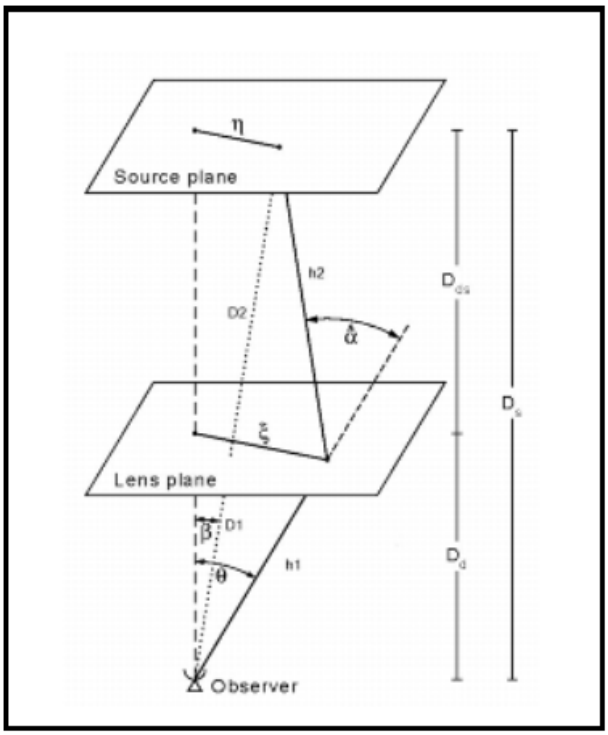

Figure 4.1: Illustration of the lens effect, showing a source-lens-observer configuration. The angular positions $\vec{\beta}$ and $\vec{\theta}$ are defined with respect to the optical axis. D_s, D_d and D_{ds} are the distances from observer to source, observer to lens, and lens to source, respectively. Figure reproduced from [52].

From the figure, we can see that the lens equation that relates the source and image positions is

$$D_s\vec{\theta} = D_s\vec{\beta} + 2D_{ds}\frac{\vec{\alpha}}{2}. \tag{4.5}$$

In the case of an extended source, neighbouring points have slightly different deflections, meaning that the shape of an extended object is distorted. If we make a Taylor expansion of the lens equation, we obtain

$$\beta(\theta) = \beta(\theta_0) + A(\theta_0).(\theta - \theta_0), \tag{4.6}$$

which defines the amplification matrix that gives us the lensing transformation between source and image planes.

$$A_{ij}(\theta) = \frac{\partial\beta_i}{\partial\theta_j} = \left(\delta_{ij} - \frac{\partial\alpha_i}{\partial\theta_j}\right). \tag{4.7}$$

A general matrix of linear distortion is a combination of convergence/expansion, shear and rotation. Meaning that we can decompose a general distortion matrix in a diagonal part, a traceless symmetric

and a traceless antisymmetric part, respectively.

$$A = \begin{bmatrix} k & 0 \\ 0 & k \end{bmatrix} + \begin{bmatrix} \gamma_1 & \gamma_2 \\ \gamma_2 & -\gamma_1 \end{bmatrix} + \begin{bmatrix} 0 & w \\ -w & 0 \end{bmatrix}$$

We need to see how to relate the deflection field $\vec{\alpha}$ with the deflection potential. Let us consider that the light that comes from the source passes then through a local potential ϕ. The potential can be included as a scalar perturbation in the FLRW metric, as we saw in section 1.2

$$ds^2 = -(1+2\phi)\,dt^2 + (1-2\phi)\left[dx_1^2 + dx_2^2 + dx_3^2\right]. \tag{4.8}$$

Let us consider photon trajectories in this metric. From the equation of geodesic deviation we can find the following differential equation for the separation vector ($\vec{x}$) between the photon trajectory and the optical axis, as function of comoving radial distance w [52]

$$\frac{d^2\vec{x}}{dw^2} + K\vec{x} = -2\left[\vec{\nabla}_\perp\phi\left(\vec{x}\left(\vec{\theta},w\right),w\right) - \vec{\nabla}_\perp\phi\left(0,w\right)\right], \tag{4.9}$$

where K is the curvature of the universe. This shows that the separation vector, and consequently the deflection, depends on the gradient of the potential in the plane orthogonal to the trajectory (meaning in the lens plane).

The equation has the following solution

$$\vec{x}\left(\vec{\theta},w\right) = f_K(w)\vec{\theta} - 2\int_0^w dw^{'} f_K(w-w^{'})\left[\vec{\nabla}_\perp\phi\left(\vec{x}\left(\vec{\theta},w^{'}\right),w^{'}\right) - \vec{\nabla}_\perp\phi\left(0,w^{'}\right)\right]. \tag{4.10}$$

We can write this solution in terms of angular positions

$$\beta_i\left(\vec{\theta},w\right) = \theta_i - 2\int_0^w dw^{'}\frac{f_K\left(w-w^{'}\right)}{f_K\left(w\right)} f_K\left(w^{'}\right)\left[\phi_{,i}\left(\vec{x}\left(\vec{\theta},w^{'}\right),w^{'}\right) - \phi_{,i}\left(0,w^{'}\right)\right]. \tag{4.11}$$

This has exactly the structure of the lens equation Eq. (4.5), telling us that the second term of the right-hand side is the solution for the deflection as a function of the potential. where the second term is the solution for the deflection as a function of the potential. This shows that the total deflection is the integral over all local deflections, each one multiplied by a 'weight' or efficiency factor that is essentially

$$\frac{D_{ds}D_d}{D_s}. \tag{4.12}$$

From Eqs. (4.7) and (4.8), we know that the spatial derivatives of the deflection field define the optical scalar fields, the elements of the amplification matrix. We see then that they are second-order derivatives of an effective cosmological lensing potential defined as

$$\psi\left(\vec{\theta},w\right) = 2\int_0^w dw^{'}\frac{f_K\left(w-w^{'}\right)}{f_K\left(w\right)} f_K\left(w^{'}\right)\phi\left(f_K\theta,w^{'}\right). \tag{4.13}$$

With this definition we can write the optical scalars as

convergence

$$k = \frac{1}{2}\left(\psi_{,11} + \psi_{,22}\right). \tag{4.14}$$

shear

$$\gamma_1 = \frac{1}{2}\left(\psi_{,11} - \psi_{,22}\right) \quad , \quad \gamma_2 = \psi_{,12}, \tag{4.15}$$

and rotation

$$w = 0. \tag{4.16}$$

The convergence k in Eq. (4.14), is the Laplacian of a potential and can be related with the mass of the lens through the Poisson equation

$$\nabla_p^2 \phi = 4\pi G\bar{\rho}\delta = a^2 4\pi G\Omega_m \rho_c a^{-3}\delta = \frac{3H_0^2\Omega_m\delta}{2a}. \tag{4.17}$$

This allows us to obtain the dependency of the lensing optical scalars fields on the density contrast field

$$k\left(\vec{\theta}, w\right) = \frac{3}{2}H_0^2\Omega_m \int_0^w dw^{'} \frac{f_K\left(w - w^{'}\right) f_K\left(w^{'}\right)}{f_K\left(w\right) a\left(w^{'}\right)} \delta\left(f_K\left(w^{'}\right)\vec{\theta}, w^{'}\right). \tag{4.18}$$

This is the convergence field produced by the lenses $\delta(w')$ located in the comoving distance range $w' \in [0, w]$. They affect the image of a single source located at w. In practice there is not a single source but a distribution of source galaxies that are distributed over redshift, between 0 and a maximum possible distance w_H.
The convergence then becomes

$$k\left(\vec{\theta}\right) = \frac{3}{2}H_0^2\Omega_m \int_0^{w_H} dw^{'} \frac{f_K\left(w^{'}\right)}{a\left(w^{'}\right)} \delta\left(f_K\left(w^{'}\right)\vec{\theta}, w^{'}\right) g\left(w^{'}\right), \tag{4.19}$$

with

$$g\left(w^{'}\right) = \int_w^{w_H} dw\, p\left(w\right) \frac{f_K\left(w - w^{'}\right)}{f_K\left(w\right)} \tag{4.20}$$

being the contribution weight of each source galaxy w' that belongs to the source redshift distribution $p(w)$. The power spectrum of the convergence field is then related to the matter power spectrum

$$P_k\left(l\right) = \frac{9}{4}H_0^4\Omega_m^2 \int_0^{w_H} dw \frac{g^2\left(w\right)}{a^2\left(w\right)} P_\delta\left(\frac{l}{f_K\left(w\right)}, w\right). \tag{4.21}$$

That means that if our model predicts a certain P_δ we can also compute the P_k that will correspond to a certain source distribution.

Since the convergence field and the shear field are second-order derivatives of the cosmological lensing potential, they are related. It is easy to compute their relation in the Fourier space, which is,

$$\tilde{\gamma}\left(\vec{l}\right) = \left(\frac{l_1^2 - l_2^2 + 2il_1l_2}{l^2}\right)\tilde{k}\left(\vec{l}\right), \tag{4.22}$$

and implies that their power spectra are identical

$$P_\gamma\left(l\right) = P_k\left(l\right). \tag{4.23}$$

This procedure allows us to relate the matter power spectrum to the convergence power spectrum, to the shear power spectrum and to the shear correlation function. The shear correlation function or power spectrum are the quantities usually computed from measurements of ellipticity of galaxies in weak lensing surveys. This then allow us to compare our theoretical calculation of the shear power spectrum with the observed ones and compare them and test our model.
It is important to note that this procedure allows us to compute the linear power spectrum. However, on small scales ($k > 0.2h\,\mathrm{Mpc}^{-1}$) the dark matter density contrast is large and non-linear corrections may be needed.

The regime where the non-linearity starts depends on the model and how fast or slow the structure forms, however we expect that any model will require some level of non-linear corrections. To solve this problem what is usually done is to use of N-body simulations that allow us to evolve the model starting from a time where the power spectrum is still linear at all scales. These simulations demand heavy computation and what is common to do, for example in the ΛCDM, is to evolve the system for certain parameter values and from these simulations extrapolate a fitting function that allows to correct the linear power spectrum in the non-linear regime [53].

4.2.2 KiDS Survey

The Kilo-Degree Survey (KiDS) is an ongoing ESO optical survey that will try to cover 1350 deg^2 of the extragalactic sky in four bands (u,g,r,i). It uses the OmegaCAM CCD mosaic camera mounted at the Cassegrain focus of the VLT Survey Telescope (VST). This combination of camera and telescope was specifically designed for the weak lensing studies [54, 55].

A weak lensing cosmological survey measures the ellipticity of the image galaxies. The ellipticity is a two component polar vector with a modulus describing the deviation from circularity and a direction. In the weak lensing approximation, where the optical scalars are small, the observed ellipticity is in fact the sum of two features: the intrinsic ellipticity of the galaxies plus the shear caused by the lensing potential [52], $\gamma_{ob} = \gamma_s + \gamma_{cosmo}$. The intrinsic ellipticities of galaxies are not necessarily independent because the orientations of galaxies are determined by physical processes that could produce correlated intrinsic alignments. For this reason the correlation function measured by KiDS is

$$\langle\gamma_{ob}\gamma_{ob}\rangle = \langle\gamma_{cosmo}\gamma_{cosmo}\rangle + \langle\gamma_{cosmo}\gamma_s\rangle + \langle\gamma_s\gamma_{cosmo}\rangle + \langle\gamma_s\gamma_s\rangle. \tag{4.24}$$

The terms $\langle\gamma_{cosmo}\gamma_s\rangle$, $\langle\gamma_s\gamma_{cosmo}\rangle$ and $\langle\gamma_s\gamma_s\rangle$ are three types of intrinsic alignments, while $\langle\gamma_{cosmo}\gamma_{cosmo}\rangle$ is the shear correlation function containing the cosmological information. This equation is then a biased estimator of the shear correlation function.

In our analysis we have used the KiDS-450 dataset where the galaxies ellipticities were measured using 450 deg^2 of imaging data. From the observed ellipticities, the KiDS team computed the ellipticity correlation function $\langle\gamma_{cosmo}\gamma_{cosmo}\rangle$ and the ellipticity power spectrum with a quadratic estimator. This

was done separating the source galaxies in three redshift bins (*zbins*: $0.1-0.3$, $0.3-0.6$ and $0.6-0.9$), producing five different shear power spectrum spectra and correlation functions (bin1-bin1, bin2-bin1, bin2-bin2, bin3-bin3, bin1-bin3), each of the five power spectra measured on angular scales ranging from $l = 76$ to $l = 1310$.
We will work with the publicly available shear power spectra and will use the public likelihood code provided in [55].

To compute the likelihood of our UDM model given these KiDS data we will need to specify not only the cosmological parameters values, but also six extra (nuisance) parameters that account for the bias in the measurements. These are: the 3 parameters *A_noise* $z_{1,2,3}$ that represents the uncertainty associated to the 3 redshift bins of the galaxies. The *m_corr* parameter that represents the uncertainty on the calibration of the ellipticity measurement of the galaxies. The *A_IA* parameter that represents the uncertainty in the amplitude of the intrinsic alignment effect. The *A_bary* parameter allows for an uncertainty on the dark matter power spectrum amplitude due to feedback from baryons. Also, the likelihood code by default already accounts for the uncertainty in the $n(z)$ distribution of galaxies by randomly choosing one of one thousand realisations.

4.3 Analysis

4.3.1 MontePython

MontePython is a Monte Carlo code for Cosmological Parameter extraction. It is prepared to work integrated with CLASS and contains already several likelihood codes for the most recent experiments [56]. It includes several methods to sample the parameter space: Metropolis-Hastings [57], Nested Sampling [58, 59] (through MultiNest [60]), EMCEE [61] (through CosmoHammer [62]) and Importance Sampling.

In our analysis we will mostly use the Metropolis-Hastings algorithm, which is a Markov Chain Monte Carlo (MCMC) method. In this method, points in the parameter space are generated in sequence from an auxiliary proposal distribution. Each point may be accepted or rejected by evaluating its likelihood against the data and comparing it with the likelihood of the previous point. The algorithm is designed such that the sequence of points mainly moves towards regions of higher likelihood, probing those regions with higher resolution. The chain of points formed is called a Markov chain because each point depends on the previous point of the chain. When the process is finished, the resulting chain is a representative sample of the probability distribution in the parameters space.

Running the code is very straightforward. After defining several configurations, we are ready to use it. MontePython comes with only two main commands. The first one is used to run a chain and the second one reads the chains and produces several outputs such as covariant matrices, plots or bestfit values. To see the list of arguments available in each command all we need to do is type *"python montepython/Montepython.py run -h/–help"* for the run, and *"python montepython/Montepython.py info -h/–help"* for analysing the chain.

To run a chain the basic thing that we need is to choose the data that we want to use (e.g. JLA), which is defined by an input file that contains the data as well as its nuisance parameters, the free parameters of the model, the derived parameters that we want and the fixed parameters (e.g. JLA.param).We also need to define the place where we want to store the chains (e.g. *"python*

montepython/Montepython.py run -p JLA.param -o chains/JLA"). Other arguments are the sampling method (e.g. *-m NS*), the number of iterations (e.g. *-N 1000*), if we want to use a specific covariant matrice (e.g. *-c covmat/JLA.covmat*) or the bestfit values to start the chain (e.g. *-b bestfit/JLA.bestfit*). As an example Fig. 4.3 shows the input file to test the UDM model against JLA.

```
#------Experiments to test (separated with commas)-----

data.experiments=['JLA']

#------ Parameter list -------
# data.parameters[class name] = [mean, min, max, 1-sigma, scale, role]
# - if min max irrelevant, put to -1 or None (if you want a boundary of -1, use -1.0)
# - if fixed, put 1-sigma to 0
# - if scale irrelevant, put to 1, otherwise to the appropriate factor
# - role is either 'cosmo', 'nuisance' or 'derived'


# Cosmological parameters list
data.parameters['a_transition_udm'] = [0.2,  0.15, 1, 0.005,  1, 'cosmo']
data.parameters['log_beta_udm']     = [1, -2.0, 3, 0.01,  1, 'cosmo']
data.parameters['Omega_lambda_udm'] = [0.72,  0.01, 1, 0.005,  1, 'cosmo']


# Nuisance
data.parameters['alpha']   = [0.15 ,  None, None, 0.001, 1, 'nuisance']
data.parameters['beta']    = [3.559,  None, None, 0.02,  1, 'nuisance']
data.parameters['M']       = [-19.02, None, None, 0.004,  1, 'nuisance']
data.parameters['Delta_M'] = [-0.10,  None, None, 0.004,  1, 'nuisance']


data.cosmo_arguments['omega_cdm'] = 0.001
data.cosmo_arguments['Omega_Lambda'] = 0
data.cosmo_arguments['a_ini_over_a_today_default'] = 1.e-13
data.cosmo_arguments['back_integration_stepsize'] = 7.e-3
data.cosmo_arguments['tol_background_integration'] = 1.e-2


#------ Mcmc parameters ----
# Number of steps taken, by default (overwritten by the -N command)
data.N=10
# Number of accepted steps before writing to file the chain. Larger means less
# access to disc, but this is not so much time consuming.
data.write_step=5
```

Figure 4.2: Input file used to run MontePython and test our UDM model againsts JLA.

In the input file we can see the free parameters associated to the model that we want to extract, named "cosmo" parameters, the "nuisance" parameters associated to the experiment used, and the fixed parameters of the model named "data.cosmo_arguments".

4.3.2 Methodology

Before testing the model with weak lensing, we first calculate the combined likelihood of three surveys that contain three cosmological probes. These are JLA for Supernovae, BOSS for BAO, and Planck for CMB. Before decoupling sound waves travelled on the baryon-photon plasma. At decoupling, this propagation stopped and a baryonic matter overdensity remained at a distance equal to the sound horizon from dark matter overdensity locations. This overdensity is still detected today in the form of a peak in the matter correlation function, or in the form of oscillations in its Fourier transform, the matter power spectrum. The measured scale where the peak appears constrains a cosmological distance. We used the BOSS 2014 combined BAO data provided in MontePython and the corresponding likelihood. This consist of six data points taken from the BOSS CMASS-DR11 and LOWZ-DR11 samples [63],

BOSS LyAQSO [64], the SDSS DR7 main galaxy sample [65] and the 6dF Galaxy survey [66]. We can see more clearly in the likelihood code that the most important theoretical quantities that we require from CLASS is the angular-diameter distance (D_A), defined as

$$D_A = \frac{1}{(1+z)} \int_0^z \frac{dz'}{H(z')}, \tag{4.25}$$

and the volume distance, defined as

$$D_V = \left[D_A^2 (1+z)^2 \frac{z}{H(z)} \right]^{\frac{1}{3}}. \tag{4.26}$$

For the SNe Ia tests we used the JLA sample, a data set of 740 SNe Ia that includes data from SDSS and SNLS surveys [67]. We used the likelihood already implemented in Monte Python, "*JLA_simple*". This code only includes one nuisance parameter "M" related to the uncertainty in the SNe Ia absolute magnitude instead of using the full "*JLA*" likelihood code that includes all the four nuisance parameters of JLA.

For the CMB we use the Planck 2015 data [6]. The likelihood codes used were also provided by the Planck Team [1] and installed in MontePython. The likelihoods used for the analysis were the "*Planck_lowl*" that measure the CMB at small scales and the "*Planck_highl_lite*" that measure the CMB at larger scales. For the large scales the Planck power spectrum is derived from Planck data combined with the nine-year WMAP sky maps [68], and the 408-MHz survey [69], including 93% of the sky. For high l we use the lite version of likelihood like we did for JLA test because this version has most of the nuisance parameters fixed, leaving us only with one CMB nuisance parameter allowing us to work in a lower dimensional parameters space and have a faster convergence.

The analysis with these three datasets is different from the analysis described in Section 4.1, since now we are testing the model using the full CMB power spectrum instead of only using the first peak location and distance information. This is already a test in the inhomogeneous universe (at high redshift) and no longer a background test. We expect that the most relevant test of the UDM model in the inhomogeneous universe will be the one made with weak lensing (a test of structure formation at lower redshifts, after transition). However, it is very important to combine these datasets in order the break degeneracies between the cosmological parameters.

Another important point to consider is the following. In our model, the rapidity of the transition, defined by the parameter β, is not constrained by any upper limit, however, as it was discussed before, for several combinations of β, $\Omega_{\Lambda udm}$, and $a_{transition}$ we expect c_s^2 to be larger than one. In fact, for very high values of β, only a very small region of $a_{transition}$ gives a $c_s^2 \leq 1$. (for example, $\beta = 500000$ and $\Omega_{\Lambda udm} = 0.72$, only the range $a_{transition} \leq 0.041$ provides a sound speed with a peak lower than one). This means that if we try to run a chain exploring a wide prior for $a_{transition}$ and β at the same time such as $a_{transition} \in [0, 1]$ and $\beta \in [0, 500000]$, a very large amount of points will be rejected, which could be a problem if there is not enough time and computer resources. To avoid this problem and obtain faster results for our model we decided to separate the space of parameter of the model in the three regions shown in Tab. 4.2. For all the combinations of likelihoods that we used, we ran separate chains confined to each region.

[1] Likelihood downloaded from (http://pla.esac.esa.int/pla)

	$a_{t,udm}$	β_{udm}	$\Omega_{\Lambda udm}$
regime 1	0.15 - 1	0.01 - 10^3	0.01 - 1
regime 2	0.055 - 0.15	0.01 - $10^{4.5}$	0.01 - 1
regime 3	0.001 - 0.055	0.01 - $10^{5.7}$	0.01 - 1

Table 4.2: The allowed ranges for the parameters of the model in the three cases.

Using the Metropolis-Hasting algorithm, we have made a total of twelve different analyses. First, we used the combined likelihood of Planck, BAO from BOSS and JLA for the three regimes of Tab. 4.2 to test a cosmological model with four free parameters: the three model parameters ($a_{transition}$, β_{udm}, $\Omega_{\Lambda udm}$) and the amplitude of the primordial power spectrum, A_s. In these case, all the nuisance parameters and remaining cosmological parameters were kept fixed. This is the minimal UDM cosmological model.

Then, we used the same combined likelihood for the three regimes of a_t, but this time considering seven free parameters: the three UDM parameters and four other fundamental cosmological parameters: the amplitude of the primordial power spectrum (A_s) and the slope (n_s), the baryon density (Ω_b) and the reduced Hubble constant (h).

Note that this corresponds to the so-called vanilla six parameter cosmological model studied by Planck for ΛCDM (minus the reionization parameter τ_{re} not relevant here) but for the case of UDM with two extra parameters. Thus, the corresponding vanilla UDM cosmology has seven free parameters. Note that we do not include a dark matter density parameter, but used the $\Omega_{\Lambda udm}$ parameter instead, which is more convenient in the UDM model.

After that, we added KiDS data to the combined likelihood and performed six more analyses. These correspond to the same three sets of minimal and vanilla models, with one extra nuisance parameter, the intrinsic alignment amplitude (A_{IA}).

When including KiDS data, in principle we need to consider the non-linear matter power spectrum. CLASS computes the linear power spectrum and then applies a non-linear correction (HALOFIT) valid for ΛCDM. However, in many cases we were not able to use the non-linear module, that applies the HALOFIT to the matter power spectrum, because of the large oscillations that prevents the code to calculate the scale where the matter power spectrum becomes non-linear.

To be able to use KiDS data in this situation, we decided to investigate if the KiDS datapoints are close to the linear regime. The largest angular scale measured is the datapoint in the angular bin l that ranges from the multipole $l = 76$ to $l = 220$, which corresponds to an angular separation of $\Theta = 98.2\,\text{arcmin}$ to $\Theta = 284.2\,\text{arcmin}$. The efficiency of lensing is greater for lenses placed at half way between source and observer, according to the efficiency factor (Eq. (4.12)). This means that for each of the three redshift bins, we may compute the source distance and also the distance to the most significant lens. From the distance to the lens, we compute the physical scale that corresponds to the angular scale. We find that the largest scale contributing to the first l-bin is $k = 0.28\,\text{h/Mpc}$. Doing the same calculation for the second l-bin (ranging form $l = 221$ to $l = 420$), we find that it corresponds to a minimal scale of $k = 0.84\,\text{h/Mpc}$. Therefore, $k = 0.28 - 0.84$ is the widest range of the matter power spectrum probed by the KiDS lensing power spectra. These two data points are then in the mildly non-linear regime, since the threshold is usually considered to be $k = 0.2\,\text{h/Mpc}$. To proceed, we computed the matter power spectrum for the concordance ΛCDM model with and without the HALOFIT correction. The linear and non-linear power spectra are identical for large scales ($k < 0.2\,\text{h/Mpc}$) and deviate for smaller scales. We then computed the likelihood of these ΛCDM power

spectra using only these two points in the five KiDS power spectra. We found that the two likelihoods (ΛCDM with and without HALOFIT correction) deviate by 15%. We also verified that the deviation increases a lot if we increase the number of KiDS data points, going into the stronger non-linear regime.

We decided then to use only these two KiDS scales and used the linear power spectrum in all our analyses, keeping in mind that we are implicitly introducing an extra theoretical uncertainty of around 15% in the statistical analysis.

In the following sections, we present the results of the twelve cases. We remind that for each of the three a_t regimes we made four different tests: minimal and vanilla, with and without lensing data. For the non-UDM parameters we used standard flat priors already suggested in [55].

For each analysis, we usually ran several chains, to be able to compare them and check for convergence, using MontePython tools. The first part of the chains are discarded, since the points are not yet representative of the final distribution. Finally, we found out that the most critical part of the running procedure is the definition of the step of the proposal distribution. MontePython also allows us to choose the number of parameters that change at each iteration and to introduce a covariance matrix, such that the points move preferentially along an eigenvector direction. For the cases with complex likelihoods we had to try many different ways before obtaining an efficient sampling.

4.3.3 Regime 1: UDM late transition

In Table 4.3 we can find the mean and the marginalized 2-σ confidence interval for the first regime (with a_t between 0.15 and 1) in the minimal set-up of four free parameters. In table 4.4 we give the results for the same set-up but now including KiDS data which introduces the intrinsic alignment parameter. We also show results for the σ_8 parameter (the amplitude of the linear matter power spectrum at redshift zero around the scale 8 Mpc), which is a derived parameter. Fig. 4.3 show us the corresponding posterior probabilities for each parameter, as well as two-dimensional contours with 1-σ and 2-σ confidence regions.

Parameters	best-fit	mean$\pm\sigma$	95% lower	95% upper
a_t	0.15	$0.1502^{+2.5e-05}_{-0.00015}$	0.15	0.1505
$log_{\beta,udm}$	1.177	$1.17^{+0.026}_{-0.026}$	1.117	1.221
$\Omega_{\Lambda udm}$	0.7018	$0.702^{+0.0012}_{-0.0012}$	0.6995	0.7045
$ln10^{10}A_s$	3.112	$3.113^{+0.0019}_{-0.0019}$	3.109	3.117

$-\ln\mathcal{L}_{\min} = 5668.45$, minimum $\chi^2 = 1.134e+04$

Table 4.3: Estimated best-fit, mean, 1-σ uncertainty and 2-σ intervals constraints for regime 1 in the minimal set-up without KiDS data.

Parameters	best-fit	mean$\pm\sigma$	95% lower	95% upper
a_t	0.15	$0.1501^{+2.5e-05}_{-0.00015}$	0.15	0.1504
$log_{\beta,udm}$	1.183	$1.172^{+0.027}_{-0.026}$	1.117	1.225
$\Omega_{\Lambda udm}$	0.7017	$0.7018^{+0.0011}_{-0.0014}$	0.6994	0.7045
$ln10^{10}A_s$	3.11	$3.113^{+0.002}_{-0.0017}$	3.109	3.117
A_{IA}	4.575	prior	prior	prior
$\sigma 8$	0.03554	$0.03545^{+0.00033}_{-0.00037}$	0.03475	0.03616

$-\ln\mathcal{L}_{\min} = 5731.3$, minimum $\chi^2 = 1.146e+04$

Table 4.4: Estimated best-fit, mean, 1-σ uncertainty and the 2-σ intervals constraints for regime 1 in the minimal set-up with KiDS data.

The results are very similar for the two cases. The distribution of a_t values is strongly peaked at the lower end of the allowed range. This result and the higher values of χ^2 in comparison to the regimes 2 and 3 (see sections 4.3.4 and 4.3.5) indicates that this range of values is not favoured for the UDM model.

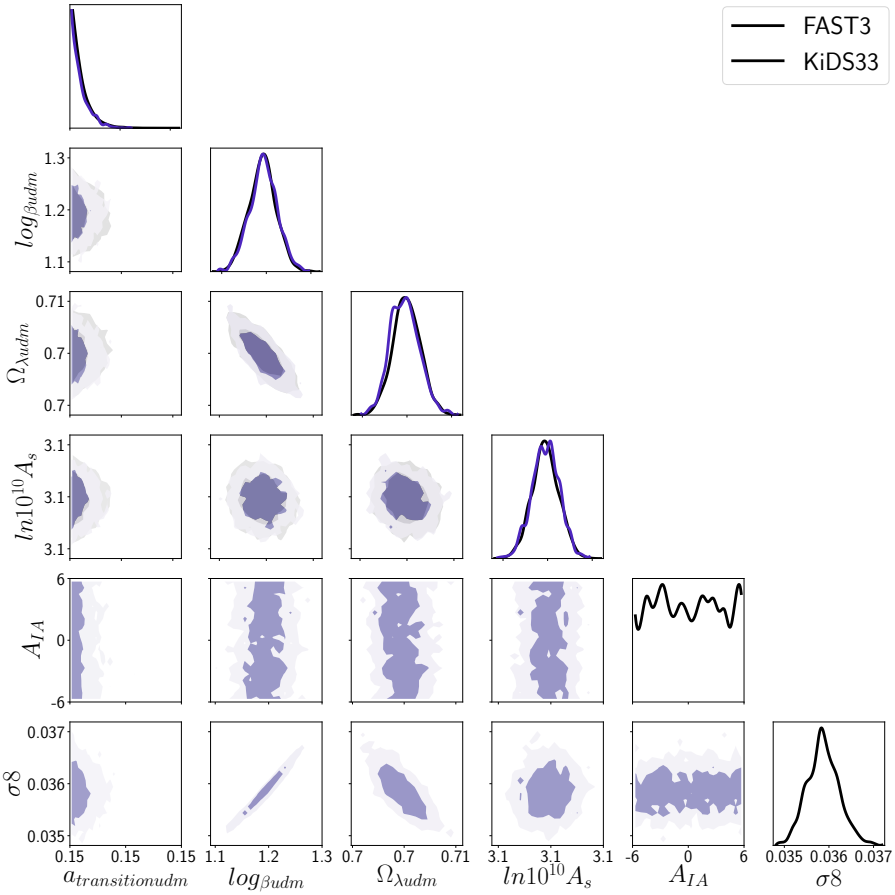

Figure 4.3: Regime 1: Posterior probabilities for each parameter in the minimal set-up, as well as the contours with the 1-σ and 2-σ confidence regions for the analysis with (black lines) and without KiDS (blue lines).

It is also important to note in Fig. 4.3 the anti-correlation relation between $\Omega_{\Lambda udm}$ and β and the strong correlation relation between β and σ_8 in the analysis with KiDS. These two correlations indicate that models with faster transition produce universes with more structure and less dark energy today. Nevertheless, the amount of formed structure is very small for all parameter values in this regime, as seen by the very small value of σ_8 found. This is in fact the reason for the strong rejection of this regime. Finally, the word "prior" in Tab. 4.4 indicates that this parameter is unconstrained by the data and we recover the input flat prior in the result.

In Tables 4.5 and 4.6 we present the results obtained for the same a_t regime but now for the vanilla set-up of seven (eight with KiDS) free parameters. We obtain the same conclusions of the previous analysis with a slight difference in the mean value for $\Omega_{\Lambda udm}$ and β. We obtain, as expected, larger 2-σ intervals since now we have less fixed parameters and we are marginalising over a large number of free parameters. In Fig. 4.4 it is also important to report that we have strong correlation relations between h and $\Omega_{\Lambda udm}$, n_s and β, n_s and $\Omega_{\Lambda udm}$, ω_b and A_s, a slight correlation relations between h and n_s; and strong anti-correlation between n_s and A_s, A_s and β, A_s and $\Omega_{\Lambda udm}$, and a slight anti-correlation between h and A_s.

Parameters	best-fit	mean$\pm\sigma$	95% lower	95% upper
a_t	0.15	$0.1502^{+2.7e-05}_{-0.00016}$	0.15	0.1505
$log_{\beta,udm}$	1.894	$1.895^{+0.021}_{-0.017}$	1.856	1.933
$\Omega_{\Lambda udm}$	0.6536	$0.6547^{+0.0038}_{-0.0048}$	0.6468	0.6629
$ln10^{10}A_s$	3.056	$3.054^{+0.0039}_{-0.004}$	3.046	3.062
ω_b	0.02	$0.01999^{+0.00016}_{-0.00018}$	0.01966	0.02033
n_s	1.048	$1.049^{+0.0058}_{-0.0059}$	1.037	1.06
h	0.6439	$0.6443^{+0.002}_{-0.0029}$	0.64	0.6486

$-\ln\mathcal{L}_{\rm min} = 5537.99$, minimum $\chi^2 = 1.108e+04$

Table 4.5: Estimated best-fit, mean, 1-σ uncertainty and the 2-σ intervals constraints for regime 1 in the vanilla set-up without KiDS data.

Parameters	best-fit	mean$\pm\sigma$	95% lower	95% upper
a_t	0.15	$0.1502^{+2.4e-05}_{-0.00016}$	0.15	0.1505
$log_{\beta,udm}$	1.883	$1.893^{+0.021}_{-0.016}$	1.852	1.931
$\Omega_{\Lambda udm}$	0.6557	$0.6547^{+0.0037}_{-0.005}$	0.6467	0.6632
$ln10^{10}A_s$	3.056	$3.055^{+0.0037}_{-0.0043}$	3.046	3.063
ω_b	0.02009	$0.01998^{+0.00017}_{-0.00016}$	0.01965	0.02032
n_s	1.044	$1.048^{+0.006}_{-0.0057}$	1.037	1.06
h	0.6449	$0.6442^{+0.002}_{-0.0029}$	0.64	0.6486
A_{IA}	-3.163	prior	prior	prior
$\sigma 8$	0.05855	$0.0596^{+0.0021}_{-0.0018}$	0.05559	0.06355

$-\ln\mathcal{L}_{\rm min} = 5600.97$, minimum $\chi^2 = 1.12e+04$

Table 4.6: Estimated best-fit, mean, 1-σ uncertainty and the 2-σ intervals constraints for regime 1 in the vanilla set-up with KiDS data.

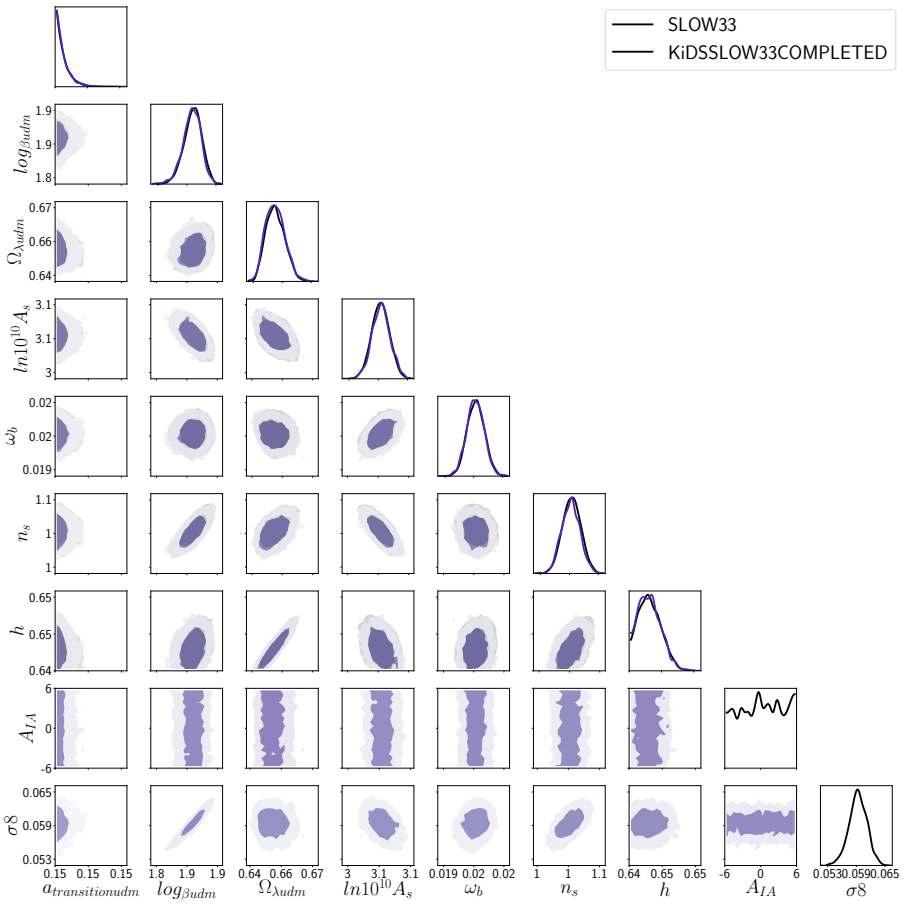

Figure 4.4: Regime 1: Posterior probabilities for each parameter in the vanilla set-up, as well as the contours with the 1-σ and 2-σ confidence regions for the analysis with (black lines) and without KiDS (blue lines).

In conclusion, the KiDS experiment had no impact in the constraint of the parameters in this regime, due to the strong decrease of the amplitude of the matter power spectrum on small scales. We also notice that the best-fit has a significative better χ^2 in the vanilla set-up than in the minimal one. The reason is that by allowing n_s to vary, models with higher n_s become possible, which increases the amplitude of the power spectrum on small scales. This is confirmed by the larger value of σ_8 found. Notice however that the preferred models in this regime have $n_s > 1$, contrary to most inflationary predictions.

4.3.4 Regime 2: UDM mid transition

In this regime, we were not able to find converged chains for the case with KiDS data. The reason why this parameter space is more difficult to analyse than the others is because there are strong oscillations in the matter power spectrum around the two data points of KiDS. These strong oscillations can give a good χ^2 for some parameter values, where the data points happen to be in local maxima of the matter power spectrum, but very bad χ^2 in neighbouring points. This scenario produces a complex likelihood with several peaks, making it hard for the chain to converge. However, even though we could not find

reliable statistical constraints, we were able to find particular models that match the observations as well as ΛCDM, as we can see in Tables 4.8 and 4.10.

In Tables 4.7 and 4.8 we present the results for the second regime in the minimal set-up. We notice that the best-fit is significantly better than in the first regime, and the amount of formed structure (as measured by σ_8) is higher. In Fig. 4.5 we show the corresponding contours. The strong contrast between the smooth contours of the no-KiDS analysis and the plots from the non-converged chain is well visible.

Parameters	best-fit	mean$\pm\sigma$	95% lower	95% upper
a_t	0.06362	$0.06282^{+0.0024}_{-0.0017}$	0.0581	0.06707
$log_{\beta,udm}$	3.092	$3.1^{+0.048}_{-0.056}$	2.989	3.214
$\Omega_{\Lambda udm}$	0.6886	$0.6885^{+0.00077}_{-0.00078}$	0.687	0.6901
$ln10^{10}A_s$	3.113	$3.114^{+0.0041}_{-0.0039}$	3.106	3.122

$-\ln\mathcal{L}_{\min} = 5386.33$, minimum $\chi^2 = 1.077e+04$

Table 4.7: Estimated best-fit, mean, 1-σ uncertainty and the 2-σ intervals constraints for regime 2 in the minimal set-up without KiDS data.

Parameters	best-fit	mean$\pm\sigma$	95% lower	95% upper
a_t	0.06472	0.06433^{+nan}_{nan}	nan	nan
$log_{\beta,udm}$	3.036	3.05^{+nan}_{nan}	nan	nan
$\Omega_{\Lambda udm}$	0.6879	0.6884^{+nan}_{nan}	nan	nan
$ln10^{10}A_s$	3.11	3.111^{+nan}_{nan}	nan	nan
A_{IA}	2.603	1.727^{+nan}_{nan}	nan	nan
$\sigma 8$	0.302	0.3049^{+nan}_{nan}	nan	nan

$-\ln\mathcal{L}_{\min} = 5432.23$, minimum $\chi^2 = 1.086e+04$

Table 4.8: Estimated best-fit, mean, 1-σ uncertainty and the 2-σ intervals constraints for regime 2 in the minimal set-up with KiDS data.

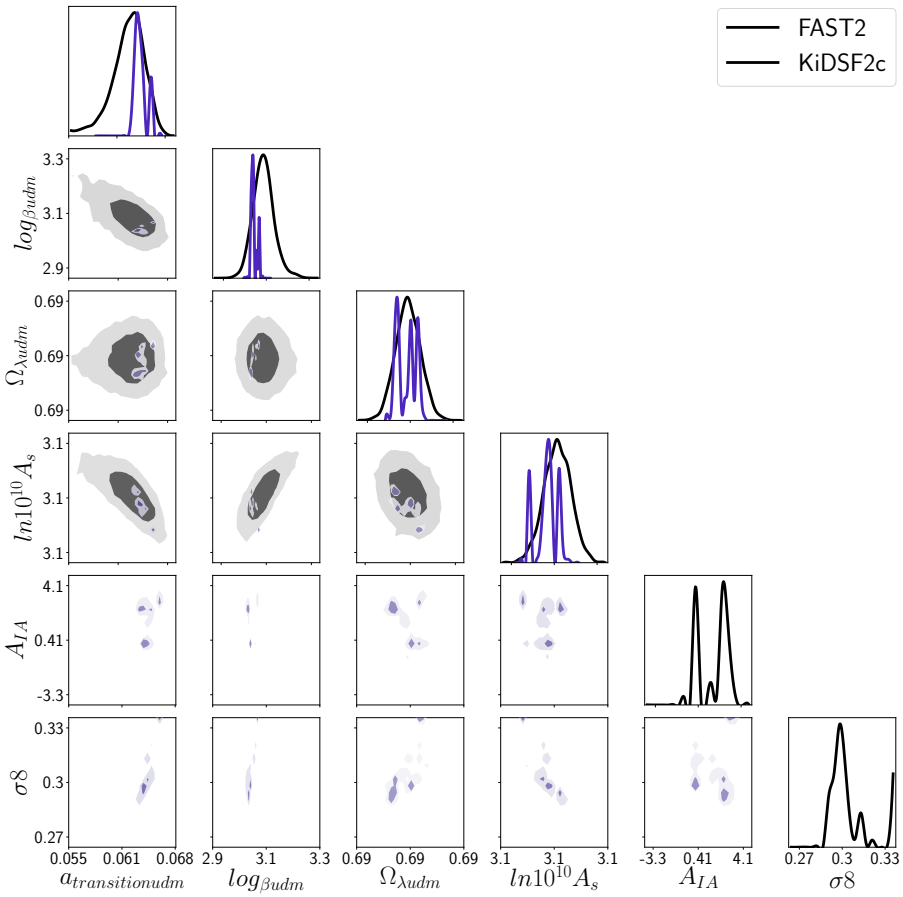

Figure 4.5: Regime 2: Posterior probabilities for each parameter in the minimal set-up, as well as the contours with the 1-σ and 2-σ confidence regions for the analysis with (black lines) and without KiDS (blue lines).

Parameters	best-fit	mean$\pm\sigma$	95% lower	95% upper
a_t	0.0726	$0.0687^{+0.00474}_{-0.00398}$	0.0613	0.0768
$log_{\beta,udm}$	2.87	$2.966^{+0.097}_{-0.16}$	2.757	3.215
$\Omega_{\Lambda udm}$	0.7105	$0.7091^{+0.0058}_{-0.0059}$	0.6977	0.7204
$ln10^{10}A_s$	3.092	$3.099^{+0.0087}_{-0.014}$	3.081	3.12
ω_b	0.0229	$0.02265^{+0.00025}_{-0.00034}$	0.02206	0.02327
n_s	0.951	$0.9578^{+0.0056}_{-0.01}$	0.9436	0.9762
h	0.6953	$0.6932^{+0.0046}_{-0.005}$	0.6836	0.7029

$-\ln\mathcal{L}_{\min} = 5378.17$, minimum $\chi^2 = 1.076e+04$

Table 4.9: Estimated best-fit, mean, 1-σ uncertainty and the 2-σ intervals constraints for regime 2 in the vanilla set-up without KiDS data.

Parameters	best-fit	mean$\pm\sigma$	95% lower	95% upper
a_t	0.06718	0.06603^{+nan}_{nan}	nan	nan
$log_{\beta,udm}$	3.024	3.021^{+nan}_{nan}	nan	nan
$\Omega_{\Lambda udm}$	0.7095	0.7077^{+nan}_{nan}	nan	nan
$ln10^{10}A_s$	3.102	3.106^{+nan}_{nan}	nan	nan
ω_b	0.02237	0.02248^{+nan}_{nan}	nan	nan
n_s	0.9592	0.9619^{+nan}_{nan}	nan	nan
h	0.693	0.692^{+nan}_{nan}	nan	nan
A_{IA}	-4.584	-4.103^{+nan}_{nan}	nan	nan
$\sigma 8$	0.3385	0.324^{+nan}_{nan}	nan	nan

$-\ln\mathcal{L}_{\rm min} = 5396.25$, minimum $\chi^2 = 1.079e+04$

Table 4.10: Estimated best-fit, mean, 1-σ uncertainty and the 2-σ intervals constraints for regime 2 in the vanilla set-up with KiDS data.

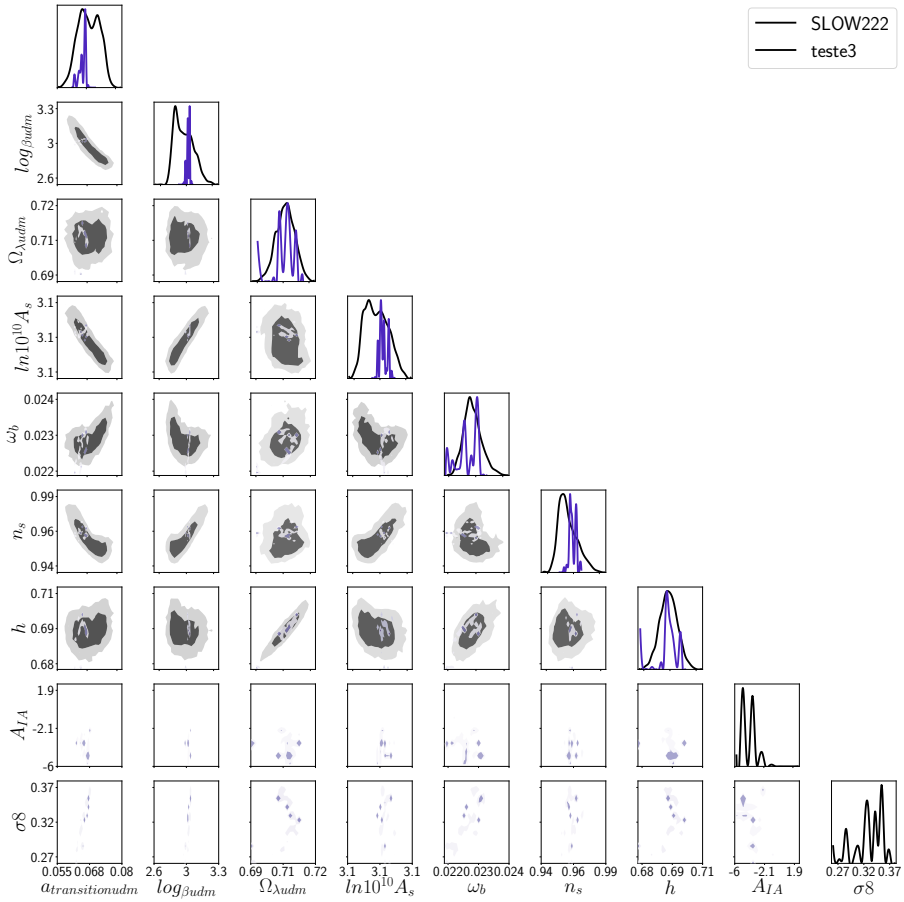

Figure 4.6: Regime 2: Posterior probabilities for each parameter in the vanilla set-up, as well as the contours with the 1-σ and 2-σ confidence regions for the analysis with (black lines) and without KiDS (blue lines).

Tables 4.9, 4.10 and Fig. 4.6 show the results of the vanilla set-up analyses. They are consistent with the minimal set-up, with no statistical results from the KiDS case. While the best-fit model no longer has a slope $n_s > 1$, indicating that this regime is more capable of forming structure than regime 1.

4.3.5 Regime 3: UDM early transition

In Tables 4.11, 4.12 and Fig. 4.7 we show the results of our analyses in this regime for the minimal set-up, while Tabs. 4.13, 4.14 and Fig. 4.8 show the results for the vanilla set-up. We can see that in this range of values for the cosmological parameters KiDS strongly constraint the values of a_t and β.

The results for the two set-ups are consistent and we can clearly see for the first time the interest in using the weak lensing data. In fact, for example in Figs. 4.7 and 4.8, we see a strong reduction in the UDM parameters contours when adding the KiDS data. In particular, the a_t distribution without weak lensing data is bimodal with the strongest peak at lower values (Fig. 4.8), while the addition of KiDS data enhances the second peak (Fig. 4.8) dramatically changing the result. Indeed, comparing the a_t results from Tab. 4.13 to Tab. 4.14 we see a strong shift in the mean value. The same happens for the β parameter where 1-σ decreases from 28% to 2% in the minimal case (Tabs. 4.11 and 4.12). The gain is smaller in the case of the UDM vanilla set-up, due to the correlations with the extra free parameters.

The parameter σ_8 has now for the first time values compatible with the known ΛCDM values [55]. Since we are adding KiDS to the Planck combination of data, we have more data points and consistently obtain stronger constraints on σ_8 in comparison with the contours obtained in [55].

We can then conclude that fast and early transition UDM models are compatible with structure formation on quasi-linear scales at low redshift.

Parameters	best-fit	mean$\pm\sigma$	95% lower	95% upper
a_t	0.01182	$0.01616^{+0.0079}_{-0.0119}$	0.00209	0.03052
$log_{\beta,udm}$	5.63	$4.631^{+1.2771}_{-1.3052}$	3.0458	5.6281
$\Omega_{\Lambda udm}$	0.6884	$0.6884^{+0.0008}_{-0.00078}$	0.6868	0.69
$ln10^{10}A_s$	3.121	$3.121^{+0.0019}_{-0.002}$	3.117	3.125

$-\ln\mathcal{L}_{\min} = 5379.71$, minimum $\chi^2 = 1.076e+04$

Table 4.11: Estimated best-fit, mean, 1-σ uncertainty and the 2-σ intervals constraints for regime 3 in the minimal set-up without KiDS data.

Parameters	best-fit	mean$\pm\sigma$	95% lower	95% upper
a_t	0.0349	$0.03614^{+0.0016}_{-0.0015}$	0.03312	0.0389
$log_{\beta,udm}$	5.639	$5.568^{+0.13}_{-0.04}$	5.378	5.7
$\Omega_{\Lambda udm}$	0.6886	$0.6883^{+0.00086}_{-0.00075}$	0.6867	0.6899
$ln10^{10}A_s$	3.121	$3.122^{+0.002}_{-0.0021}$	3.118	3.126
A_{IA}	-4.333	$-4.413^{+0.2701}_{-1.4360}$	-5.8489	-2.4071
$\sigma 8$	0.7726	$0.7703^{+0.03}_{-0.047}$	0.6967	0.8559

$-\ln\mathcal{L}_{\rm min} = 5413.66$, minimum $\chi^2 = 1.083e+04$

Table 4.12: Estimated best-fit, mean, 1-σ uncertainty and the 2-σ intervals constraints for regime 3 in the minimal set-up with KiDS data.

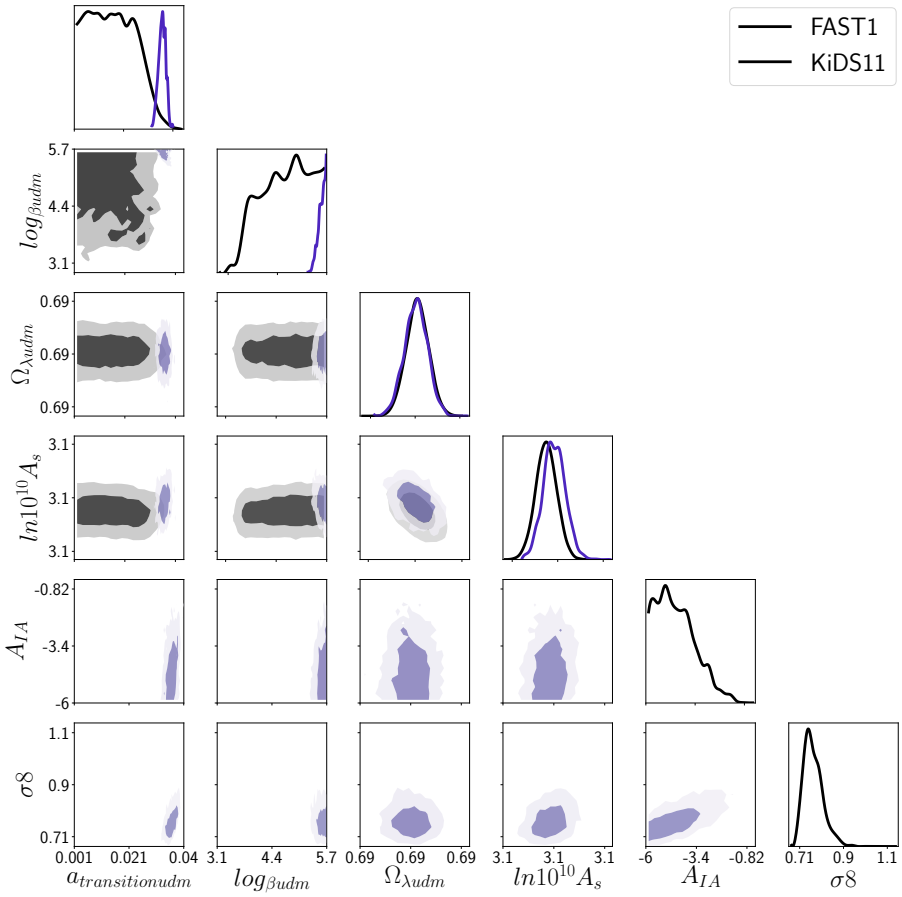

Figure 4.7: Regime 3: Posterior probabilities for each parameter in the minimal set-up, as well as the contours with the 1-σ and 2-σ confidence regions for the analysis with (black lines) and without KiDS (blue lines).

We can also look for correlations on the two-dimensional plots of Figs. 4.7 and 4.8. In comparison with the first regime we no longer have the correlation between n_s and β, and we obtain values of n_s very similar to the ones obtained for ΛCDM. We also lost the anti-correlation between $\Omega_{\Lambda udm}$ and

β. In fact we cannot conclude in this case if the correlation still exist, since the values of β are very constrained near the maximum value allowed and we cannot see if there is any correlation trend. We also do not see a correlation between β and σ_8, however a correlation is expected since the value of β is strongly correlated with the Jeans scale that will affect the matter power spectrum at the scales where σ_8 is calculated. We observe that there is new a anti-correlation between A_s and $\Omega_{\Lambda udm}$ that did not exist in the first regime. On the contrary, now a_t and σ_8 seem to have a correlation that we were unable to see in the first regime since a_t was always near its minimum value allowed. This correlation is expected since the value of a_t is also related to the Jean scale.

Finally, since our model is now sensitive to KiDS data, we get for the first time a measurement of the instrinsic alignment amplitude. In particular, we find a negative value in agreement with the values obtained in [55] for ΛCDM. We also find a correlation between the value of σ_8 and the intrinsic alignment, because the intrinsic alignment affects the amplitude of the power spectrum at the measured scales.
The negative value of A_{IA} indicates that the alignment is dominated by the cross term in Eq. 4.24 and not by the auto-correlation term.

Parameters	best-fit	mean$\pm\sigma$	95% lower	95% upper
a_t	0.005355	$0.01516^{+0.0025}_{-0.014}$	0.00213	0.04128
$log_{\beta,udm}$	5.458	$5.001^{+0.7}_{-0.21}$	4.038	5.7
$\Omega_{\Lambda udm}$	0.7088	$0.709^{+0.0056}_{-0.0053}$	0.6981	0.7198
$ln10^{10}A_s$	3.12	$3.119^{+0.0033}_{-0.0042}$	3.111	3.128
ω_b	0.02254	$0.02249^{+0.00019}_{-0.00019}$	0.0221	0.02289
n_s	0.9734	$0.9734^{+0.0037}_{-0.0049}$	0.964	0.9836
h	0.6925	$0.6924^{+0.0044}_{-0.0043}$	0.6837	0.7011

$-\ln\mathcal{L}_{\min} = 5370.78$, minimum $\chi^2 = 1.074e+04$

Table 4.13: Estimated best-fit, mean, 1-σ uncertainty and the 2-σ intervals constraints for regime 3 in the vanilla set-up without KiDS data.

Parameters	best-fit	mean$\pm\sigma$	95% lower	95% upper
a_t	0.03723	$0.03007^{+0.012}_{0.003}$	0.03356	0.04144
$log_{\beta,udm}$	5.521	$5.365^{+0.33}_{-0.046}$	4.772	5.7
$\Omega_{\Lambda udm}$	0.7084	$0.7085^{+0.0053}_{-0.0054}$	0.6978	0.719
$ln10^{10}A_s$	3.122	$3.121^{+0.0032}_{-0.0048}$	3.114	3.131
ω_b	0.02253	$0.02252^{+0.00021}_{-0.00019}$	0.02213	0.02291
n_s	0.9752	$0.9752^{+0.0043}_{-0.0054}$	0.9655	0.9855
h	0.6919	$0.6922^{+0.0042}_{-0.0044}$	0.6834	0.7008
A_{IA}	-3.673	$-3.085^{+0.3749}_{-2.6643}$	-5.7489	5.7212
$\sigma 8$	0.8336	$0.8286^{+0.067}_{-0.11}$	0.671	1.057

$-\ln\mathcal{L}_{\min} = 5406.97$, minimum $\chi^2 = 1.081e+04$

Table 4.14: Estimated best-fit, mean, 1-σ uncertainty and the 2-σ intervals constraints for regime 3 in the vanilla set-up with KiDS data.

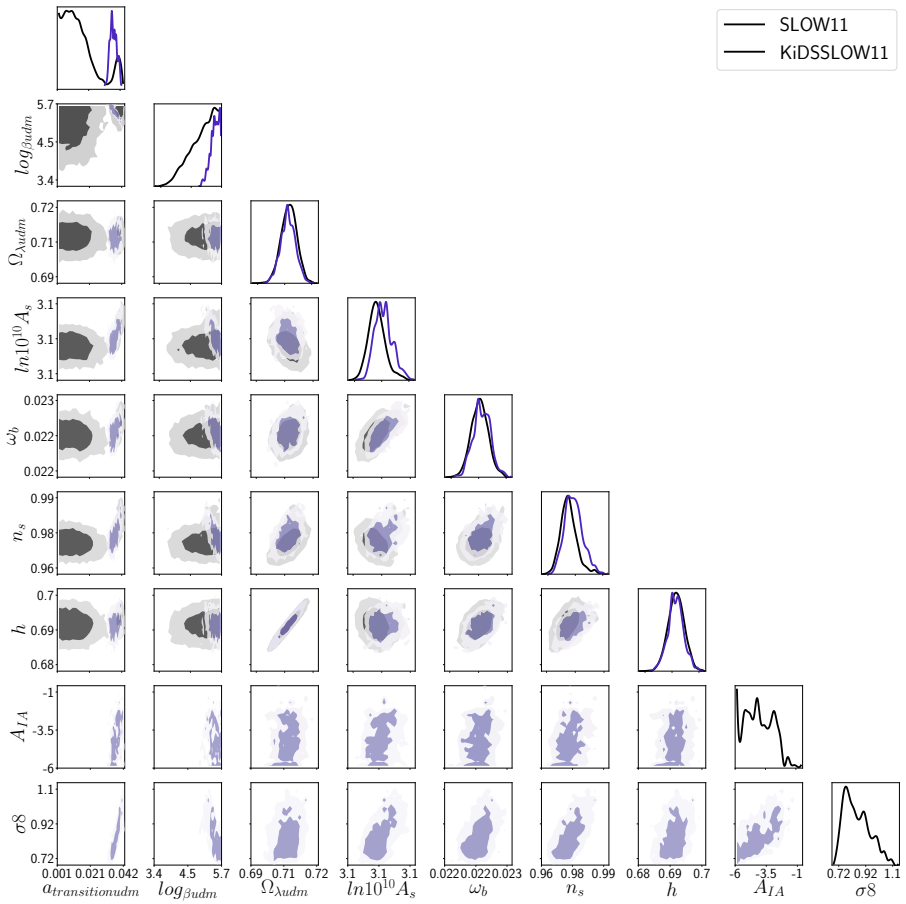

Figure 4.8: Regime 3: Posterior probabilities for each parameter in the vanilla set-up, as well as the contours with the 1-σ and 2-σ confidence regions for the analysis with (black lines) and without KiDS (blue lines).

4.3.6 Model comparison

For model comparison we made an analysis of the ΛCDM model, both in a minimal and in a vanilla set-up.
The minimal case only has two free parameters: A_s and $w_{cdm} = \Omega_{cdm}h^2$ that replaces Ω_Λ. The vanilla case has the basis five parameters (A_s, w_{cdm}, w_b, n_s, h). We produced chains with and without weak lensing data and show the results for the four cases, only in table form (see Tab. 4.15 - 4.18).

Parameters	best-fit	mean$\pm\sigma$	95% lower	95% upper
ω_{cdm}	0.1201	$0.1201^{+0.00038}_{-0.00036}$	0.1194	0.1208
$ln10^{10}A_s$	3.121	$3.121^{+0.0022}_{-0.0019}$	3.117	3.125

$-\ln\mathcal{L}_{\min} = 5379.63$, minimum $\chi^2 = 1.076e+04$

Table 4.15: Estimated best-fit, mean, 1-σ uncertainty and the 2-σ intervals constraints for ΛCDM in the minimal set-up without KiDS data.

Parameters	best-fit	mean$\pm\sigma$	95% lower	95% upper
ω_{cdm}	0.1199	$0.12^{+0.00032}_{-0.00037}$	0.1193	0.1207
$ln10^{10}A_s$	3.12	$3.121^{+0.0018}_{-0.002}$	3.117	3.124
A_{IA}	0.7002	$0.8844^{+0.3333}_{-0.3114}$	0.3114	1.6214
$\sigma 8$	0.8563	$0.8564^{+0.0019}_{-0.0022}$	0.8525	0.8606

$-\ln\mathcal{L}_{\min} = 5412.43$, minimum $\chi^2 = 1.082e+04$

Table 4.16: Estimated best-fit, mean, 1-σ uncertainty and the 2-σ intervals constraints for ΛCDM in the minimal set-up with KiDS data.

Parameters	best-fit	mean$\pm\sigma$	95% lower	95% upper
ω_{cdm}	0.1169	$0.1169^{+0.001}_{-0.0011}$	0.1148	0.119
$ln10^{10}A_s$	3.119	$3.119^{+0.0033}_{-0.0022}$	3.1128	3.1253
ω_b	0.02249	$0.02252^{+0.00019}_{-0.00018}$	0.02215	0.02289
n_s	0.973	$0.9733^{+0.0037}_{-0.0041}$	0.9656	0.9816
h	0.6926	$0.6929^{+0.0044}_{-0.0045}$	0.6841	0.7019

$-\ln\mathcal{L}_{\min} = 5370.54$, minimum $\chi^2 = 1.074e+04$

Table 4.17: Estimated best-fit, mean, 1-σ uncertainty and the 2-σ intervals constraints for ΛCDM in the vanilla set-up without KiDS data.

Parameters	best-fit	mean$\pm\sigma$	95% lower	95% upper
ω_{cdm}	0.117	$0.1168^{+0.001}_{-0.0011}$	0.1146	0.119
$ln10^{10}A_s$	3.119	$3.119^{+0.0042}_{-0.0041}$	3.11	3.127
ω_b	0.02252	$0.02251^{+0.00017}_{-0.00021}$	0.02215	0.02294
n_s	0.9737	$0.9735^{+0.0044}_{-0.0041}$	0.9649	0.982
h	0.6929	$0.6934^{+0.0047}_{-0.0045}$	0.6843	0.7026
A_{IA}	-0.9944	$-0.8434^{+0.69}_{-0.77}$	-2.239	0.6273
$\sigma 8$	0.8475	$0.8465^{+0.0041}_{-0.0043}$	0.838	0.8552

$-\ln\mathcal{L}_{\min} = 5394.00$, minimum $\chi^2 = 1.079e+04$

Table 4.18: Estimated best-fit, mean, 1-σ uncertainty and the 2-σ intervals constraints for ΛCDM in the vanilla set-up with KiDS data.

We start by comparing the best-fit values for each case with ΛCDM (Tab. 4.19). We confirm that regime 1, that we already ruled out, is very different from the ΛCDM values. The other cases, specially UDM_3, have similar best-fit values for the standard models as ΛCDM.

Parameters	ΛCDM (no KiDS/KiDS)	UDM_1 (no KiDS/KiDS)	UDM_2 (no KiDS/KiDS)	UDM_3 (no KiDS/KiDS)
h	0.6926/0.6929	0.6439/0.6449	0.6953/0.6930	0.6925/0.695
$ln10^{10}A_s$	3.119/3.119	3.056/3.056	3.092/3.102	3.120/3.119
ω_b	0.02249/0.02252	0.0200/0.0201	0.02290/0.02237	0.02254/0.02246
n_s	0.973/0.9737	1.048/1.044	0.951/0.9592	0.9734/0.9749
$\Omega_{\Lambda udm}$ / Ω_Λ	0.7094/0.7094	0.6536/0.6557	0.7105/0.7095	0.7088/0.7123
A_{IA}	$--/-0.9944$	$--/-3.163$	$--/-4.584$	$--/-4.632$
χ^2	5370.54/5394.00	5537.99/5600.97	5378.17/5396.25	5370.78/5407.85

Table 4.19: Best-fit values for ΛCDM and the three regimes of the UDM model, with and without KiDS.

We took the matter power spectrum of the best-fit UDM_3 model obtained from the analysis without KiDS and computed its σ_8 value. We found $\sigma_8 = 0.8218$. Comparing with the result obtained from the analysis with KiDS ($\sigma_8 = 0.8063$) we expect a similar tension between the predicted values of σ_8 from Planck and KiDS as in ΛCDM.

We also compute a number of information criteria to make a quantitative model comparison with ΛCDM. These criteria are the Bayesian information criteria (BIC), defined as [70, 71]

$$\mathrm{BIC} = -2\ln \mathrm{L}_{\max} + k\ln N\,, \tag{4.27}$$

the Deviance information criteria (DIC), following [72]

$$\mathrm{DIC} = 2\langle\chi^2\rangle - \chi^2_{min}\,, \tag{4.28}$$

and the Akaike information criteria (AIC) [70]

$$\mathrm{AIC} = 2k - 2\ln \mathrm{L}_{\max}. \tag{4.29}$$

These criteria depend on the best-fit χ^2, mean χ^2 over the sample, number of model parameters k and number of data points N. In general, a large number of model parameters penalises the model. So a model with more parameters needs to have a better best-fit in order to be favoured in these comparisons.
Tables 4.20 - 4.22 show the values found for the three criteria, plus the best-fit χ^2 and reduced χ^2 for the four models in the two set-ups and the two combinations of data.

	ΛCDM	UDM_1	UDM_2	UDM_3
χ^2	5379.63	5668.45	5386.33	5379.71
$\chi^2_{\rm red}$	0.92960	0.97951	0.93076	0.92962
BIC	5396.95	5703.10	5420.98	5414.36
DIC	5381.66	5673.32	5390.95	5382.83
AIC	5383.63	5676.45	5394.33	5387.71

Table 4.20: Values from five model comparison quantities, for the minimal no-KiDS case.

	ΛCDM	UDM_1	UDM_2	UDM_3
χ^2	5412.43	5731.30	5432.23	5413.66
$\chi^2_{\rm red}$	0.93366	0.98867	0.93708	0.93387
BIC	5438.42	5774.62	5475.55	5456.98
DIC	5419.27	5739.46	−−	5422.48
AIC	5418.43	5741.30	5442.23	5423.66

Table 4.21: Values from five model comparison quantities, for the minimal with-KiDS case.

	ΛCDM	UDM_1	UDM_2	UDM_3
χ^2	5370.54	5537.99	5378.17	5370.78
$\chi^2_{\rm red}$	0.92804	0.95697	0.92936	0.92808
BIC	5413.85	5598.63	5438.81	5431.42
DIC	5375.60	5545.05	5384.63	5377.02
AIC	5380.54	5551.99	5392.17	5384.78

Table 4.22: Values from five model comparison quantities, for the vanilla no-KiDS case.

	ΛCDM	UDM_1	UDM_2	UDM_3
χ^2	5394.00	5600.97	5396.25	5406.97
$\chi^2_{\rm red}$	0.93048	0.96618	0.93087	0.93272
BIC	5445.99	5670.28	5465.56	5476.28
DIC	5400.18	5611.19	−−	5430.04
AIC	5406.00	5616.97	5412.25	5422.97

Table 4.23: Values from five model comparison quantities, for the vanilla with-KiDS case.

We find that the best-fit χ^2 of UDM_3 is slightly worse than ΛCDM. However, due to the larger number of model parameters, there is a stronger preference for ΛCDM from all information criteria and in all scenarios there is and indication that including KiDS data disfavours the UDM model even more. For the vanilla case, we obtain the same trend except for the second regime, where there is a decrease in the difference between the BIC result for ΛCDM and for UDM_2 when we include the KiDS data. This may suggest that for this regime the UDM model may be a better fit to this probe than ΛCDM. This inconclusive result is a strong motivation to study in more detail the second regime and proceed into a further and strong analysis in the future.

Chapter 5

Conclusions

This dissertation allowed me to learn the full procedure of how to test a cosmological model. Starting from learning a new cosmological model allowed me to study the problems related to ΛCDM and GR and gain a broader view of several proposed solutions. Then studying the theoretical details of the model gave me the opportunity to understand in more detail the evolution of scalar perturbations, how structure is formed and how it depends on a cosmological model. Then I was able to master a Boltzmann code (CLASS) which involved a review of the C programming language. Having modified the code, I was in a position to solve the equations of perturbations for this specific model. For the future, this will be an important expertise that will give me the chance to work on new models and new observables, such as solving the tensor modes of perturbation and extracting the gravitational waves predicted from a cosmological model. This dissertation also allowed me to explore the world of parameter estimation and gain expertise in an MCMC code, which makes a bridge between the theoretical quantities obtained from CLASS and the observable data.
Finally, I learnt many details about various cosmological data, using the likelihood codes of each dataset.

The analysis made in this dissertation leads to the conclusion that this UDM model is a viable cosmological model, compatible with the structure formation data used.
As in all scientific analysis, we made several assumptions and verifications that are important to keep in mind.
First of all, we verified that the large oscillations produced for some parameters values were real and not a numerical artefact. To verify this, we used a different numerical integrator and considered different approximations to the Heaviside function.
The oscillations impede to properly compute a non-linear scale in the standard way. In addition there is no non-linear prescription developed specifically for UDM models. For these reasons, we decided to keep only the linear or quasi-linear data points from the weak lensing dataset. The points kept from the various cosmic shear power spectrum at various redshift bins probe the scale range $k = [0.28, 0.82]$ of the matter power spectrum. By using these data points in two different ΛCDM analysis (with and without making the Halofit non-linear correction) we verified that the error in the likelihood is of order 10 %.
Another assumption, was to divide the n-dimension parameter space in three separate regimes, in order to discard the volume where most of the models produced a sound speed larger than one and reach convergence faster. This division granted us to study three specific cases of the model: one where the matter power spectrum strongly decreases at small scales, suppressing structure formation; a case where

the scales that we used to test against KiDS are in a strong oscillatory regime, giving regions of the space parameter with very good results next to regions of the space parameter with bad results; and a third case where the oscillations of the matter power spectrum only appears on very small scales and allow structure formation. In the first and third regime, due to the smoothness of the matter power spectrum in the tested regions the chains were able to converge. In the second regime we were not able to made a complete analysis, but we were able to find UDM models with good agreement with the observations. To obtain results for the second case we expect in the future to divide this space parameter in more parts or preferentially use a different sampling method that can better account for multiple likelihood peaks than the MCMC, such as the Nested Sampling.

We also performed the same analysis for ΛCDM without the HALOFIT non-linear corrections and from the comparison between our UDM model and ΛCDM we could conclude that our model is still a strong candidate and a model capable of forming structure. However, a strong preference for the ΛCDM model still remains.

There are several ways in which we could try to improve our analysis in future work. Besides the improvement in the statistical analysis, in particular for the second case, we may also improve the theoretical matter power spectrum by including the non-linear corrections. This will pass by being able to implement the HALOFIT or other non-linear correction to our UDM model. This will be mandatory to use if we want to test this model with the future data from the Euclid space mission.

We may also consider a different approach to the treatment of the UDM perturbations. In this dissertation we always performed a standard procedure to deal with the linear perturbation and then apply, when possible, non-linear corrections that start to appear at late times. However, in future works this method may also be revisited and we should check if a new approach for the case of models with large oscillations in the density contrast must be considered. This is because large oscillations can produce, in some scale, a large amplitude in the density contrast giving rise to a non-linear regime much earlier in time. Then, the linear density contrast goes down again as it oscillates and the power spectrum today is linear at that scale. However, we might consider that linear evolution is no longer valid from the time of the oscillation peak, and from this time onwards that scale could be removed from the linear evolution, and this effect could backreact on the evolution of the other scales.
The oscillations are indeed caused by the variation of the sound speed. As a test, we fix the sound speed to zero in the perturbation module of CLASS and we were able to obtain a matter power spectrum with no oscillations. This give rises to possible ideas that allow the model to be well behaved and remove the large oscillations obtained. One option might be to construct a lagrangian for this model, where we obtain a more generalised fluid, or even just consider the fluid to be non-adiabatic. This will introduce a new degree of freedom, related to the fact that the variation of pressure now has a dependency on the entropy, allowing us to fix the sound speed and reduce the oscillations. These new approaches usually give rise to new degrees of freedom that will penalise the model according to the information criteria used in Sec. 4.6. However, it is important to consider all possible variations of a model that are realist and physically allowed. A model should not be ignored just because it requires more degrees of freedom. It could turn out to be the true description of the Universe.

Another possibility is to continue working with this model as it is, but considering the backreaction effect discussed in Sec. 2.3. This backreaction was already implemented in CLASS for the GCG and

based on the results obtained for the GCG (see Appendix A) it might have a strong influence in the matter power spectrum of the UDM model.

Therefore, there are may aspects of the UDM models that may be refined and many variations that are worth exploring, motivated by our results that these models are still viable given current structure formation data.

Appendices

Appendix A

Results for the GCG

In this appendix, we show results from our implementation of the generalised Chaplygin gas (GCG), introduced in Section 2.2. The main goal of implementing this model was to compare our results with published ones.
The comparison was successful, and we may now also discuss some of the models' features.

In Figs. A.1 and A.2 we show the density contrast obtained when using the GCG for two different scales. Just like in Fig. 3.30, there is a much smoother pattern in the oscillations compared with the UDM model with fast transition. These oscillations, as shown in Fig. A.3 also result in a matter power spectrum with some oscillations.

We also considered the backreaction of the collapsed regions on the evolution of the linear density contrast, as described in Section 2.3. The evolution of the two components, δ_+ and δ_- is shown in Fig. A.4, A.5, A.6 for three different scales, together with the evolution of δ_{cdm} in a flat ΛCDM model.

We see that δ_+, the density contrast of the collapsed regions, grows as CDM while δ_- behaves as in the standard GCG model. The presence of the collapsed regions smooths out the oscillations in the final matter power spectrum, as shown in Fig. A.7.
This is a very interesting case and we have already implemented this approach for the UDM model for future analyses.

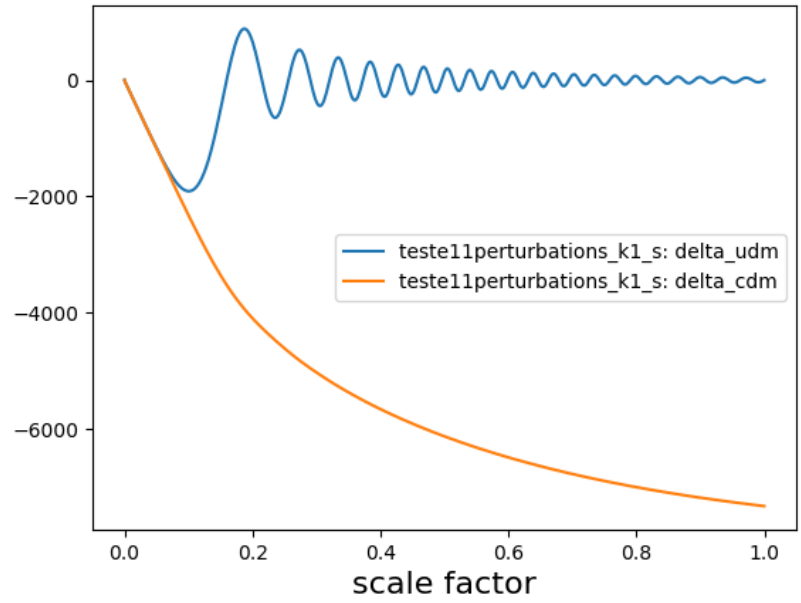

Figure A.1: Evolution of δ_{GCG} and δ_{cdm} over time for the intermediate scale $k = 0.1$, for $A_{chap} = 0.72$ and $\alpha = 0.2$.

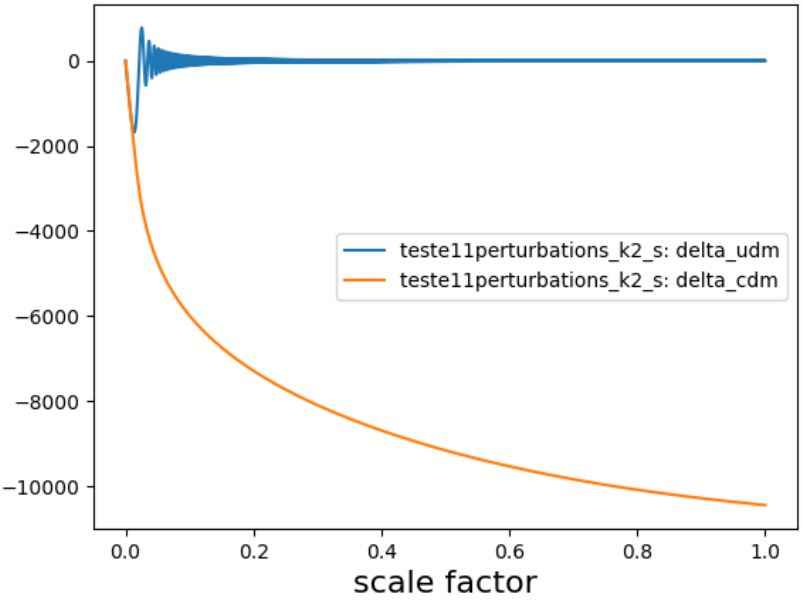

Figure A.2: Evolution of δ_{GCG} and δ_{cdm} over time for the small scale $k = 10$, for $A_{chap} = 0.72$ and $\alpha = 0.2$.

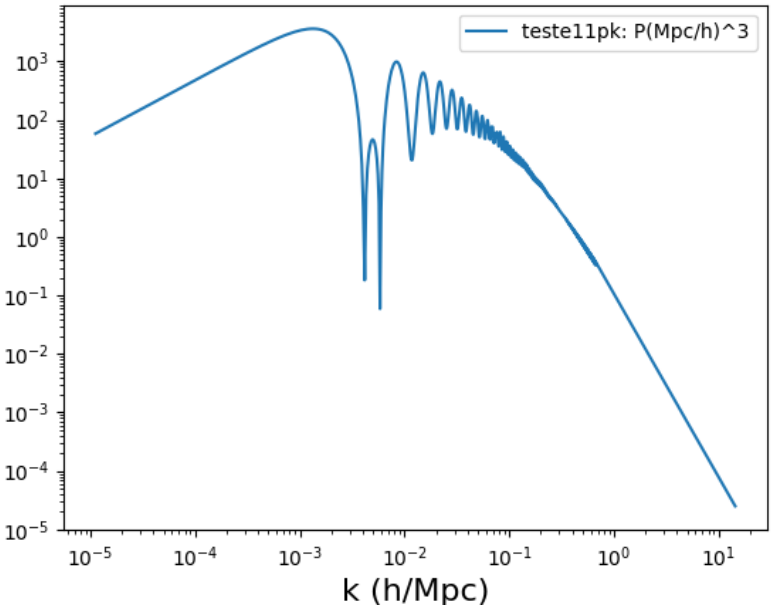

Figure A.3: Matter power spectrum for $A_{chap} = 0.72$ and $\alpha = 0.2$.

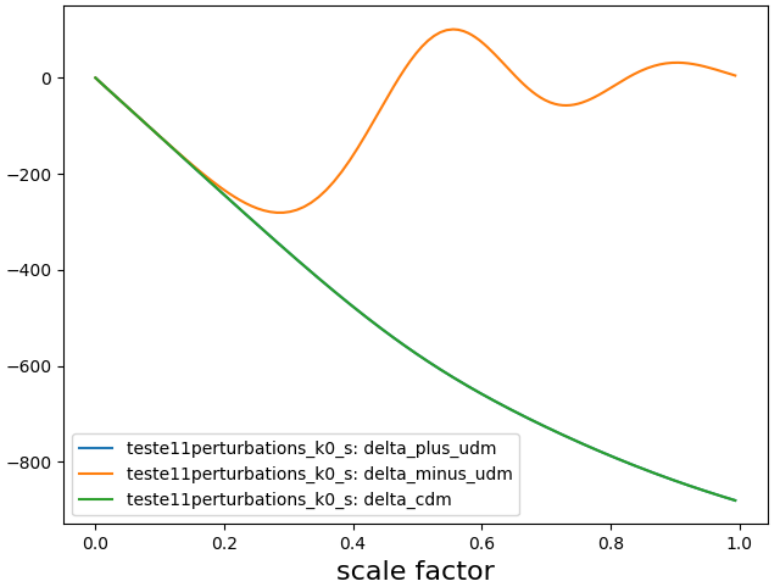

Figure A.4: Evolution of $\delta_{+,GCG}$, $\delta_{-,GCG}$ and δ_{cdm} over time for the large scale $k = 0.01$, for $A_{chap} = 0.72$, $\alpha = 0.2$ and using a backreaction parameter $\epsilon_i = 0.4$.

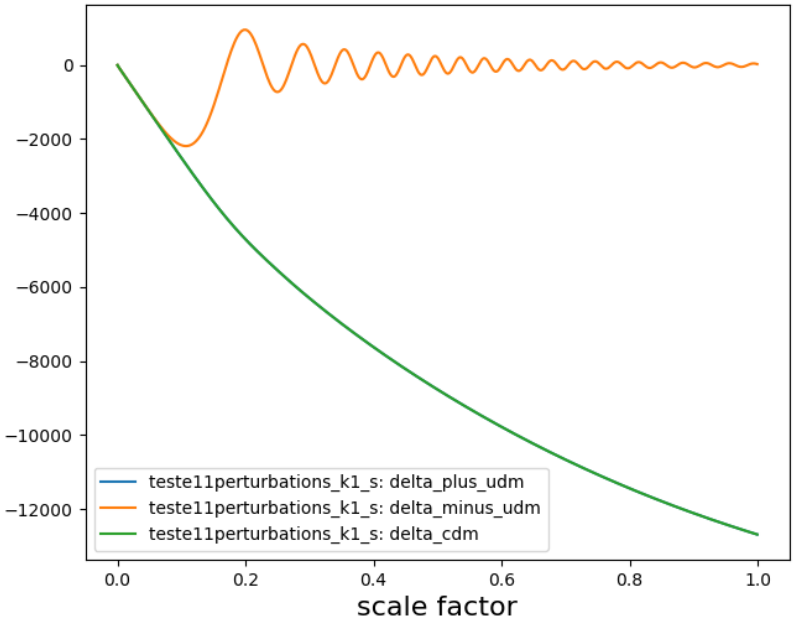

Figure A.5: Evolution of $\delta_{+,GCG}$, $\delta_{-,GCG}$ and δ_{cdm} over time for the intermediate scale $k = 0.1$, for $A_{chap} = 0.72$, $\alpha = 0.2$ and using a backreaction parameter $\epsilon_i = 0.4$.

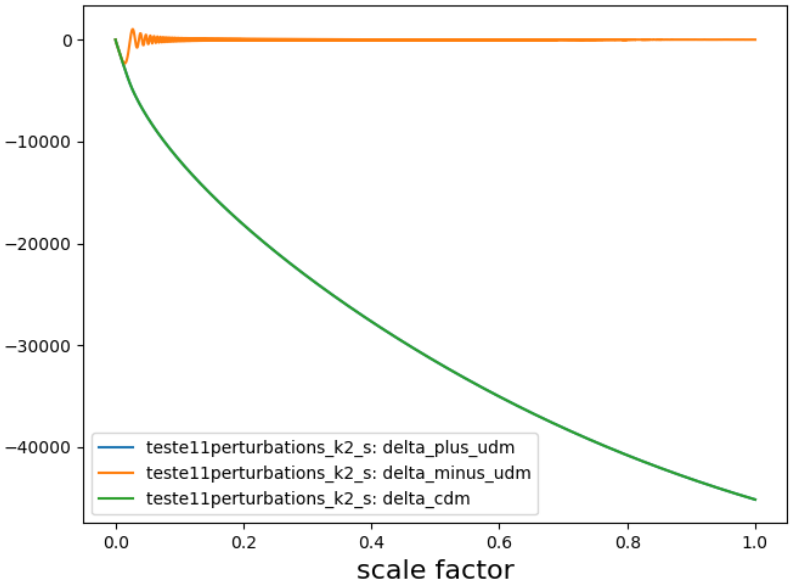

Figure A.6: Evolution of $\delta_{+,GCG}$, $\delta_{-,GCG}$ and δ_{cdm} over time for the small scale $k = 10$, for $A_{chap} = 0.72$, $\alpha = 0.2$ and using a backreaction parameter $\epsilon_i = 0.4$.

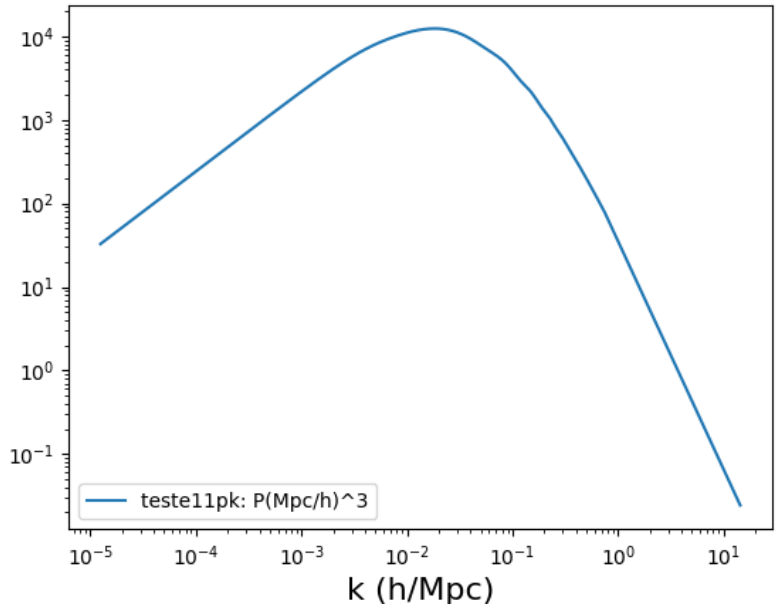

Figure A.7: Matter power spectrum for $A_{chap} = 0.72$, $\alpha = 0.2$ and using a backreaction parameter $\epsilon_i = 0.4$.

Appendix B

Continuous approximations to the Heaviside function

In order to investigate that the large oscillations were not a numerical artifact, we decided to use different continuous approximations to the Heaviside step function.
We considered various popular S-shaped curves, also called sigmoid curves.

First attempt

$$H(a - a_t) = \frac{1}{2}\left[1 + \times tanh\left(\beta\left(a - a_t\right)\right)\right]. \tag{B.1}$$

We started by considering the well-known logistic function.
This attempt was unsuccessful since this approximation gives a negative speed of sound for a certain period of time, as seen in Fig. B.1.

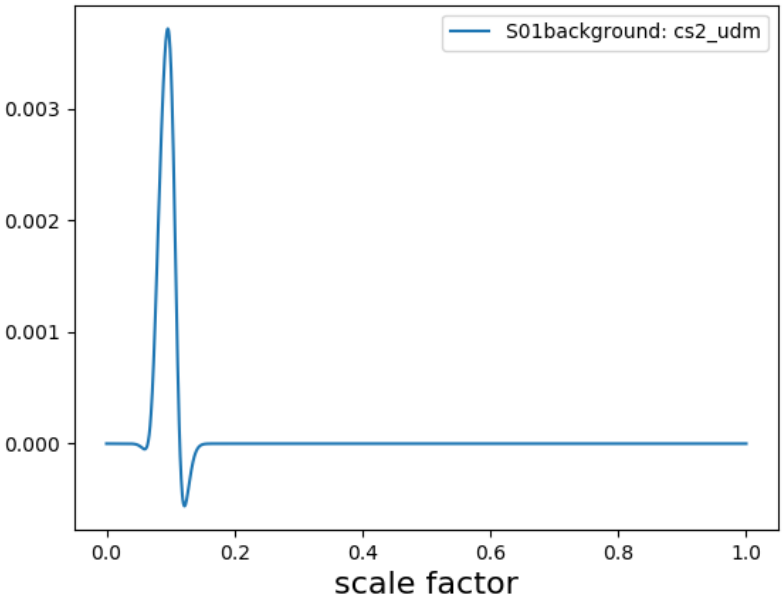

Figure B.1: Speed of sound for the first attempt, with $a_t = 0.01$, $\Omega_{\Lambda udm} = 0.7$ and $\beta = 500$.

This result in a exponential growth of the density contrast for the fluid, and therefore, for the matter power spectrum, shown in Fig. B.2. This results is of course not found in the observed universe.

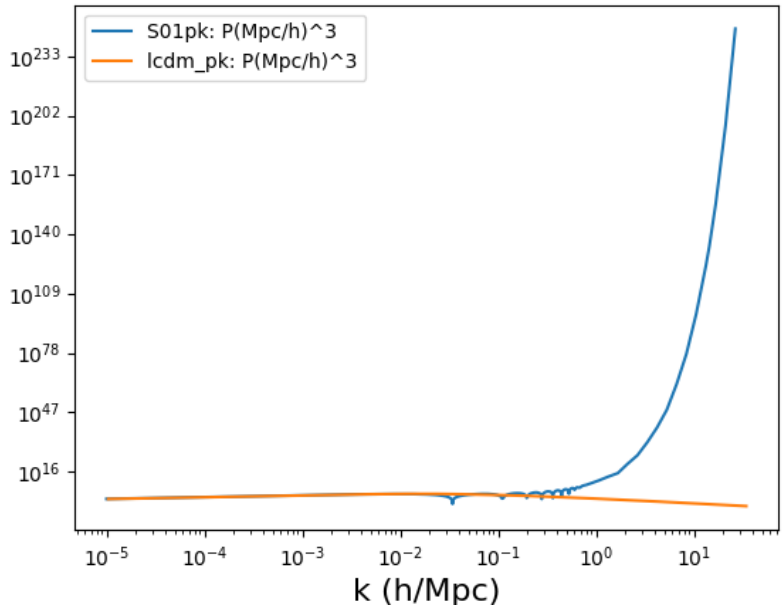

Figure B.2: Matter power spectrum for the first attempt with $a_t = 0.01$, $\Omega_{\Lambda udm} = 0.7$ and $\beta = 500$.

Second attempt

$$H(a-a_t) = \frac{1}{2}\left[1 + \frac{\beta\,(a-a_t)}{\left(1+\beta^2\,(a-a_t)^2\right)^{1/2}}\right]. \tag{B.2}$$

In this attempt we obtained the same result as in the previous one, finding again a negative sound speed, as shown in Fig. B.1.

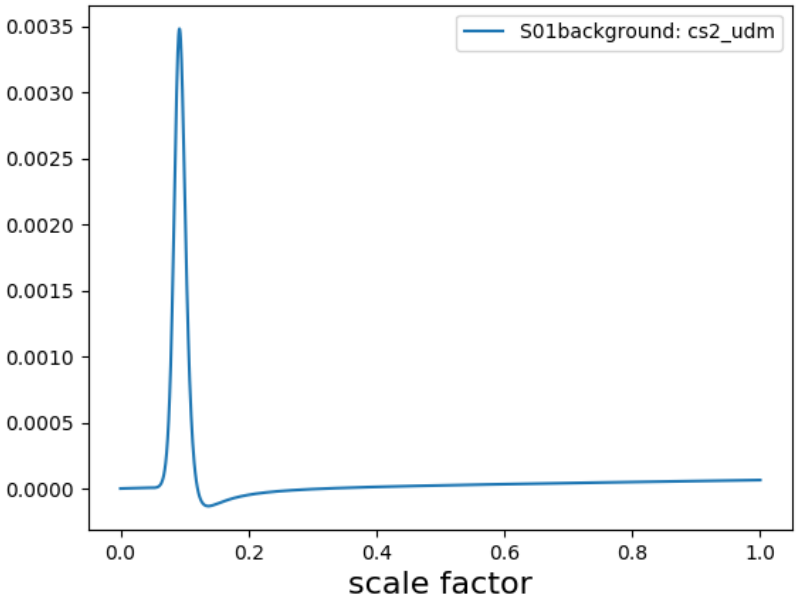

Figure B.3: Speed of sound for the second attempt, with $a_t = 0.01$, $\Omega_{\Lambda udm} = 0.7$ and $\beta = 500$.

Third attempt

$$H(a-a_t) = \frac{1}{2}\left[1 + \frac{\beta\,(a-a_t)}{1+\beta|a-a_t|}\right]. \tag{B.3}$$

With this approximation we were not even able to compute any good result.

Fourth attempt

$$H(a-a_t) = \frac{2}{\pi} atan\left(exp\left(\beta\,(a-a_t)\right)\right). \tag{B.4}$$

This function is similar to the one used in our UDM model. It only differs in having an exponential in the argument of arctan. It turns out to be an interesting viable function that may deserve further consideration in future works.
Its main interesting feature is that it produces a sound speed that remains null after the peak the at transition (see Fig. B.4) This is not always the case for the original function, where the sound speed slowly increases from zero after the peak. This new feature allows for a very smooth matter spectrum,

as shown in Fig. B.5, even though large oscillations are still formed for models with later transitions, as shown in Fig. B.6

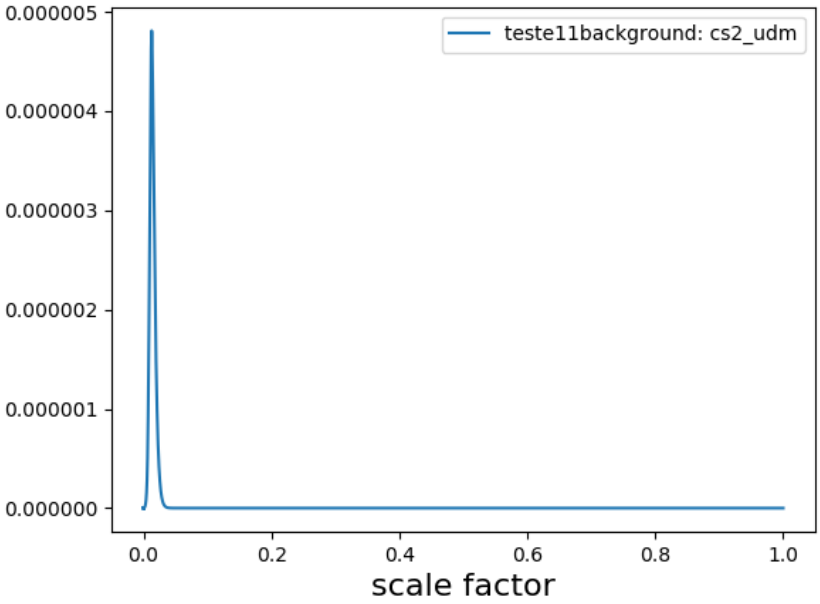

Figure B.4: Speed of sound for the fourth attempt, with $a_t = 0.01$, $\Omega_{\Lambda udm} = 0.7$ and $\beta = 500$.

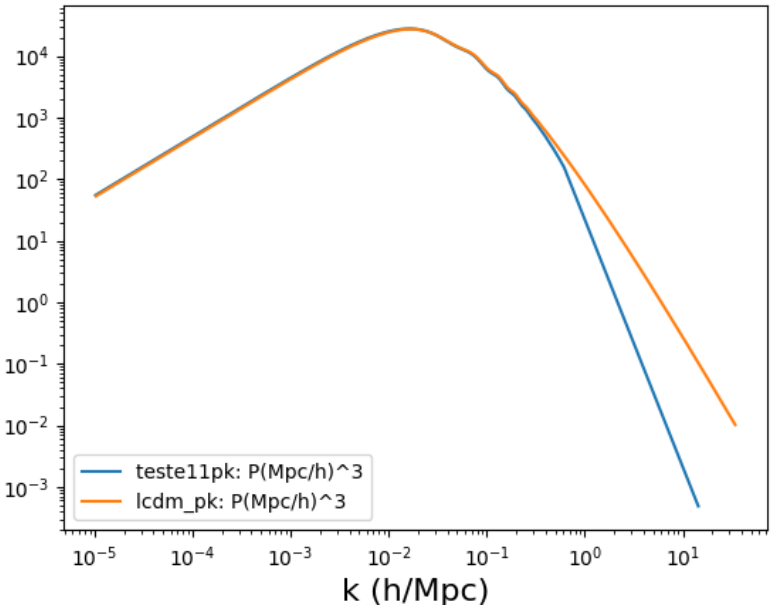

Figure B.5: Matter power spectrum for the fourth attempt with $a_t = 0.01$, $\Omega_{\Lambda udm} = 0.7$ and $\beta = 500$.

However, for higher values of a_t what could be a numerical problem remains:

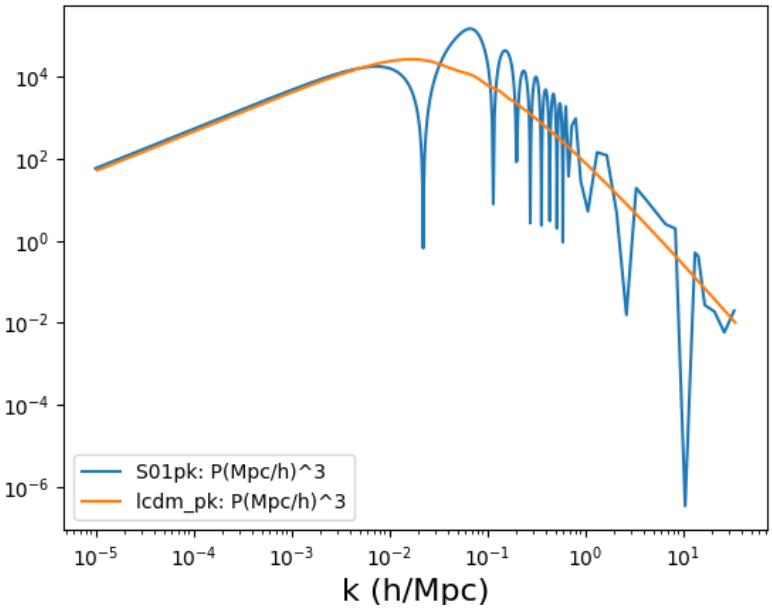

Figure B.6: Matter power spectrum for the fourth attempt with $a_t = 0.09$, $\Omega_{\Lambda udm} = 0.7$ and $\beta = 500$.

Discussion

After testing these new functions it has become clearer that an approximation to the Heaviside function is not only a mathematical device to connect the two regimes of the UDM model, but it contains a lot of physics in it. This is related to the fact that even if these functions have exactly the same shape, its derivatives are not the same, resulting in different evolutions for the equation of state and the sound speed. A different function consequently represents a new model, with different characteristics.
We also found no evidences for numerical issues in our CLASS implementation.

Bibliography

[1] Amendola L., Tsujikawa S., *Dark Energy* (Book), Cambridge University Press (2010).

[2] Baumann D. *Cosmology: Part III Mathematical Tripos* (Lecture)

[3] Lifshitz E. M. *Republication of: On the gravitational stability of the expanding universe*, J. Phys. (USSR) 10 116 (1946)

[4] Carroll S. *Spacetime and Geometry: An Introduction to General Relativity* (Book), Pearson (2003).

[5] Bartelmann M. *Cosmology* (Lecture), Institut fur Theoretische Astrophysik Universitat Heidelberg.

[6] Planck Collaboration *Planck 2015 results. XIII. Cosmological parameters*, Astron.Astrophys. 594 A13 (2016).

[7] Chung-Pei Ma, Bertschinger E. *Cosmological Perturbation Theory in the Synchronous and Conformal Newtonian Gauges*, Astrophys.J. 455 7-25 (1995).

[8] W. H. Press and Vishniac, E. T. Ap. J.,239, 1. (1980)

[9] Yoo J., Watanabe Y. *Theoretical Models of Dark Energy*, Int.J.Mod.Phys. D21 1230002 (2012).

[10] Supernova Search Team Collaboration, Riess A. G. et. al. *Type Ia supernova discoveries at $z > 1$ from the Hubble Space Telescope: Evidence for past deceleration and constraints on dark energy evolution*, Astrophys.J. 607 665-687 (2004).

[11] SDSS Collaboration, Eisenstein D. J. et. al. *Detection of the baryon acoustic peak in the large-scale correlation function of SDSS luminous red galaxies*, Astrophys.J. 633 560-574 (2005).

[12] Wetterich C. *Cosmology and the Fate of Dilatation Symmetry*, Nucl.Phys. B302 668 (1988).

[13] Ratra B. and Peebles P. *Cosmological Consequences of a Rolling Homogeneous Scalar Field*, Phys.Rev. D37 3406 (1988).

[14] Caldwell R., Dave R. and Steinhardt P. J. *Cosmological imprint of an energy component with general equation of state*, Phys.Rev.Lett. 80 1582-1585 (1998).

[15] Zlatev I., Wang L.M. and Steinhardt P. J., *Quintessence, cosmic coincidence, and the cosmological constant*, Phys.Rev.Lett. 82 896-899 (1999).

[16] Caldwell R. and Linder E. V. *The Limits of quintessence*, Phys.Rev.Lett. 95 141301 (2005).

[17] Armendariz-Picon C., Mukhanov V. F. and Steinhardt P. J. *A Dynamical solution to the problem of a small cosmological constant and late time cosmic acceleration*, Phys.Rev.Lett. 85 4438-4441 (2000).

[18] Armendariz-Picon C., Mukhanov V. F. and Steinhardt P. J. *Essentials of k-essence*, Phys.Rev. D63 103510 (2001).

[19] Wetterich C. *The Cosmon model for an asymptotically vanishing time dependent cosmological 'constant'*, Astron.Astrophys. 301 321-328 (1995).

[20] Amendola L., *Coupled quintessence*, Phys.Rev. D62 043511 (2000).

[21] Capozziello S., Carloni S. and Troisi A. *Quintessence without scalar fields*, Recent Res.Dev.Astron.Astrophys. 1 625 (2003).

[22] Carroll S. M., Duvvuri V., Trodden M. and Turner M. S. *Is cosmic speed - up due to new gravitational physics?*, Phys.Rev. D70 043528 (2004).

[23] Nojiri S., Odintsov S., *Unified cosmic history in modified gravity: From F(R) theory to Lorentz non-invariant models*, D., Phys.Rept., 505,59 (2011).

[24] Dvali G., Gabadadze G. and Porrati M. *4-D gravity on a brane in 5-D Minkowski space*, Phys.Lett. B485 208-214 (2000).

[25] Deffayet C. *Cosmology on a brane in Minkowski bulk*, Phys.Lett. B502 199-208 (2001).

[26] Tomita K. *A local void and the accelerating universe*, Mon.Not.Roy.Astron.Soc. 326 287 (2001).

[27] Alnes H., Amarzguioui M. and Gron O. *An inhomogeneous alternative to dark energy?*, Phys.Rev. D73 083519 (2006).

[28] Kamenshchik A. Y., Moschella U. and Pasquier V. *An Alternative to quintessence*, Phys.Lett. B511 265-268 (2001).

[29] Bento M., Bertolami O. and SenA. *Generalized Chaplygin gas, accelerated expansion and dark energy matter unifcation*, Phys.Rev. D66 043507 (2002).

[30] Sandvik H., Tegmark M., Zaldarriaga M. and Waga I. *The end of unified dark matter?*, Phys.Rev. D69 123524 (2004).

[31] Amendola L., Waga I. *Observational constraints on silent quartessence*, JCAP 0511 009 (2005).

[32] Kumar S., Sen A.A. *Clustering GCG: a viable option for unified dark matter-dark energy?*, JCAP 10, 036 (2014).

[33] Avelino P.P., Bolejko K., Lewis G.F. *Nonlinear Chaplygin Gas Cosmologies*, Phys.Rev. D89 no.10, 103004 (2014).

[34] Wang Y., Wands D., Xu L., De-Santiago J., Hojjati A. *Cosmological constraints on a decomposed Chaplygin gas*, Phys. Rev. D 87, 083503 (2013).

[35] Wands D., De-Santiago J., Wang Y. *Inhomogeneous vacuum energy*, Class. Quantum Grav. 29,145017 (2012).

[36] De-Santiago J., Wands D., Wang Y. *Inhomogeneous and interacting vacuum energy*, Proceedings of 4th International Meeting on Gravitation and Cosmology (MGC 4), p.183-196 (2014).

[37] Scherrer R. J. *Purely kinetic k-essence as unified dark matter*, Phys.Rev.Lett. 93 011301 (2004).

[38] Piattella O.F., Bertacca D. *Gravitational potential evolution in Unified Dark Matter Scalar Field Cosmologies: an analytical approach*, Mod.Phys.Lett. A26 2277-2286 (2011).

[39] Piattella O.F., Bertacca D., Bruni M., Pietrobon D. *Unified Dark Matter models with fast transition*, JCAP 1001 014 (2010).

[40] Bertacca D., Bruni M., Piattella O.F., Pietrobon D. *Unified Dark Matter scalar field models with fast transition*, JCAP 1102 018 (2011).

[41] Bruni M., Lazkoz R. and Rozas-Fernández A. *Phenomenological models for Unified Dark Matter with fast transition*, Mon. Not. R. Astron. Soc.431,2907 (2013).

[42] Camera S., Kitching T. D., Heavens A. F., Bertacca D., Diaferio A. *Measuring Unified Dark Matter with 3D cosmic shear*, Mon.Not.Roy.Astron.Soc. 415 399-409 (2011).

[43] Mukhanov V. *Physical Foundations of Cosmology*, (Book) Cambridge University Press (2005).

[44] Ferreira V., *Unified Models of Dark Energy and Dark Matter* (Master Dissertation), Universidade do Porto (2014).

[45] Nadkarni-Ghosh S., Refregier A. *The Einstein-Boltzmann equations revisited*, Mon. Not. Roy. Astron. Soc. 471 2391 (2017).

[46] Lesgourgues J. *The Cosmic Linear Anisotropy Solving System (CLASS) I: Overview*, CERN-PH-TH/2011-081, LAPTH-009/11 (2011).

[47] Seljak U., Zaldarriaga M. *A Line of Sight Approach to Cosmic Microwave Background Anisotropies*, Astrophys.J.469:437-444 (1996).

[48] Lewis A., Challinor A., Lasenby A. *Efficient Computation of CMB anisotropies in closed FRW models*, Astrophys.J.538:473-476 (2000).

[49] Doran M. *CMBEASY:: an Object Oriented Code for the Cosmic Microwave Background*, JCAP 0510 011 (2005).

[50] Blas D., Lesgourgues J., Tram T. *The Cosmic Linear Anisotropy Solving System (CLASS)II: Approximation schemes*, arXiv:1104.2933 [astro-ph.CO] (2011).

[51] Lazkoz R., Leanizbarrutia I.,and Salzano V. *Cosmological constrains on fast transition Unified Dark Energy/Matter models* , PRD93,043537 (2016).

[52] Bartelmann M., Schneider P. *Weak gravitational lensing* , Phys.Rept. 340 291-472 (2001).

[53] The Virgo Consortium, Smith R.E., Peacock J.A., Jenkins A., White S.D.M., Frenk C.S., Pearce F.R., Thomas P.A., Efstathiou G.,Couchmann H.M.P. *Stable clustering, the halo model and nonlinear cosmological power spectra*, Mon.Not.Roy.Astron.Soc.341:1311 (2003).

[54] Hildebrandt H., Viola M., Heymans C., Joudaki S., Kuijken K., Blake C., Erben T., Joachimi B., Klaes D., Miller L. et al. *KiDS-450: Cosmological parameter constraints from tomographic weak gravitational lensing*, Mon.Not.Roy.Astron.Soc. 465 1454 (2017).

[55] Köhlinger F., Viola M., Joachimi B., Hoekstra H., Van Uitert E., Hildebrandt H., Choi A., Erben T., Heymans C., Joudaki S. et al. *KiDS-450: The tomographic weak lensing power spectrum and constraints on cosmological parameters*, arXiv:1706.02892 [astro-ph.CO] (2017).

[56] Audren B., Lesgourgues J., Benabed K., Prunet S. *Conservative Constraints on Early Cosmology: an illustration of the Monte Python cosmological parameter inference code*, JCAP 1302 001 (2013).

[57] Lewis A., Bridle S. *Cosmological parameters from CMB and other data: A Monte Carlo approach*, Phys.Rev. D66 103511 (2002).

[58] Feroz F., Hobson M.P. *Multimodal nested sampling: an efficient and robust alternative to MCMC methods for astronomical data analysis*, Mon. Not. Roy. Astron. Soc., 384, 2, 449-463 (2008).

[59] Feroz F., Hobson M.P., Bridges M. *MultiNest: an efficient and robust Bayesian inference tool for cosmology and particle physics*, Mon. Not. Roy. Astron. Soc. 398: 1601-1614 (2009).

[60] Feroz F., Hobson M.P., Cameron E., Pettitt A.N. *Importance Nested Sampling and the MultiNest Algorithm*, arXiv:1306.2144 [astro-ph.IM] (2013).

[61] Foreman-Mackey D., Hogg D. W., Lang D., Goodman J. *emcee: The MCMC Hammer*, arXiv:1202.3665 [astro-ph.IM] (2012).

[62] Akeret J., Seehars S., Amara A., Refregier A., Csillaghy A. *CosmoHammer: Cosmological parameter estimation with the MCMC Hammer*, Astronomy and Computing, Volume 2, Pages 27-39, (2013).

[63] BOSS Collaboration *The clustering of galaxies in the SDSS-III Baryon Oscillation Spectroscopic Survey: baryon acoustic oscillations in the Data Releases 10 and 11 Galaxy samples*, Mon.Not.Roy.Astron.Soc. 441 no.1, 24-62 (2014).

[64] BOSS Collaboration *Quasar-Lyman α Forest Cross-Correlation from BOSS DR11: Baryon Acoustic Oscillations*, JCAP 1405 027 (2014).

[65] Ross A. J., Samushia L., Howlett C., Percival W. J., Burden A., Manera M. *The clustering of the SDSS DR7 main Galaxy sample - I. A 4 per cent distance measure at z = 0.15*, Mon.Not.Roy.Astron.Soc. 449 no.1, 835-847 (2015).

[66] Beutler F., Blake C., Colless M., Jones D. H., Staveley-Smith L., Campbell L., Parker Q., Saunders W., Watson F. *The 6dF Galaxy Survey: baryon acoustic oscillations and the local Hubble constant*, Monthly Notices of the Royal Astronomical Society, Volume 416, Issue 4, pp. 3017-3032, (2011).

[67] SDSS Collaboration *Improved cosmological constraints from a joint analysis of the SDSS-II and SNLS supernova samples*, Astron.Astrophys. 568 A22 (2014)

[68] Bennett C. L., Larson D., Weiland J. L., Jarosik N., Hinshaw G., Odegard N., Smith K. M., Hill R. S., Gold B., Halpern M., Komatsu E., Nolta M. R., Page L., Spergel D. N., Wollack, E., Dunkley J., Kogut A., Limon M., Meyer S. S., Tucker G. S., Wright E. L. *Nine-year Wilkinson Microwave Anisotropy Probe (WMAP) Observations: Final Maps and Results*, The Astrophysical Journal Supplement, Volume 208, Issue 2, article id. 20, 54 pp. (2013)

[69] Haslam C. G. T., Salter, C. J., Stoffel, H., Wilson, W. E. *A 408 MHz all-sky continuum survey. II - The atlas of contour maps*, Astronomy and Astrophysics Supplement Series, vol. 47, p. 1, 2, 4-51, 53-142. (1982).

[70] Liddle A. *How many cosmological parameters?*, Mon.Not.Roy.Astron.Soc. 351 L49-L53 (2004).

[71] Kass R. E., Raftery A. E. *Bayes Factors*, J.Am.Statist.Assoc. 90 no.430, 773-795 (1995).

[72] Saez-Gomez D., Carvalho S. C., Lobo F. S. N., Tereno I. *Constraining $f(T, \mathtt{T})$ gravity models using type Ia supernovae*, Phys. Rev. D 94, 024034 (2016).